
Air Coupled Ultrasonic Transducers for Industrial Applications

Luftgekoppelte Ultraschallwandler für die industrielle Anwendung

Zur Erlangung des akademischen Grades Doktor-Ingenieur (Dr.-Ing.)

genehmigte Dissertation von Alexander Unger aus Cottbus

Tag der Einreichung: 26. Juni 2018, Tag der Prüfung: 19. Juni 2019

Darmstadt – D 17

1. Gutachten: Prof. Dr. mont. Mario Kupnik
2. Gutachten: Prof. Dr. rer. nat. Dr. h.c. Gerhard M. Sessler



TECHNISCHE
UNIVERSITÄT
DARMSTADT

Fachgebiet Mess- und Sensortechnik
Fachbereich 18 – Elektrotechnik und
Informationstechnik

Air Coupled Ultrasonic Transducers for Industrial Applications
Luftgekoppelte Ultraschallwandler für die industrielle Anwendung

Genehmigte Dissertation von Alexander Unger aus Cottbus

1. Gutachten: Prof. Dr. mont. Mario Kupnik
2. Gutachten: Prof. Dr. rer. nat. Dr. h.c. Gerhard M. Sessler

Tag der Einreichung: 26. Juni 2018

Tag der Prüfung: 19. Juni 2019

Darmstadt – D 17

Bitte zitieren Sie dieses Dokument als:

URN: urn:nbn:de:tuda-tuprints-89745

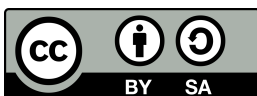
URL: <http://tuprints.ulb.tu-darmstadt.de/id/eprint/8974>

Dieses Dokument wird bereitgestellt von tuprints,

E-Publishing-Service der TU Darmstadt

<http://tuprints.ulb.tu-darmstadt.de>

tuprints@ulb.tu-darmstadt.de



Die Veröffentlichung steht unter folgender Creative Commons Lizenz:

Namensnennung – Weitergabe unter gleichen Bedingungen 4.0 International

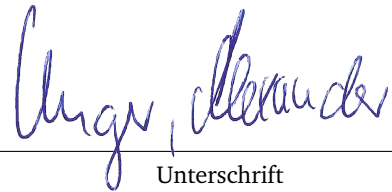
<https://creativecommons.org/licenses/by-sa/4.0/>

Decleration according to § 9 PromO

Hiermit versichere ich, die vorliegende Dissertation ohne Hilfe Dritter nur mit den angegebenen Quellen und Hilfsmitteln angefertigt zu haben. Alle Stellen, die aus Quellen entnommen wurden, sind als solche kenntlich gemacht. Diese Arbeit hat in gleicher oder ähnlicher Form noch keiner Prüfungsbehörde vorgelegen.

Darmstadt, den 26. Juni 2018

Ort, Datum

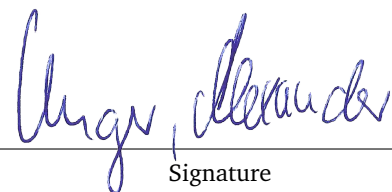


Unterschrift

Hereby I declare, that I authored the present PhD-thesis alone without third party assistance and exclusively under the use of the literature denoted. The present PhD-thesis has by now not been used in any other exam.

Darmstadt, 26th of June 2018

place and date



Signature

Department of Electrical Engineering and Information Technology
Chair of Measuerment and Sensor Technology

Abstract

Air-coupled ultrasonic transducers are widely used in many industrial, medical, or domestic applications, such as range finding, gesture sensing, or gas flow metering, to name only a few. The knowledge of the behavior and properties of the ultrasonic transducers is essential for the development and the improvement of these applications. The three most utilized work principles, e.g. piezoelectric, electrostatic, and electromagnetic, of ultrasonic transducers are explained and most common representatives of ultrasonic transducers are described. Within this thesis, several important methods of characterization in three domains (electrical, mechanical, and acoustical) of ultrasonic transducers are described, investigated and modified. The electrical impedance measurement delivers the most important characteristics of ultrasonic transducers in the electrical domain. However, the electrical impedance measurement using a common network analyzer reveals issues considering the measurement uncertainties at higher impedance values, such as the open circuit resonance frequency. In order to characterize the behavior of the ultrasonic transducers with the boundary conditions more closely to the applications, electrical impedance measurements of ultrasonic transducers at their rated excitation voltage are conducted in comparison to the common small signal network analyzer measurements. Further, the ultrasonic transducers are characterized with thermal loads, which occur, for example, in gas flow metering. A wide temperature range of almost 450 °C from -190°C using a cryo setup to $+250^{\circ}\text{C}$ using an oven are used to characterize a piezoelectric wide range transducer. In doing so, the influence of the excitation voltage and the thermal boundary conditions are investigated. A complex curve fit algorithm is implemented in MATLAB[®] and is used to fit the Butterworth-van Dyke model to the electrical impedance data gathered. The Butterworth-van Dyke model is extended by using up to seven parameters in total in order to describe additional physical effects such as contact resistance, parasitic contact capacitance, and parasitic parallel resistance. The parameters are monitored and each of them is analyzed individually to achieve a robust complex curve fit algorithm. A laser doppler vibrometer is used to characterize the surface velocity and displacement of the ultrasonic transducers in the mechanical domain. This measurement setup is extended by translational linear stages in order to obtain the surface velocity of the entire surface area of ultrasonic transducers. Through post processing of the stored A-scans at any spatial point of the area, characteristics such as the transient oscillation at each point, are visualized in a video sequence. In order to characterize ultrasonic transducers in the acoustical domain, two different volumetric sound pressure level measurement systems are used to characterize and visualize the sound pressure field using a calibrated microphone. First, a 3D linear stage which is capable of measuring the sound pressure level in a volume of 1 m^3 in front of an ultrasonic transducer in equidistant steps in any direction ($X - Y - Z$). Second, a goniometer which is built in an anechoic chamber and capable of measuring the sound pressure level in a volume of $144\pi\text{ m}^3$ in front of an ultrasonic transducer, using spherical coordinates $r-\varphi-\theta$. Further, an air-coupled 40 kHz 1D-phased array prototype with a half-wavelength pitch is built and characterized in both transmit and receive mode. It features a smart packaging layer utilizing waveguides to separate the acoustic aperture from the vibrating aperture. In doing so the acoustic characteristics are manipulated and an impressive sound pressure level of $(130 \pm 1)\text{ dB}$ at a distance of 1 m. The ultrasonic beam can be steered electronically in an angle of 110° without creating any significant grating lobes.

The approach, used in this prototype, leads to various improvements of existing applications, such as gestures sensing, gas flow meters, or imaging of entire rooms in air. Further, the mechanical amplification, using an additional horn structure on top of the vibrating aperture, of the efficient piezoelectric Murata MA40S4x ultrasonic transducers is investigated and adopted. A capacitive micromachined ultrasonic transducer is modified with such a horn structure acting as a mechanical amplifier. The horn with a diameter of 2.3 mm and a thickness of 100 μm is fabricated of aluminum using non-micromachining techniques. It is glued on top of a 55 kHz single cell device and an increased sound pressure level of (3 ± 1) dB is obtained. Within this thesis the described methods of characterizations are essential to gain needed knowledge of the behavior of ultrasonic transducers, which can lead to an improvement of many industrial, medical, or domestic applications. The described waveguide approach and mechanically amplification opens the door for various modification of ultrasonic transducers and therefore the usage in applications.

Kurzfassung

Luftgekoppelte Ultraschallwandler werden in vielen industriellen, medizinischen oder privat-häuslichen Anwendungen benutzt, wie zum Beispiel Entfernungsmessung, Gestenerkennung oder Gas Durchflussmessung um hier nur einige zu Nennen. Die Kenntnis über das Verhalten und die Eigenschaften von Ultraschallwandlern ist dabei wesentlich für die Entwicklung und die Verbesserung solcher Anwendungen. Die drei meist genutzten Wirkprinzipien, das piezoelektrische, das elektrostatische, das elektromagnetische und deren geläufigsten Vertreter von Ultraschallwandlern werden in der vorliegenden Arbeit erklärt. Wichtige Charakterisierungsmethoden von Ultraschallwandlern aus der elektrischen, der mechanischen und der akustischen Domäne werden beschrieben, untersucht und modifiziert. Die Messung der elektrischen Impedanz, häufig durchgeführt mit Netzwerkanalysatoren, liefert dabei die wichtigsten Merkmale von Ultraschallwandlern in der elektrischen Domäne. Jedoch weisen diese Messungen bei höheren Impedanzen, im Bereich der Antiresonanz, Probleme bei den Messunsicherheiten auf. Netzwerkanalysatoren nutzen dabei häufig nur eine Kleinsignalanalyse. Ultraschallwandler werden jedoch in der späteren Anwendung mit maximaler Versorgungsspannung betrieben, deshalb werden im Vergleich zur Kleinsignalanalyse Impedanzmessungen mit maximaler Versorgungsspannung untersucht. Des Weiteren werden die Ultraschallwandler unter thermischer Last untersucht, welche zum Beispiel in der Gas Durchflussmessung auftritt. Dabei wurde ein großer Temperaturbereich von fast 450°C mit Hilfe eines Cryo Aufbaus von -190°C bis 250°C in einem Ofen durchfahren und mehrere Ultraschallwandler charakterisiert. Hierbei wurden der Einfluss der Versorgungsspannung und der Einfluss der thermischen Randbedingungen untersucht. Um die Daten der Impedanzmessungen zu analysieren wurde ein Komplex-Curve-Fit Algorithmus in MATLAB[®] implementiert um das Butterworth-van Dyke Modell auf die Messdaten komplex zu fitten. Dabei wurde das Butterworth-van Dyke Modell auf bis zu sieben Elemente erweitert um zusätzliche physikalische Effekte wie den parasitären Kontaktwiderstand, die parasitäre Kontaktkapazität und den parasitären Parallelwiderstand abzubilden. Durch die Beobachtung aller sieben Parameter und die Untersuchung des Einflusses jedes einzelnen wurde ein robuster Komplex-Curve-Fit Algorithmus erreicht. Um die mechanische Domäne zu untersuchen wurden die Oberflächengeschwindigkeit und die Auslenkung der Ultraschallwandler mit einem Laser Doppler Vibrometer gemessen. Zusätzlich wurde das Einzelpunkt vibrometer mit Hilfe von Linear Achsen, für die Vermessungen von Flächen, erweitert. So können durch das Speichern der A-Scans, an jedem gemessenen Raumpunkt der Fläche, transiente Vorgänge durch erzeugen einer Videosequenz im Nachhinein dargestellt werden. Für die Charakterisierung der akustischen Domäne werden zwei volumetrische Mikrofonmesssysteme verwendet. Das Erste bietet den Vorteil einer äquidistanten kartesischen Positionierung ($X-Y-Z$) eines kalibrierten Mikrofons innerhalb eines Volumen von 1 m^3 . Das Zweite erlaubt die Vermessung von Ultraschallwandlern in einem Schallreflexionsarmen Raum über ein Volumen von rund $144\pi\text{ m}^3$ durch Ausnutzung des Goniometer Prinzips und verfahren des kalibrierten Mikrofons in Kugelkoordinaten $r - \varphi - \theta$. Ferner wird ein 40 kHz 1D-Phased Array Prototyp mit einem Pitch von halber Wellenlänge gebaut und charakterisiert. Es nutzt die Besonderheit eines Smart-Packaging-Layers welcher mit Hilfe von Wellenleiterstrukturen die akustische Apertur von der vibrierenden Apertur trennt. Dadurch werden die akustischen Merkmale manipuliert und ein Schalldruckpegel von $(130 \pm 1)\text{ dB}$ in

einem Abstand von 1 m gemessen. Dabei lässt sich die so generierte Hauptschallkeule in einem Winkel von 110° elektronisch, ohne weitere signifikante Gitterkeulen entstehen, steuern. Dieser Ansatz führt zu verschiedensten Verbesserungen von bereits existierenden Anwendungen wie Gesten Erkennung, Gas Durchflussmessungen oder Bildgebenden Verfahren in Luft für die Visualisierung ganzer Räume. Des Weiteren wurde die mechanische Verstärkung von piezoelektrischen Luftgekoppelten Ultraschallwandlern von Murata untersucht und auf einem Kapazitiven Mikromaschinell gefertigten Ultraschallwandler angewandt. Hierzu wurde eine Hornstruktur mit einem Durchmesser von 2,3 mm und einer Dicke von $100\ \mu\text{m}$ aus Aluminium gefertigt und auf einem Kapazitiven Mikromaschinell gefertigtem Ultraschallwandler 55 kHz aufgeklebt. Dabei wurde ein um (3 ± 1) dB erhöhter Schalldruckpegel gemessen. Die in der vorliegenden Arbeit beschriebenen Charakterisierungsmethoden sind wesentlich für den Kenntnisgewinn des Verhaltens von Ultraschallwandler und führen somit zur einer Verbesserung von vielen Anwendungen aus der Industrie, der Medizin, oder dem privatem Hausgebrauch. Der Wellenleiteransatz und die mechanische Verstärkung von Ultraschallwandlern weisen dabei den Weg für die verschiedensten Modifikationen und Nutzungen in den Anwendungen.

Acknowledgments

- First of all, I would like to thank my doctoral supervisor Prof. Dr. mont. Mario Kupnik, who gave me, already back in Cottbus the opportunity to join his research group. Furthermore, I would like to thank him also to offer me the chance and follow him at the Technische Universität Darmstadt. I would like to thank him for his full support, his valuable tips and the fruitful discussions during the regular research meetings.
- I would like to thank Prof. Dr. rer. nat. Dr. hc. Gerhard M. Sessler for his time and expertise and acting as reviewer for this thesis.
- Further, I would like to thank all my colleagues at both universities for their support, their knowledge exchange, our long term fruitful discussions, their tips and tricks and for all the fun we had together.
- Many thanks also to all undergraduates and graduates students that I have supervised.
- Especially I would like to thank my entire family for their support, their patience, their mutual understanding and their encouragement in both good and bad times.
- Special thanks to Maria and Alex. Everything started with you.
- Finally I would like to thank all my friends and all the people who believed in me.

List of Publications

2017

A. Jäger, A. Unger, H. Wang, Y. Arnaudov, L. Kang, R. Su, D. Lines, S. N. Ramadas, S. Dixon, and M. Kupnik. “Ultrasonic phased array for sound drift compensation in gas flow metering”. In: *2017 IEEE International Ultrasonics Symposium (IUS)*. Sept. 2017, pp. 1–4. DOI: [10.1109/ULTSYM.2017.8092174](https://doi.org/10.1109/ULTSYM.2017.8092174)

A. Jäger, D. Großkurth, M. Rutsch, A. Unger, R. Golinske, H. Wang, S. Dixon, K. Hofmann, and M. Kupnik. “Air-coupled 40-KHZ ultrasonic 2D-phased array based on a 3D-printed waveguide structure”. In: *2017 IEEE International Ultrasonics Symposium (IUS)*. Sept. 2017, pp. 1–4. DOI: [10.1109/ULTSYM.2017.8091892](https://doi.org/10.1109/ULTSYM.2017.8091892)

2016

F. Schiewer, Han Wang, A. Unger, N. Stefanova, and M. Kupnik. “Single-transducer acoustic levitator with equidistant vertical positioning capability”. In: *2016 IEEE International Ultrasonics Symposium (IUS)*. Sept. 2016, pp. 1–4. DOI: [10.1109/ULTSYM.2016.7728813](https://doi.org/10.1109/ULTSYM.2016.7728813)

S. E. Burrows, S. N. Ramadas, T. J. R. Eriksson, L. Kang, S. M. Dixon, A. Unger, and M. Kupnik. “High temperature flexural ultrasonic transducer for non-contact measurement applications”. In: *2016 Joint IEEE International Symposium on the Applications of Ferroelectrics, European Conference on Application of Polar Dielectrics, and Piezoelectric Force Microscopy Workshop (ISAF/ECAPD/PFM)*. Aug. 2016, pp. 1–3. DOI: [10.1109/ISAF.2016.7578077](https://doi.org/10.1109/ISAF.2016.7578077)

2015

A. Unger, E. Konetzke, M. Rutsch, M. Hoffmann, S. N. Ramadas, S. Dixon, and M. Kupnik. “Versatile air-coupled phased array transducer for sensor applications”. In: *2015 IEEE SENSORS*. Nov. 2015, pp. 1–4. DOI: [10.1109/ICSENS.2015.7370187](https://doi.org/10.1109/ICSENS.2015.7370187)

C. Hatzfeld, C. Schröder, A. Unger, O. Morar, T. Klemm, M. Kupnik, and R. Werthschützky. “Flow sensor for field measurement of viscous liquid usage for consumer studies”. In: *2015 IEEE SENSORS*. Nov. 2015, pp. 1–4. DOI: [10.1109/ICSENS.2015.7370343](https://doi.org/10.1109/ICSENS.2015.7370343)

E. Konetzke, M. Rutsch, M. Hoffmann, A. Unger, R. Golinske, D. Killat, S. N. Ramadas, S. Dixon, and M. Kupnik. “Phased array transducer for emitting 40-kHz air-coupled ultrasound without grating lobes”. In: *2015 IEEE International Ultrasonics Symposium (IUS)*. Oct. 2015, pp. 1–4. DOI: [10.1109/ULTSYM.2015.0019](https://doi.org/10.1109/ULTSYM.2015.0019)

M. Rutsch, E. Konetzke, A. Unger, M. Hoffmann, S. N. Ramadas, S. Dixon, and M. Kupnik. “Extending the receive performance of phased ultrasonic transducer arrays in air down to 40 kHz and below”. In: *2015 IEEE International Ultrasonics Symposium (IUS)*. Oct. 2015, pp. 1–4. DOI: 10.1109/ULTSYM.2015.0095

R. Golinske, M. Hoffmann, E. Konetzke, A. Unger, M. Rutsch, and M. Kupnik. “Diffraction loss calculation based on boundary element method for an air-coupled phased array”. In: *2015 IEEE International Ultrasonics Symposium (IUS)*. Oct. 2015, pp. 1–4. DOI: 10.1109/ULTSYM.2015.0375

T. J. R. Eriksson, S. N. Ramadas, A. Unger, M. Hoffman, M. Kupnik, and S. M. Dixon. “Flexural transducer arrays for industrial non-contact applications”. In: *2015 IEEE International Ultrasonics Symposium (IUS)*. Oct. 2015, pp. 1–4. DOI: 10.1109/ULTSYM.2015.0047

M. Hoffmann, A. Unger, A. Jäger, and M. Kupnik. “Effect of transducer port cavities in invasive ultrasonic transit-time gas flowmeters”. In: *2015 IEEE International Ultrasonics Symposium (IUS)*. Oct. 2015, pp. 1–4. DOI: 10.1109/ULTSYM.2015.0272

A. Guseva, M. Hoffmann, A. Unger, S. Zulk, M. B. El Amien, E. Sarradj, and M. Kupnik. “Ultrasonic transducer characterization in air based on an indirect acoustic radiation pressure measurement”. In: *2015 IEEE International Ultrasonics Symposium (IUS)*. Oct. 2015, pp. 1–4. DOI: 10.1109/ULTSYM.2015.0333

Min-Chieh Ho, Maik Hoffmann, Alexander Unger, Park Kwan Kyu, Mario Kupnik, and Butrus T. Khuri-Yakup. “CMUTs in permanent contact operation for high output pressure”. In: *ASME 2015, InterPACK-ICNMM*. July 2015. URL: <http://tubiblio.ulb.tu-darmstadt.de/77484/>

2013

M. Hoffmann, A. Unger, M. C. Ho, Kwan Kyu Park, B. T. Khuri-Yakup, and M. Kupnik. “Volumetric characterization of ultrasonic transducers for gas flow metering”. In: *2013 IEEE International Ultrasonics Symposium (IUS)*. July 2013, pp. 1315–1318. DOI: 10.1109/ULTSYM.2013.0336

A. Unger, M. Hoffmann, M. C. Ho, K. K. Park, B. T. Khuri-Yakup, and M. Kupnik. “Finite element analysis of mechanically amplified CMUTs”. In: *2013 IEEE International Ultrasonics Symposium (IUS)*. July 2013, pp. 287–290. DOI: 10.1109/ULTSYM.2013.0074

List of Oral Presentations

2016

"Single-transducer acoustic levitator with equidistant vertical positioning capability", at 2016 IEEE International Ultrasonics Symposium (IUS) in Tours, France.

"High temperature flexural ultrasonic transducer for non-contact measurement applications", at 2016 Joint IEEE International Symposium on the Applications of Ferroelectrics, European Conference on Application of Polar Dielectrics, and Piezoelectric Force Microscopy Workshop (ISAF/ECAPD/PFM) in Darmstadt, Germany.

2015

"Versatile air-coupled phased array transducer for sensor applications", at 2015 IEEE SENSORS in Busan, South Korea.

"Flow sensor for field measurement of viscous liquid usage for consumer studies", at 2015 IEEE SENSORS in Busan, South Korea.

"Extending the receive performance of phased ultrasonic transducer arrays in air down to 40 kHz and below", at 2015 IEEE International Ultrasonics Symposium (IUS) in Taipei, Taiwan.

2013

"Finite element analysis of mechanically amplified CMUTs", at 2013 IEEE International Ultrasonics Symposium (IUS) in Prague, Czech Republic.

Contents

1	Introduction	1
1.1	Motivation	1
1.2	Industrial Applications	2
1.3	Structure of this Thesis	3
1.4	Original Work	4
2	Basics of Air-Coupled Ultrasonic Transducers	6
2.1	Air Coupled Ultrasonic Transducers	6
2.2	Active Work Principle of Ultrasonic Transducers	6
2.2.1	Ultrasonic Transducers Based on the Piezoelectric Principle	7
2.2.2	Ultrasonic Transducers Based on the Electrostatic Principle	11
2.2.3	Ultrasonic Transducers Based on the Electromagnetic Principle	15
2.3	Equivalent Circuit Model and its Parameter	15
2.4	Separation of the Acoustic Aperture	22
3	Methods of Characterization	25
3.1	Electrical Impedance Measurements	25
3.1.1	Measurement Setup Network Analyzer	27
3.1.1.1	Measurement Uncertainty	29
3.1.1.2	Bias-T with Protection Circuit	33
3.1.2	Impedance Measurement Setup for Higher Excitation Voltage	38
3.1.3	Ambient Temperature Impedance Measurements	42
3.1.4	High Temperature Impedance Setup	43
3.1.5	Cryo Temperature Impedance Setup	43
3.2	Surface Velocity and Displacement	45
3.2.1	Measurement Setup	45
3.2.2	Surface Velocity and Displacement Measurement	48
3.2.3	Surface Pressure	50
3.3	Sound Pressure Level	51
3.3.1	Measurement Setup Based on a Goniometer	51
3.3.2	Measurement Setup Based on 3D Linear Stages	54
3.3.3	Sound Pressure Field	55
3.4	Schlieren Photography Setup	56
3.4.1	Schlieren Setup	56
3.4.2	Sound Pressure Field	57
4	Automatic Parameter Extraction	59
4.1	Extended Butterworth-van Dyke Model	59

4.2	Extended 7-elements Butterworth-van Dyke Model and the Influence of its Parameters . . .	61
4.3	Complex Curve Fit Algorithms	72
4.3.1	Finding Start Parameters	73
4.3.2	Monitoring of the Fit Parameters	74
5	Waveguides an Approach of Separation of the Acoustic Aperture	81
5.1	Fabrication of the Phased Array utilizing Waveguides	82
5.2	First Characterization Measurements	84
5.2.1	Transmit Mode	84
5.2.2	Receive mode	84
5.3	Results and Conclusions	85
6	Mechanical Amplification of CMUT	88
6.1	The Finite Element Model	89
6.2	Horn Fabrication and Simulations Results	90
6.3	First Measurements for Validation	91
6.4	Conclusion of a Mechanically Amplified CMUT	93
	Conclusion and Future Work	94
	List of used symbols	96
	Acronyms and abbreviation	98
	Bibliography	100
	List of Figures	109
	List of Tables	111
	Curriculum vitae	112

1 Introduction

Ultrasonic transducers, ultrasonic actors or ultrasonic sensors are important and mostly inexpensive devices, which are being used for many applications. They are typically designed to their designated field and environment. Here ultrasonic transducers generate ultrasound and therewith ultrasound waves do propagate into the media. Thereby ultrasonic transducers are able to transmit and receive ultrasound due to reciprocity.

1.1 Motivation

Ultrasonic (US) transducers are widely used in many industrial, automotive, medical and domestic applications. They are essential for non-destructive evaluation, medical imaging, range finding, container less processing, acoustic tweezing, haptic holograms, gesture sensing, tactile displays, parametric loudspeakers, directed ultrasonic communications, anemometry, temperature measurement, ultrasonic cleaning, ultrasonic welding or flow metering to name a few. According to the field of using ultrasound and ultrasonic transducers their work principle can be distinguished in solid state or fluid physics. Whereby fluids are again separated into liquids and gases. So ultrasonic transducer are being distinguished again between immersion or emersion devices. Therefore their frequency varies depending on states of matter of the media in which ultrasound is propagating (Table 1.1). Due to different properties of the me-

Table 1.1: Overview of most typical frequencies of ultrasound used in different media and its specific speed of sound [16].

Media	Frequency range for US transducer	Speed of sound range
Solids	500 kHz – 1 GHz	$60 \frac{\text{m}}{\text{s}} - 18000 \frac{\text{m}}{\text{s}}$
Liquids	500 kHz – 50 MHz	$1168 \frac{\text{m}}{\text{s}} - 1540 \frac{\text{m}}{\text{s}}$
Gases	20 kHz – 500 kHz	$130 \frac{\text{m}}{\text{s}} - 1280 \frac{\text{m}}{\text{s}}$

dia the principle of generating ultrasound efficiently has also to be different. US transducers can be classified in piezoelectric (PUTs, PMUTs), electrostatic (CUTs, CMUTs), and magnetostrictive (EMATs) transducers (Chapter 2.1). Ultrasonic transducers are often particularly designed for a desired frequency range, by using the physical active principle and housing for their own application. However, the focus of this thesis is mostly on air-coupled Capacitive Micromachined Ultrasonic Transducers (CMUTs) and air-coupled Piezoelectric Ultrasonic Transducers which are using the radial (mono-morph) [17] and thickness mode (bolt-clamped Langevin) concept [18].

So to use these ultrasonic transducers in industrial application in an optimal way the knowledge about their behavior and characteristic is essential. Besides geometric parameters such as aperture size or focal length important characteristics are the electrical impedance, the surface velocity, the sound pressure field, or the sound pressure level. Therefore proper methods of characterization are essential and are introduced, described, and analyzed in this thesis.

1.2 Industrial Applications

Of the many industrial applications here the ultrasonic flow meters and the ultrasonic imaging are described in more detail. A common and important industrial application where ultrasonic transducer are being used is flow metering. Ultrasonic flow meters (UFMs) are available for liquids and for gases. The difference is the driving frequency of the ultrasonic transducer and its active work principle. Mostly piezoelectric-driven ultrasonic transducer are used (Chapter 2.2.1). They are robust and can be used in these domains of fluids. UFMs are using different types of measurement principles, e.g. ultrasonic transit time, ultrasonic laser doppler, ultrasonic correlation, and ultrasonic vortex shedding UFMs [19]. For example, a common transit time UFM consists of at least one acoustic path which is consists of two ultrasonic transducers. One transducer acts as a transmitter emitting ultrasound and the other one acts as a receiver. The time of flight (TOF) of the ultrasound signal is measured downstream and upstream. Now, depending on the flow velocity of the media inside the flow meter the TOF upstream will be different than the TOF downstream. Hence, the velocity of the media can be calculated, knowing or assuming the flow profile. In order to increase the accuracy, multi path transit time UFM measure the TOFs via several independent paths, so the flow profile can be gathered much more precisely.

The main goal to determine the robust and strong ultrasonic transducers is knowing as much as possible of those ultrasonic transducer such as sound pressure level (SPL), beam characteristics, or temperature dependencies, high and low temperatures, can be essential. Therefore characterizing such ultrasonic transducers with several methods can lead to an advantages in these applications in design, development and fabrication of UFMs. Of course this is valid for the other types of UFMs as well. In this work therefore most important characterization methods such as electrical impedance, sound pressure level, surface velocity measurements are described and used for characterizations and investigations.

Next, another important industrial application is ultrasonic imaging. Looking into medical imaging, ultrasonic examinations are widely used and already standard and available since many years. Here the imaging takes places with high frequencies usually in range of several mega hertz, since those examinations are conducted in liquids and tissue inside of the human body. In order to gather an image an array consisting of many hundreds small ultrasonic transducers is used and controlled by electronics to steer and focus the ultrasonic beam in two dimensions. In doing so, an area of interest can be scanned and therewith an image is constructed based on the pulse echo TOFs.

However, imaging in air, based on electronic steering, is not available yet and needs to be further developed. The main advantages of an ultrasonic imaging would be that it is non intrusive and it would be impervious against smoky, dusty, or foggy environments. So when using it for supervision of elder people who are living alone if they are for example plunged, their privacy and dignity is still protected. In case of an emergency the emergency service can be called. Also scanning a smoky room, fire fighters would get an image and could detected people as well.

But the main issues in air are the missing ultrasonic transducers below 200 kHz, which fulfill the needs of a good quality imaging systems. Those are broadband transducers, for good spatial resolution, with

enough sound pressure level and sensitivity for a high signal-to-noise-ratio (SNR) and an aperture size which fits the half-wavelength criteria. This criteria is required to build an array of ultrasonic transducers with no significant grating lobes [16]. Grating lobes reduce the field of view, by inducing ambiguities. This is no problem when arrays for imaging in liquids are used, due to the order of magnitudes higher frequency and the higher speed of sound in liquids. Therefore the array elements easily can be made smaller than the half-wavelength.

In this thesis a concept of separating the acoustic aperture from the actual vibrating aperture is introduced and investigated (Chapter 5). This separation is achieved by using waveguides, such as acoustic tubes or channels. Using such waveguide structure opens the door for many industrial applications such as imaging of entire rooms with a half-wavelength array by reducing the pitch of the ultrasonic transducers. Furthermore, thinking of harsh environment industrial applications with high or low temperatures a proper waveguide could be used to protect the ultrasonic transducer by building a negative temperature gradient with cooling or a positive one with heating. The ultrasonic transducer works always in its specified point of operation. Such harsh environments such as found in non-destructive testing (NDT) or non-destructive evaluation (NDE) or even in non-contact non-destructive testing (NCNDT) or non-contact non-destructive evaluation (NCNDE) when conducted in-situ on molten or hot materials.

1.3 Structure of this Thesis

This thesis is structured as follows. After a short motivation with several examples of the usage of ultrasonic transducers for industrial applications the author declares his original work, in which mainly five contributions are described.

In chapter 2 the basics of air-coupled ultrasonic transducers are described. The three main work principles of generating ultrasound are introduced and described in more detail. The important and overall valid equivalent circuit model "the Butterworth-van Dyke model" is derived and the main parameters are explained. An interesting interdisciplinary approach of separating the vibrating structure from the acoustic aperture is discussed.

Chapter 3 describes the four most important methods of characterization of ultrasonic transducers. First, the electrical impedance measurements and with its accuracy at small signals and ambient temperatures is discussed. Then this method is compared with a higher excitation voltage, which is used to characterize the electrical impedance of ultrasonic transducers in their point of operation. Following by the electrical impedance measurements of the wide temperature range of -190°C up to 250°C . Second, the characterization of the surface velocity of ultrasonic transducers, using a laser vibrometer, which was in addition modified to scan the surface of ultrasonic transducers. Third, the calibrated measurement of the sound pressure level as one of the most important quantities and the visualization of the sound pressure field by utilizing two different volumetric measurement setups. Finally, the quantitative visualization of the sound pressure field using a Schlieren photography setup.

In Chapter 4 the automatic parameter extraction using a complex curve fit algorithm is introduced. Furthermore the Butterworth-van Dyke model is extended to consider more physical effects and a method

for finding the model and good starting values by monitoring the parameters is described. Therefore a program was written in LabVIEW™ to manipulate parameters individually.

Then in chapter 5 the already discussed separation of the vibrating structure from the acoustic is implemented, by building an air-coupled phased array with a half-wavelength pitch by utilizing waveguides. The phased array is then characterized in transmit and receive mode.

Chapter 6 introduces a mechanically amplified capacitive micromachined ultrasonic transducer by modifying a device without micromachining techniques. This idea was born by characterizing an efficient piezoelectric ultrasonic transducer from Murata. A finite element study was conducted and a promising dimension of the mechanical amplifier was built and glued on a 55 kHz capacitive micromachined ultrasonic transducer, which was then characterized measuring the sound pressure level.

Finally a conclusion of this thesis is given and future work is discussed.

1.4 Original Work

In the author's opinion the original part of the work are the following:

- 1) Electrical impedance characterization with excitation voltages up to $70V_{pp}$.

A common characterization of ultrasonic transducers is the electrical impedance measurement using a network or an impedance analyzer. These analyzers often feature methods where only small signal levels, e.g. $1V_{RMS}$ are used to obtain the electrical impedance of a device under test (DUT). However, in many industrial applications such as container less processing, range finding, or gas flow metering, only to name a few, the ultrasonic transducers are driven by their maximum ratings of voltage and current and therewith at their maximum power level. Higher signals, e.g. maximum excitation voltage, have to be investigated and electrical impedance measurements need to be conducted at those excitations voltage levels. Since, depending on the active work principles (Chapter 2), ultrasonic transducers can have effects such as frequency shifts, mechanical or electrical bifurcation [20, 21, 22], which are non-linear behaviors in regimes of higher driving settings, e.g. high excitation voltage.

- 2) Electrical impedance characterization over a wide temperature range of $440^{\circ}C$.

In most cases, ultrasonic transducers are designed for a specific operation range, e.g. temperature, ambient pressure, or other environmental conditions. However, piezoelectric ultrasonic transducers can, for example have a Curie temperature. The electrical impedance measurement needs to be conducted over a wide temperature range to investigate the effects due to the thermal load conditions. The very same ultrasonic transducers were characterized from $-190^{\circ}C$ up to $250^{\circ}C$ and their impedance data were analyzed.

- 3) Complex curve fit with automatic parameter extraction.

The knowledge of several important parameters of a DUT, its characteristics and therewith a predictability of its behavior are important for an application development and for the fabrication of the DUT itself. In order to obtain these parameters a proper equivalent circuit – the Butterworth-van Dyke model – is fitted to electrical impedance measurement data. A complex curve fit algorithm has to be used, since the electrical impedance is a complex characteristic quantity, which consists of magnitude and phase. A complex curve fit algorithm is implemented in MATLAB[®] and Mathematica[®], which is used to fit models consisting of up to seven parameters.

4) Separation of acoustic aperture from vibrating aperture.

The separation of the acoustic aperture from the vibrating aperture can be found in nature, i.e. the lips and the vocal cords in humans [23]. This separation allows the manipulations of the generated sound. The author shows an approach of separating the acoustic aperture from the vibrating aperture [24, 25] using waveguides to build an air-coupled 1D-phased array with a pitch of half-wavelength at 40 kHz for both transmit and receive, whereby reciprocity is demonstrated for the first time. In doing so it is capable of transmitting and receiving ultrasound without any significant grating lobes with an opening angle electronically steered by 110° in total [5].

5) Mechanical amplification of a capacitive micromachined ultrasonic transducer.

Mechanical amplification using a horn is state-of-the-art for many piezoelectric ultrasonic transducers [3, 26, 27]. The author shows the possibility of a mechanical amplification of a 55 kHz air-coupled capacitive micromachined ultrasonic (CMUT) transducer, to improve both its sound pressure level in transmit mode and its sensitivity in receive mode [15]. A horn, fabricated by the author using non-micromachining techniques, was attached to a CMUT, which increased the center-to-average displacement ratio in both transmit and receive mode [15], thus the modified CMUT was characterized.

2 Basics of Air-Coupled Ultrasonic Transducers

This chapter gives an overview of most common air-coupled ultrasonic transducers. Hence, piezoelectric, electrostatic and electromagnetic ultrasonic transducers are described and thus their active work principle is explained. The Butterworth-van Dyke model is derived from the mechanical domain and important parameters of ultrasonic transducers are introduced. Further an interdisciplinary approach of the separation of the actual vibrating structure and the acoustic aperture is described.

2.1 Air Coupled Ultrasonic Transducers

Beforehand air-coupled ultrasonic transducers are the main objective in this thesis. When speaking of air-coupled ultrasonic transducers emersed transducers working in gases are meant. Conventionally ultrasonic transducers convert – such as any electro-acoustic transducer – electrical energy into acoustic energy and vice versa, i.e. these can act as transmitter or receiver, due to reciprocity. Similar as a loudspeaker and a microphone combined in one device. The energy conversion is not done directly from electrical to acoustic energy. The electrical energy is primarily converted to mechanical energy and the mechanical energy is then subsequently converted to acoustic energy. Whereby the acoustic energy is a special subdomain of mechanical energy. The same principle applies the other way around, when first acoustic energy is converted to mechanical energy and then mechanical energy is converted to electrical energy.

Thereby the acoustic to mechanical or mechanical to acoustic conversion occurs always through a mechanical oscillation system, which is usually a mass-spring-damper system. This conversion is responsible for the directivity pattern of the ultrasonic transducer and also its efficiency [16]. Whereas the electrical to mechanical or the mechanical to electrical conversion principle is depending on the type of ultrasonic transducer. It can be reversible or non-reversible [16]. The three most common conversion principles are piezoelectric, electrostatic and magnetostrictive and are described as follows.

2.2 Active Work Principle of Ultrasonic Transducers

In general, the active work principle of ultrasonic transducers, meaning the electrical to mechanical and mechanical to electrical conversion can be distinguished into three groups. Namely ultrasonic transducers which are based on the piezoelectric, based on the electrostatic and based on the electromagnetic (Figure 2.1). Within these groups the ultrasonic transducers are further classified and are represented by a selection of transducer types.

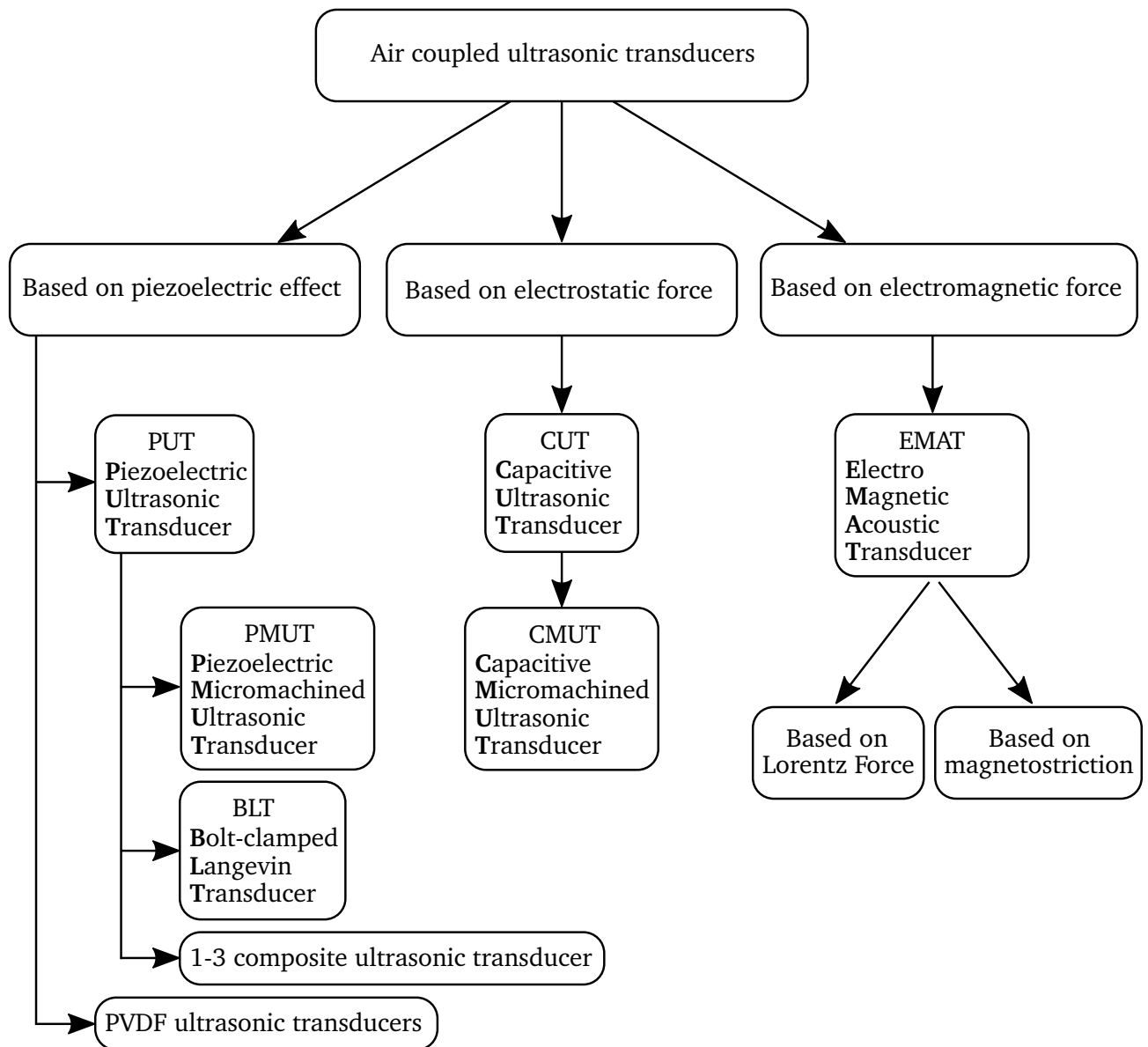


Figure 2.1: Overview of most common air coupled ultrasonic transducers and classification according their work principles.

The focus of this work is on reversible conversion principles and air-coupled ultrasonic transducers only. PUTs, BLT and CMUTs are used in this thesis. However, these basics are more or less the same for immersion transducer, e.g. in water or liquids in general.

2.2.1 Ultrasonic Transducers Based on the Piezoelectric Principle

Piezoelectric materials are widely used in many applications. Piezoelectric materials feature an electric polarization when mechanically stressed or deformed. It is called piezoelectric effect and is being used to receive ultrasound. The reciprocal piezoelectric effect works the other way around, piezoelectric materials deform themselves when an electrical voltage is applied, which is being used to transmit ultrasound.

Piezoelectric materials in particular piezoelectric ceramics have resonant frequencies depending on their specific elastic vibration [17]. This vibration is a function of the shape of the piezoelectric ceramic material. Furthermore piezoelectric ceramics can have various vibration modes, such as radial, longitudinal, transversal, thickness and shear mode to name a few [17]. These modes depend on the shape of the piezoelectric ceramic, orientation of polarization during the fabrication process, and the direction of the electric field. At this point only a few important piezoelectric ultrasonic transducers will be discussed.

First, unimorph or monomorph piezoelectric ultrasonic transducers. They have one piezoelectric active layer which is attached to a non-active layer, e.g. metal. The piezoelectric layer uses the radial mode. It is expanding and contracting when an excitation voltage is applied to its electrodes. The term bimorph is often used instead, which is miss leading, because it refers to the similar bi-metal structure due to its bending characteristic. The ultrasonic transducer MA40S4x (Murata Manufacturing Co. Ltd.,

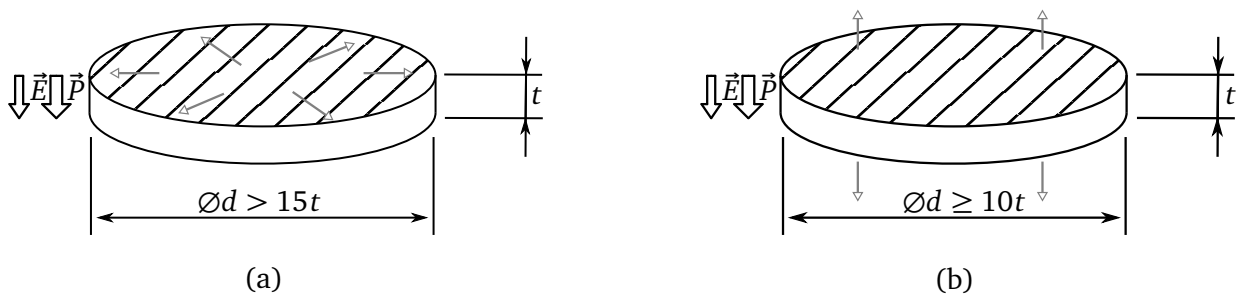


Figure 2.2: Comparison of a radial mode of a piezoelectric material (a) and thickness mode of a piezoelectric material (b), the hatched area indicates the electrodes, \vec{E} is Electric Field, and \vec{P} the polarization. The vibration modes of a piezoelectric material depend on the shape, dimension, orientation of polarization, and direction of the applied electric field [17].

Higashikotari, Kyōto, Japan) [Figure 2.3 (a)] is an efficient ultrasonic transducer of this monomorph type. Here the metal plate is made of brass where the Piezo layer PZT-7B [17] is glued at the bottom side. This structure is fixed at the almost outer diameter with silicone to the base [Figure 2.3 (b)]. Therefore it can bend up and down freely at its center point.

Additionally it has a horn or funnel-shaped structure, an equalizer [26], out of aluminum attached to the top side at the center of the brass plate [Figure 2.3 (b)]. This acts as a mechanical amplifier due to its larger average-to-center displacement ratio [15] (Chapter 6). The monomorph structure is bending in transmit mode the most in the center, but this area is relatively small compared to the entire brass plate area. Using this horn concept the displacement of the small area is enlarged to a bigger area, namely the entire diameter of the aluminum horn (Figure 2.4). In receiving mode the horn structure amplifies and concentrates the incoming sound wave by focusing its energy, respectively force to the center of the monomorph structure (Figure 2.4), where its sensitivity is largest, due to its constructional constraints.

The acoustic aperture and the vibrating aperture is still the same. But using the ultrasonic transducer with its housing, as it is intended, the opening grid of the housing becomes the new acoustic aperture. So the MA40S4x are well designed transducers, looking at the full assembly. However it is a narrow band [16] ultrasonic transducer operating at 40kHz [28]. Excited with $10V_{\text{RMS}}$ Sine wave signal, it features (120 ± 3) dB Sound Pressure Level (SPL) at a distance of 30 cm [29]. The MA40S4x can be used

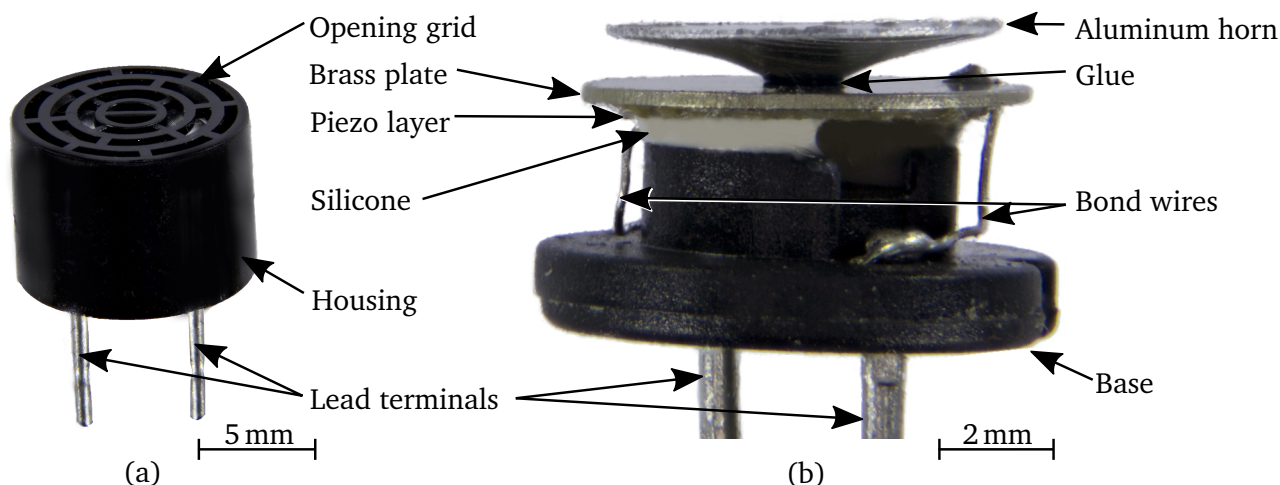


Figure 2.3: Murata MA40S4S 40 kHz 10 mm ultrasonic transducer (a), inside view of a Murata MA40S4S where the housing has been removed (b), slightly enlarged.

as a transmitter as well as a receiver. Although Murata offers a dedicated transmitter MA40S4S and a better matched dedicated receiver MA40S4R (see Chapter 2.3 for more detail). Monomorph or bending plate ultrasonic transducers are overall efficient in transmitting and receiving ultrasound in air.

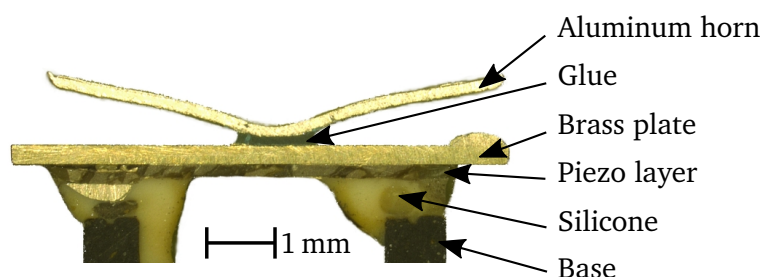


Figure 2.4: Murata MA40S4S 10 mm ultrasonic transducer without housing cut in half, using Technovit[®] 5071 (Kulzer GmbH, Wehrheim, Germany) a fast curing two component embedding resin [30], to visualize the monomorph structure with Keyence VHX-600 Microscope (Keyence Osaka, Japan). Whereby the Technovit[®] 5071 was removed using a photo editing software.

Second, composite ultrasonic transducers, consisting of a mixed combination of different components, these can be piezo ceramics mixed with glass beads, air bubbles, polymer or epoxy resin. Common piezo-composites are 1-3 composite ultrasonic transducers (Figure 2.5). Here the piezo ceramic is structured in varies shapes and sizes and it is isolated mostly with epoxy resin. The 1-3 composite ultrasonic transducers are named by their connectivity [31]. Where the first number stands for the piezo-active component and the second number for the less or even non piezo-active component. Imagine a typical coordinate system (xyz), in which the classification ranges from 0, 1, 2 to 3. Then 1 corresponds to only one direction independent of (xyz) and 2 corresponds to two independent directions of (xyz), a combination of ($x;y$), ($x;z$) or ($y;z$). With 0 standing for an isolated component with no connectivity and 3 as a fully connected component in every direction of (xyz). Therewith the connectivity directions

of both materials are described. So in 1-3 composites, the piezo-active component (piezo ceramic) is connected in one direction either in x, y or z (1). Then the non-piezo-active component (epoxy resin), which is connected in three directions (3).

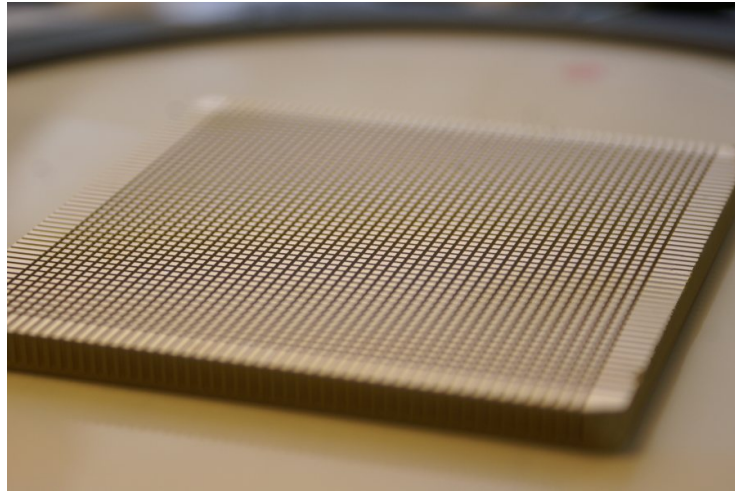


Figure 2.5: 1-3 piezo composite ultrasonic transducer from Precision Acoustics (Dorchester, UK) [32].

Such as $\frac{\lambda}{4}$ piezo ultrasonic transducers, composite ultrasonic transducers for air coupling often do need an impedance matching layer in front of them. Unlike 1-3 composite ultrasonic transducers for immersion (e.g. water), where such a layer is often not needed due to the better acoustic impedance matching of water 1.5 MRayl to 6.5 MRayl of the composite material, which is equivalent to 1.5 MPasm^{-1} to 6.5 MPasm^{-1} in SI-units. This layer is usually used to improve the coupling efficiency into air, due to its better acoustic impedance match [16]. The impedance mismatch between piezo material and air can be reduced stepwise using several matching layers of $\frac{\lambda}{4}$ or even $\frac{\lambda}{8}$ [33, 34].

Most piezo composite ultrasonic transducers have a so called backing. The backing is an absorbing material, which reduces the backwards dissipated ultrasonic sound wave. It can be glued or infused to the back side of the piezo-active composite material. Such backing is often used to increase the bandwidth due to its damping behavior. In doing so the transducers efficiency is reduced, there is always a trade off [16]. Therefore composite ultrasonic transducers are often more broadband but less efficient than monomorph or bending plate ultrasonic transducers, which results in better spatial resolution in imaging applications.

Third, Bolt Clamped Langevin (BLT) half wavelength ultrasonic transducers. Those ultrasonic transducers consists of two or more piezoelectric disks, which are clamped mechanically in between the front-, and back-end using a bolt [Figure 2.6 (a)]. The piezoelectric disks are electrically connected via interlacing polarity electrodes [Figure 2.6 (b)] and are operating in thickness mode. Stacking these piezo disks in larger number fitted to the resonance the more performance is available. They are clamped as well using a bolt or screw, which is forcing the back-, and front-end together. This is also called mechanically prestressed. Unlike the other two described piezoelectric ultrasonic transducers the prestress is here necessary to let the BLT work properly. First, the mechanically prestress is used to fine tune its resonance frequency. Second, without enough prestress the brittle piezo disks would burst due to the high surface velocities (Chapter 3.2). The dimensions of the back-end and of the front-end as well have

to match the wavelength. Depending of their material and therefore depending on their speed of sound of the back-end and of the front-end the length of the entire ultrasonic transducer has to match $\frac{n}{2}\lambda$. Hence, the surface velocity at the front face of the ultrasonic transducer has its maximum. In doing so the BLT ultrasonic transducers are acting such as a piston. Therefor they have to be mounted in a node of oscillation to allow a free movement for maximum performance when dissipating ultrasound into air or such as the 40 kHz ultrasonic transducer SMBLTD45F40H (STEMINC Steiner & Martins, INC, Doral, FL, USA) is therefore mounted with its front face directly onto a surface of interests (e.g. ultrasonic cleaning tanks, ultrasonic plastic welding, fluid mixer transducer, solid separation transducer, or stop organism growth on boat hull [18]).

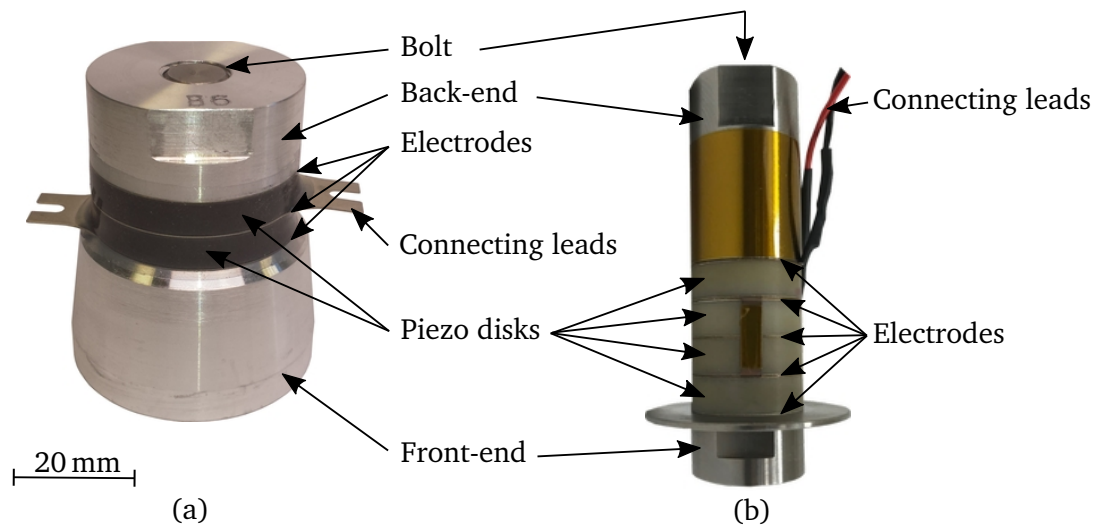


Figure 2.6: Bolt-Clamped Langevin 40 kHz ultrasonic transducer SMBLTD45F40H (STEMINC Steiner & Martins, INC, Doral, FL, USA) (a) and another type of Langevin ultrasonic transducer which has four piezo ceramic disks being custom made and investigated for a third party project (b) Copyright Steffen Elgner [35].

2.2.2 Ultrasonic Transducers Based on the Electrostatic Principle

Another group of common ultrasonic transducers are the ultrasonic transducers based on the electrostatic principle. They consist of two electrodes facing each other such as a capacitor in principle. Thereby one electrode is fixed and cannot move or bend. The counter electrode however is thin and can be deformed. This can either be a thin foil, which acts as a membrane or a thin plate, which acts as a bending plate. Those devices are often referred as capacitive ultrasonic transducers (CUTs) and the latter one capacitive micromachined ultrasonic transducers (CMUTs). In between those electrodes is either air or vacuum for electrical isolation. Both transducer types have a deformable foil or plate structure at the front. So vibration of this structure can generate the ultrasonic wave. In contrast to ultrasonic transducers based on the piezoelectric principle such as monomorph or 1-3 composite ultrasonic transducers a capacitive transducer always need to be prestressed. CUTs and CMUTs are often prestressed mechanically and electrically using a high DC-Bias voltage.

A common capacitive ultrasonic transducer (CUT) is the Series 600 [Figure 2.7 (b)] ultrasonic transducer (SensComp, Inc., Livonia, MI, USA), which was originally design by Polaroid™ for their auto focus ranging system [36]. Its back electrode is made of aluminum. This electrode features concentric circular shaped V-groves machined in [Figure 2.7 (a)]. These groves provide small cavities in combination with the front electrode, a foil [Figure 2.7 (a)]. These cavities filled with air allowing the foil to vibrate slightly in and out. So ultrasound can be generated. The foil is gold or metal plated on one side so the opposite side is acting as an electrical isolation. The foil is clamped to the front face or welded onto a ring [Figure 2.7 (a)]. Thereby the foil is mechanically prestressed by the spring pushing from the backside of the transducer at the back electrode and stretching therewith the foil. Furthermore the back electrode acts as the high voltage or hot electrode and the front electrode, the foil, as the ground or cold electrode. Since the foil is surrounded by air a CUT is usually damped and therefore it is less efficient regarding its sound pressure level but it is more broadband. That is why these CUTs have a specified center frequency of 50 kHz rather than a resonance frequency [37]. A perforated front face housing made of stainless steel covers the CUT and protects the thin foil [Figure 2.7 (b)].

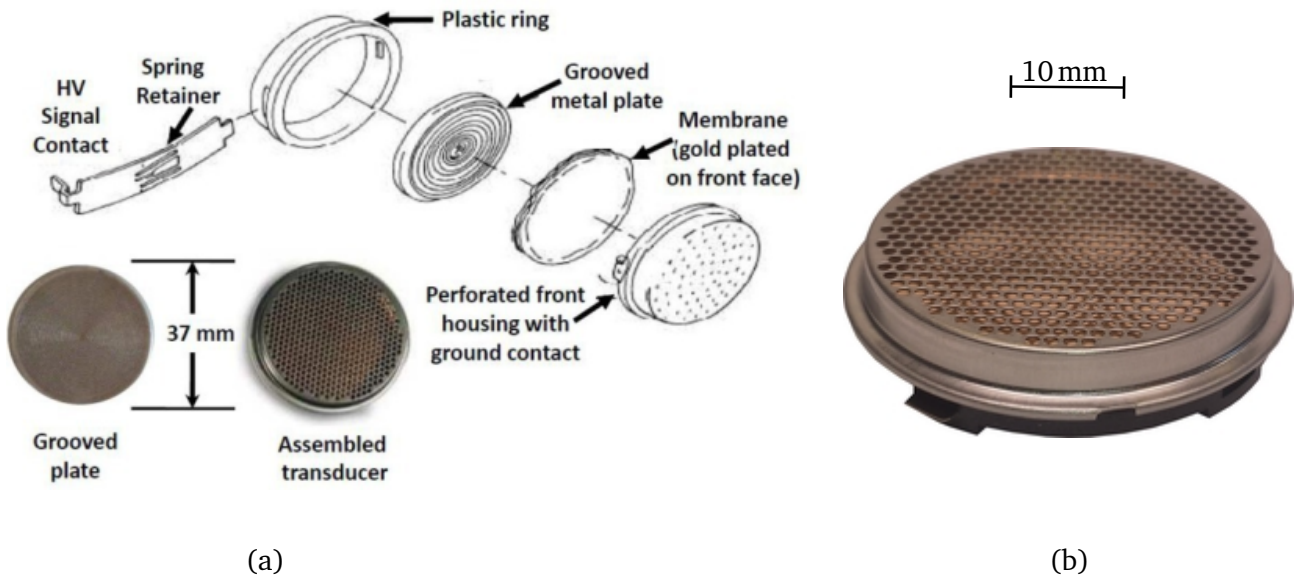


Figure 2.7: Exploded drawing of a CUT Series 600 SensComp, Copyright Polaroid™ manual 6500 Series Sonar Ranging Module (a) [37] and tilted view of a Series 600 SensComp 50 kHz ultrasonic transducer (b).

In contrast to the piezoelectric driven ultrasonic transducers (Chapter 2.2.1) the capacitive ultrasonic transducers need in addition to the AC excitation voltage a DC voltage, which is called DC-Bias or Bias voltage. It is used to increase the efficiency of those ultrasonic transducers and the DC-Bias voltage linearizes the CUTs around their operating point (Equation 2.4). For the SensComp 600 CUTs the recommended DC-Bias voltage is as high as the AC voltage, 200 V each, so AC+DC voltage is total of $400 V_p$ [37]. To apply this combination of AC+DC voltage a so called Bias-T is necessary [Chapter 3.1.1.2 Figure 3.4 (b)]. This AC+DC voltage is then responsible for an electrostatic force F_{el} , which lets the foil vibrating. In receiving mode the DC-Bias voltage is needed too, the sensitivity is increased and its response linearized.

Micromachined ultrasonic transducers (CMUTs) working with a similar principle such as CUTs. They also have two electrodes (plates) facing against each other. One is fixed and can not bend and the other one is thin and therefore flexible (bendable). The gap in between can be filled with air or can be evacuated and sealed keeping the vacuum. Unlike CUTs they are mostly made of silicon and are fabricated usually in a cleanroom. CMUTs are smaller by order of magnitudes. Usually their uniformity and reproducibility is good. This is possible because masking, lithography, etching, oxidation, and metalization is down scalable, well controllable and manageable on wafer level. Two main fabrication processes were established in the past 20 years. First, CMUT fabrication using sacrificial release method and second CMUT fabrication using wafer bonding.

The difficulty which is to overcome during a CMUT fabrication process is to build a cavity or gap with lateral dimensions between two plates [38]. Since the micro fabrication is good in structuring and building structured layer by layer on top of each other or etching structures into the silicon it is not possible to built something on nothing, to some extend and keeping in mind the properties of silicon and silicon dioxide. Therefore, a sacrificial layer or material is used to fill the gap and it used as kind of support structure before adding the counter plate silicon layer. This sacrificial layer is then dissolved with a proper etchant later. This process step reveals then the gap which is needed. There are some main issues regarding this method. The etchant is unfortunately not only dissolving the sacrificial layer but also the surrounding silicon structures e.g. top plate [38]. Due to this fact it is more difficult to achieve the needed thickness of the gap and plate. So it is affecting the resonance frequency and performance later, whose are dependent on those parameter. Furthermore, the uniformity and reproducibility is affected too. Also different materials lead to different material properties, for example compressive stress in sacrificial layer, which can simply destroy the silicon plate during the etch process releasing such stress [38].

To avoid those issues another process called wafer bonding or wafer fusion bonding is used [38]. Here the CMUT is structured in general on two wafers. One is structured with the back electrode, posts, and the gap [Figure 2.8 (a)], which is done with lithography, oxidation and etching. The other wafer is a special silicon on insulator wafer (SOI). It is fusion bonded to the first one. After this bonding step the handle layer of this second wafer and its buried oxide layer (BOX) is then removed [38]. In doing so the top plate as a silicon layer is now placed on top off the bottom wafer enclosing the gap. If this fusion bonding process is done in vacuum, then it is now encapsulated and sealed through the bonding step. So the top plate is already prestressed and therefore slightly deflected by the ambient pressure [Figure 2.8 (b)]. Finally a metalization layer is deposited and is acting as the top electrode, such as the CUT this top electrode is connected to ground.

Assuming the electrodes are parallel such as the plates of capacitor, the electrical energy W_{el} is calculated by [40], i.e.

$$W_{el} = \frac{1}{2}CV^2 = \frac{1}{2} \frac{\epsilon A}{d} E^2 d^2 = \frac{1}{2} \epsilon d A E^2 \quad (2.1)$$

where the permittivity ϵ is given by $\epsilon = \epsilon_0 \epsilon_r$ with ϵ_0 is the permittivity of vacuum and ϵ_r is the relative permittivity of the material, d is the distance between the electrodes, A is the area of an electrode, C as

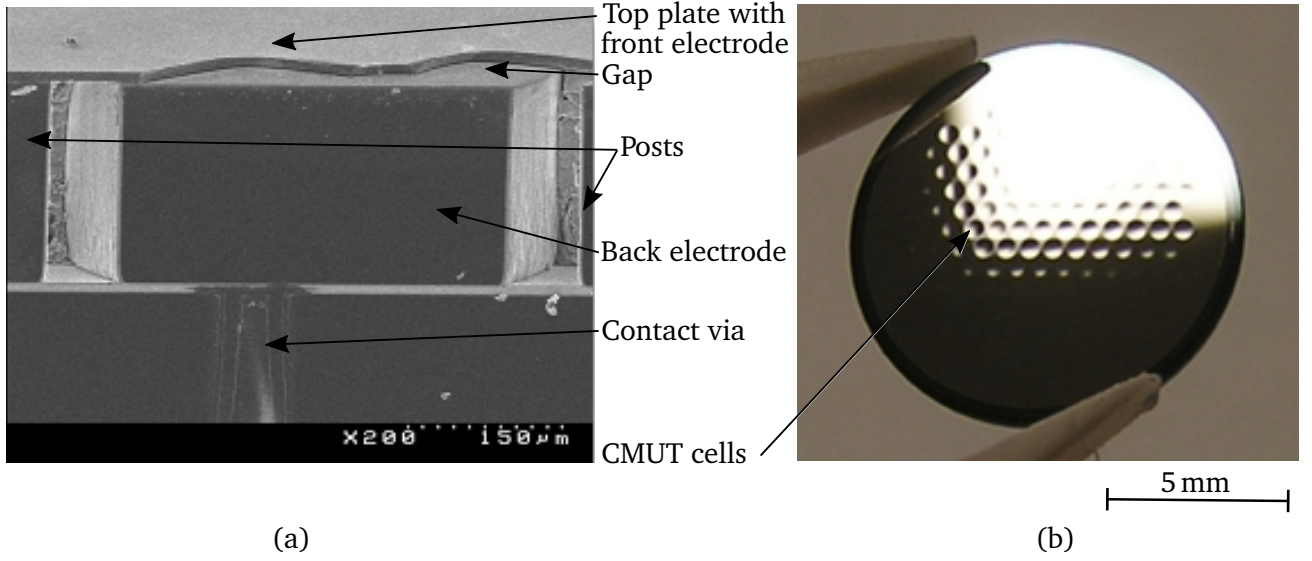


Figure 2.8: Scanning electron microscope (SEM) picture of one [Figure 2.8 (b)] capacitive micromachined ultrasonic transducer cell cut (a) [39] and a multi CMUT cell ultrasonic transducer array with 151 cells in parallel with resonance frequency of 330kHz, the deflection due to the ambient pressure (sealed vacuum) as a mechanical prestress is visible through light reflections (b) [39].

the capacitance with $C = \frac{\epsilon A}{d}$, and the electrical field $E = \frac{V}{d}$ with voltage V . Then the electrostatic force F_{el} can be calculated as the derivative of the electrical energy W_{el} after the distance (stretch s)

$$F_{el} = \frac{dW_{el}}{ds} = \frac{d}{ds} \left(\frac{1}{2} \epsilon d A E^2 \right) = \frac{1}{2} \epsilon A E^2 = \frac{1}{2} \epsilon A \frac{V^2}{d^2} \quad (2.2)$$

If now an AC voltage $V = V_{AC} \sin(\omega t)$ is applied (Equation 2.2) only then becomes clear that the CUT or

$$F_{el} = \frac{1}{2} \frac{\epsilon A}{d^2} [V_{AC} \sin(\omega t)]^2 = \frac{1}{2} \frac{\epsilon A}{d^2} \frac{1}{2} V_{AC}^2 [1 - \cos(2\omega t)] = \frac{1}{4} \frac{C^2 V_{AC}^2}{\epsilon A} [1 - \cos(2\omega t)] \quad (2.3)$$

CMUT is driven with a quadratic distortion with twice the frequency $V_{AC}^2 \cos(2\omega t)$ (Equation 2.3). But when an AC+DC voltage is applied $V = V_{DC} + V_{AC} \sin(\omega t)$ using equation 2.2 then

$$F_{el} = \frac{1}{2} \frac{\epsilon A}{d^2} [V_{DC} + V_{AC} \sin(\omega t)]^2 = \frac{1}{4} \frac{C^2}{\epsilon A} [2V_{DC}^2 + V_{AC}^2 + 4V_{DC}V_{AC} \sin(\omega t) - V_{AC}^2 \cos(2\omega t)] \quad (2.4)$$

the term $2V_{DC}^2 + V_{AC}^2$ is the static force component (Equation 2.4), the term $4V_{DC}V_{AC} \sin(\omega t)$ the V_{DC} bias voltage linearizes and magnifies (Equation 2.4) the CMUT because the V_{DC} bias voltage is usually higher voltages than the V_{AC} especially when driving CMUTs. The term $-V_{AC}^2 \cos(2\omega t)$ is still the quadratic distortion with twice the frequency (Equation 2.4). That is why capacitive ultrasonic transducers always need an additional DC-Bias voltage.

2.2.3 Ultrasonic Transducers Based on the Electromagnetic Principle

Electromagnetic acoustic transducers (EMATs) are only used for non-destructive testing (NDT) of solid materials, due to their work principle. Other than for piezoelectric ultrasonic transducers, no coupling fluid between test specimen and electromagnetic acoustic transducer is needed. The EMAT can touch but does not need to touch the surface of the test specimen [41]. Although proximity then is an advantage. There are two commonly active work principles when it comes to EMATs: transducers based on the Lorentz force and transducers based on the magnetostriction [42, 43].

First, electromagnetic ultrasonic transducers based on the Lorentz force. These are using two magnetic fields. One is a static or a quasi static magnetic field, which can be provided simply by a magnet or even a coil using direct current (DC). It is often referred to as the bias magnetic field [42]. The other magnetic field is generated through a coil, situated above a test specimen, using alternating current (AC) from 20 kHz to 100 MHz, which can be continuous waves or pulses [44]. Then the alternating magnetic field induces eddy currents into the surface of a test specimen. This induction will take place close to the surface and with increase of frequency the depth will decrease, due to the skin effect. So the test specimen must be a conducting and non-ferromagnetic material e.g. stainless steel, copper, or aluminum [42, 43]. The test specimen is part of an electromagnetic ultrasonic transducer. Next, the induced eddy currents will experience a force, the Lorentz force, due to the present bias magnetic field. So elastic deformation of the material occurs based on the Lorentz force. In such way ultrasonic waves are excited and propagate directly in the test specimen. Depending on the design of an EMAT, especially the shape of the AC coil, longitudinal, shear, Rayleigh, or lamb waves are excited [42].

Second, electromagnetic ultrasonic transducers based on the magnetostriction. When an EMAT is used with a ferromagnetic test specimen then the elastic deformation of the material occurs based on the magnetostriction. The Weiss domains of the ferromagnetic materials are interacting with the external alternating magnetic field [42]. They can shift and rotate according to the external magnetic field. A distortion takes place due to this rotation and the dimension of the material is changing in a range of $10 \frac{\mu\text{m}}{\text{m}}$ up to $2 \frac{\text{mm}}{\text{m}}$ at high magnetostrictive materials [45]. If magnetostriction happens at frequencies in the audible range this phenomena can even be heard e.g transformers humming. Again the test specimen becomes part of the EMAT. Otherwise no ultrasound can be generated.

2.3 Equivalent Circuit Model and its Parameter

Ultrasonic transducers and their behavior can be described mathematically using ordinary differential equations. Here analogies between the mechanical domain and the electrical domain are used. In doing so, complex network theory of the electrical domain with all its rules can be used to describe a mechanically system such as an ultrasonic transducer. Therefore, a better understanding is given and characterization of ultrasonic transducers can be done using lumped parameter models such as the Butterworth-van Dyke equivalent circuits and therefrom derived models (Chapter 4.1).

Ultrasonic transducers have a mechanically vibrating structures which is generating the ultrasound. This vibration or oscillation is driven or caused by several kinds of active working principle (Chapter 2). It

is well known that such mechanically oscillation can be described as spring-mass-damper system mathematically with differential equations [46, 47, 48]. Looking at a quartz crystal only by itself the applied harmonic force $F_0 \sin(\omega t)$ is given by the ordinary differential equation (ODE)

$$m \frac{d^2x}{dt^2} + d \frac{dx}{dt} + cx = F_0 \sin(\omega t), \quad (2.5)$$

where damping d , spring constant c , time t , angular frequency ω , and the displacement x of the center of the mass m . It is a fact that those differential equation and therefore behavior of a mechanical oscillator such as a quartz crystal oscillator can be described with differential equation using in analogy electrical basic components, resistance, inductance, and capacitance [47, 49, 50]. The differential equation must thereby be valid in both the mechanical and the electrical domain. Since the mechanical ODE uses the displacement x as the mutual quantity, the electrical ODE is then written with the charge Q as the mutual quantity by

$$L \frac{d^2Q}{dt^2} + R \frac{dQ}{dt} + \frac{Q}{C} = U_0 \sin(\omega t), \quad (2.6)$$

with inductance L , resistance R , capacitance C , time t , angular frequency ω and $U_0 \sin(\omega t)$ as the applied voltage. The applied force in mechanical domain which is responsible for the displacement and the applied voltage in the electrical domain which is responsible for the movement of the charges in a wire.

There are basically two known analogies [16, 47, 51]. Analogy of the first art which is used for impedance fidelity (Table 2.1) and the second art which is used when circuit fidelity is needed. This implies obviously that the first art analogy has no circuit fidelity a parallel resonance circuit exchanges with a series resonance circuits and vice versa. The second analogy leads to a reciprocity of the impedance. These are generally interchangeable without any compromises [16]. In this work the first analogy is used (Table 2.1).

The ODE 2.6 describes a RLC series resonance circuit. This is obviously not enough to describe a quartz crystal or piezoelectric layer with electrodes, which are always necessary for electrical connection. Adding electrodes the quartz or piezo layer acts as a dielectric layer in between, which leads to a capacitive behavior. Therefore a parallel capacitance C_p has to be added in parallel to the RLC circuit.

Stephen Butterworth and Karl Skillmann van Dyke developed independently this equivalent circuit with lumped parameters [46, 49]. In reason of that, the Butterworth-van Dyke (BvD) model (Figure 2.9) as equivalent circuit is common and is used as a description of quartz crystal resonators or piezoelectric disks. Annotation, sometimes ultrasonic transducer especially piezoelectric driven one are also described using the Mason model which includes mechanical coupling. But only if the thickness mode is used and the lateral dimension is a multiple of there wavelength [16, 47]. Furthermore, the basic BvD model or the 4-elements equivalent circuit is often extended with more lumped parameters. Those extended models are discussed in chapter 4.1.

In general the Butterworth-van Dyke (BvD) model uses concentrated electrical devices to describe ultrasonic transducer disregarding of the actual working principle e.g. piezoelectric, electrostatic or

Table 2.1: Analogy of mechanical and electrical parameters using impedance fidelity [16, 47, 51].

Meachanical	Symbol		Symbol	Electrical
Mass	m	\longleftrightarrow	L	Inductance
Damping	d	\longleftrightarrow	R	Resistance
Spring constant	c	\longleftrightarrow	$1/C$	1/Capacitance
Force	F_0	\longleftrightarrow	V_0	Voltage
Displacement (Deflection)	x	\longleftrightarrow	Q	Charge
Velocity	$\dot{x} = \frac{dx}{dt} = v$	\longleftrightarrow	$\dot{Q} = \frac{dQ}{dt} = i$	Current
Acceleration	$\ddot{x} = \frac{d^2x}{dt^2} = \dot{v} = \frac{dv}{dt} = a$	\longleftrightarrow	$\ddot{Q} = \frac{d^2Q}{dt^2} = \frac{di}{dt}$	Accelerated Charge

electromagnetic. Therefore electrical network theory can be used for calculation of the steady state solution.

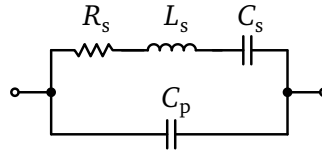


Figure 2.9: Butterworth-van Dyke model with R_s, L_s, C_s in series as the mechanical or acoustic branch describing a quartz crystal by itself and C_p as the electrical branch which describes the electrical connections e.g. electrodes [46, 49].

So the complex impedance $\underline{Z} = R + jX$ is then calculated by

$$\underline{Z} = \underline{Z}_{\text{series}} \parallel \underline{Z}_{\text{parallel}} = \frac{1}{\underline{Y}} = \frac{1}{\underline{Y}_{\text{series}} + \underline{Y}_{\text{parallel}}}, \quad (2.7)$$

where R is the resistance, X is the reactance, $\underline{Y} = G + jB$ is the complex admittance with G as the conductance, B as the susceptance, and j as the imaginary unit. The series impedance $\underline{Z}_{\text{series}}$ is given with

$$\underline{Z}_{\text{series}} = R_s + j \left(\omega L_s - \frac{1}{\omega C_s} \right) \quad (2.8)$$

and the parallel impedance $\underline{Z}_{\text{parallel}}$ is given with

$$\underline{Z}_{\text{parallel}} = \frac{1}{j\omega C_p}, \quad (2.9)$$

where ω is the angular frequency, R_s is the resistance, L_s is the inductance, and C_s is the capacitance of the series branch of the BvD model (Figure 2.9). Combining then equation 2.7 with 2.8 and 2.9 gives

$$\underline{Z} = \frac{\left(\omega L_s - \frac{1}{\omega C_s} \right) - jR_s}{\omega R_s C_p + j \left(\omega^2 L_s C_p - \frac{C_p}{C_s} - 1 \right)} \quad (2.10)$$

as the complex impedance of the BvD model.

Plotting the magnitude $|Z|$ and the phase φ_z over the frequency of the BvD model (Figure 2.10) gives the same result such as an impedance measurement of this device (Chapter 3.1). Hence, conducting an electrical impedance measurement and analyzing the data provides many important parameter of the DUT, the ultrasonic transducer. In order to gather the parameter with an automatic parameter extraction (Chapter 4) it is necessary to have a good model and a robust complex curve fit algorithm (Chapter 4.3).

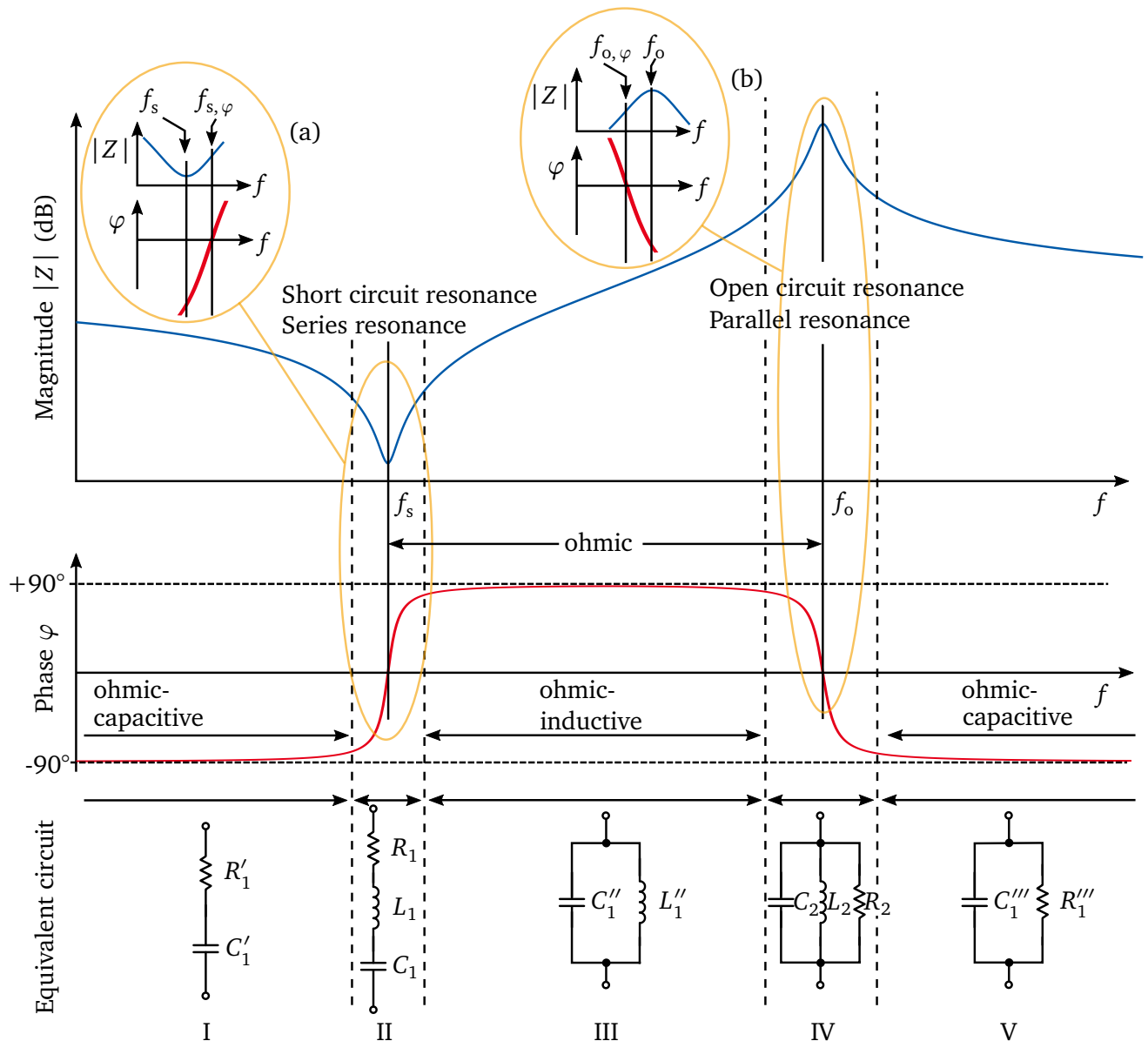


Figure 2.10: Butterworth-van Dyke model with magnitude $|Z|$, the phase φ_z and important equivalent circuit model describing the behavior in several regions (I-V) of interests [30, 52]. The inlets show the discrepancy of f_s (a) and f_s (b) when the damping R_s has to be considered.

The BvD model is a powerful analytic model, which provides many parameters of an ultrasonic transducer and its electrical impedance behavior. Looking closely at the BvD model of an ultrasonic transducer then the frequency range can be distinguished into five regions of interests.

First, at frequencies below the short circuit resonance (Figure 2.10 I) and at frequencies above the open circuit resonance (Figure 2.10 V) when the ultrasonic transducer mostly becomes ohmic-capacitive. The phase φ is here usually negative and reaches down to minimum of -90° . The equivalent circuits can be either described as series of $R'C'$ or as parallel of $R''C''$ and are interchangeable [52].

Second, between the short and open circuit resonance frequency an ultrasonic transducer becomes ohmic-inductive (Figure 2.10 III). Here the phase φ is usually positive and can reach up to a maximum of $+90^\circ$ if a powerful ultrasonic transducer is considered. The equivalent circuit can be described as parallel of $C''L''$, which is again interchangeable with both elements in series [52].

Thirdly, most important regions of interest are the short circuit resonance (Figure 2.10 II) and open circuit resonance (Figure 2.10 IV). Here the ultrasonic transducer is used for transmitting respectively receiving ultrasound. In both cases of resonance the ultrasonic transducer is completely ohmic if no damping is present [52].

When operating an ultrasonic transducer in transmit mode, at its short circuit resonance frequency, it is usually connected to a low impedance driving source e.g. waveform generator or amplifier. In doing so the parallel capacitance of the BvD and thereby the ultrasonic transducer is shorted. At its short circuit resonance frequency f_s (Figure 2.10) the magnitude of the impedance is at its minimum. Thus the ultrasonic transducer draws maximum energy and has its maximum displacement. The short circuit resonance frequency f_s is calculated by

$$f_s = \frac{\omega_s}{2\pi} = \frac{1}{2\pi\sqrt{L_s C_s}}, \quad (2.11)$$

setting the reactance, the imaginary part, of $\underline{Z}_{\text{series}}$ (Equation 2.8) to zero, due to the condition of resonance [53], and solving for ω_s .

When operating an ultrasonic transducer in receive mode, at its open circuit resonance frequency, it is usually connected to a high impedance input of an amplifier. So the BvD model and thereby the ultrasonic transducer is working as an open circuit (Figure 2.10) at high impedance matching the impedance of the amplifier. The open circuit resonance frequency f_o is calculated by

$$f_o = \frac{\omega_o}{2\pi} = \frac{1}{2\pi\sqrt{L_s \frac{C_s C_p}{C_s + C_p}}}, \quad (2.12)$$

again setting the reactance, imaginary part, of $\underline{Z}_{\text{series}}$ (Equation 2.8) to zero and solving for ω_o . But this time the parallel capacitance C_p has to be considered as well. Due to the high impedance connection into an amplifier no current flow is assumed, and, therefore, C_s and C_p are treated as connected in series. Both equations 2.11 and 2.12 give for most ultrasonic transducers good approximations for their short circuit f_s and open circuit f_o resonances.

However, using these calculations the short circuit resonance is lower than the short circuit resonance indicated by the zero crossing of the phase $f_{s,\varphi}$ [Figure 2.10 inlet (a)]. Also the calculated open circuit resonance is higher than the open circuit resonance indicated by the second zero crossing of the phase

$f_{o,\varphi}$ [Figure 2.10 inlet (b)]. For a correct calculation of both frequencies the entire imaginary part of the complex impedance (Equation 2.10) has to be solved for ω by

$$\omega \rightarrow \frac{C_s(\omega^2 L_s C_s - 1) - C_p \{1 + \omega^2 C_s [C_s R_s^2 + L_s(\omega^2 L_s C_s - 2)]\}}{\omega(C_s + C_p)^2 + \omega^3 C_s C_p [C_s C_p R_s^2 - 2L_s(C_s + C_p)] + \omega^5 L_s^2 C_s^2 C_p^2} \stackrel{!}{=} 0. \quad (2.13)$$

Using Mathematica 11.0.1.0 (Wolfram Research, Inc., Champaign, IL, USA) to calculate the imaginary part (Equation 2.13) and solving it analytically for ω gives two valid solutions for the exact resonances ω_s with

$$\omega_s^2 = \frac{1}{L_s C_s} - \frac{R_s^2}{2L_s^2} + \frac{1}{2L_s C_p} \left(1 - \sqrt{1 + \frac{R_s^4 C_p^2}{L_s^2} - \frac{4R_s^2 C_p^2}{L_s C_s} - \frac{2R_s^2 C_p}{L_s}} \right) \quad (2.14)$$

and ω_o with

$$\omega_o^2 = \frac{1}{L_s C_s} - \frac{R_s^2}{2L_s^2} + \frac{1}{2L_s C_p} \left(1 + \sqrt{1 + \frac{R_s^4 C_p^2}{L_s^2} - \frac{4R_s^2 C_p^2}{L_s C_s} - \frac{2R_s^2 C_p}{L_s}} \right) \quad (2.15)$$

at phase zero. Solutions for negative angular resonance frequency of $\omega_s = \pm\sqrt{\omega_s^2}$ and $\omega_o = \pm\sqrt{\omega_o^2}$ are neglected, since they have no physical meaning. Studying equation 2.14 and 2.14 shows the influence of the resistance R_s . In case of a quartz crystal with high quality factor of Q up to 500,000 [54] the resistance is negligibly small. Assuming this fact and setting therefore $R_s = 0$ than equation 2.14 becomes simplified to

$$\begin{aligned} \omega_o^2 &= \frac{1}{L_s C_s} + \frac{1}{2L_s C_p} (1 - \sqrt{1}) \\ &= \frac{1}{L_s C_s} + \frac{1}{2L_s C_p} - \frac{1}{2L_s C_p} \\ &= \frac{1}{L_s C_s}. \end{aligned} \quad (2.16)$$

In doing so the short circuit resonance frequency (Equation 2.11) can be found with $\omega = 2\pi f_s$. Also setting $R_s = 0$ than equation 2.15 becomes simplified to

$$\begin{aligned} \omega_s^2 &= \frac{1}{L_s C_s} + \frac{1}{2L_s C_p} (1 + \sqrt{1}) \\ &= \frac{1}{L_s C_s} + \frac{1}{2L_s C_p} + \frac{1}{2L_s C_p} \\ &= \frac{1}{L_s C_s} + \frac{1}{L_s C_p} \\ &= \frac{C_p + C_s}{L_s C_s C_p} \\ &= \frac{1}{L_s \frac{C_p C_s}{C_s + C_p}}. \end{aligned} \quad (2.17)$$

So the open circuit resonance frequency (Equation 2.12) can be found with $\omega = 2\pi f_0$. To conclude, the error of the calculated resonance frequencies depends on the ultrasonic transducer type and its quality factor. So for narrow band ultrasonic transducers the error will be smaller than for ultrasonic transducers which are more broad band. Narrow band means the ultrasonic transducer has a high quality factor Q . Thus broadband means the ultrasonic transducer has a low quality factor Q .

The quality factor Q can be defined in a variety of different ways. According to Hunt [55] the most fundamental explanation is that Q_m the mechanical quality factor is [52, 55]

$$Q_m = 2\pi \frac{\text{Energy stored}}{\text{Energy dissipated}} = 2\pi \frac{E_s}{E_d} \quad (2.18)$$

in a transducer during one full period cycle. Again using the analogy of the electrical circuit theory the quality factor Q_1 of a series resonance (Figure 2.10 II) it can also be calculated by [52]

$$Q_1 = \frac{1}{R_1} \sqrt{\frac{L_1}{C_1}}. \quad (2.19)$$

In case of a parallel resonance circuit (Figure 2.10 IV) the quality factor Q_2 is given by [52]

$$Q_2 = R_2 \sqrt{\frac{C_2}{L_2}}. \quad (2.20)$$

Hence equations 2.19 and 2.20 are only valid for a resonator which can vibrate freely such as hanging in air and is non loaded [52].

Since ultrasonic transducers usually have loaded structures, e.g. piezo-ceramic is sputtered on a plate or piezo-ceramic disks are clamped with a bolt (Chapter 2.2.1) another way can be used for the calculation of the quality factors. In general the quality factor Q can be calculated by [56]

$$Q = \frac{f_0}{BW} = \frac{f_0}{f_2 - f_1}, \quad (2.21)$$

where f_0 is the resonance frequency, f_1 lower cut off frequency and f_2 upper cut off frequency left and right at $\pm 3\text{dB}$ of the magnitude of the impedance at the resonance frequency. Usually is $f_2 > f_1$ and therewith the bandwidth $BW = f_2 - f_1$ is calculated. In case of a symmetric undamped waveform f_0 is also often refereed as the center frequency and the lower respectively upper cut off frequency f_1, f_2 are in equal distance of it. Ultrasonic transducers have two resonance frequencies, therefore also two quality factors and two bandwidths respectively. Due to the mutual interferences of both resonances, ultrasonic transducers mostly do not have symmetrical cut off frequencies. Looking at short resonance thus the quality factor is calculated by

$$Q_s = \frac{f_s}{BW_s} \quad (2.22)$$

with its bandwidth

$$BW_s = f_{s,2,+3\text{dB}} - f_{s,1,+3\text{dB}} \quad (2.23)$$

Here the bandwidth is given by frequencies $f_{s,2,1}$ at +3 dB from the minimum of the magnitude of the impedance. The quality factor of the open circuit resonance is calculated similarly by

$$Q_o = \frac{f_o}{BW_o} \quad (2.24)$$

Since the magnitude of the impedance has its maximum at the open circuit resonance, the bandwidth is given by the frequencies $f_{s,2,1}$ at -3 dB from this maximum, i.e.

$$BW_o = f_{o,2,-3\text{dB}} - f_{o,1,-3\text{dB}} \quad (2.25)$$

In doing so, both quality factors can be obtained out of the measured electrical impedance (Chapter 3.1) which can be conducted under thermal load or with higher excitation voltages.

Next important parameter of ultrasonic transducers is their electromechanical coupling efficiency k_{eff} , which is indicating the performance of energy transfer from one domain to another, from electrical to mechanical. Therewith using the mechanical one to generate ultrasound, via vibrational structures, in the acoustical domain. The coupling coefficient is defined by following equations [55]

$$k_{\text{eff}}^2 = 1 - \left(\frac{f_o}{f_s}\right)^2 \quad (2.26)$$

for electromagnetic coupling and

$$k_{\text{eff}}^2 = 1 - \left(\frac{f_s}{f_o}\right)^2 \quad (2.27)$$

for electrostatic coupling. An ultrasonic transducer becomes more efficient the more apart the short circuit resonance frequency is from the open circuit resonance frequency is.

2.4 Separation of the Acoustic Aperture

In general almost every ultrasonic transducers except EMATs generate ultrasound with a vibrating structure. As described before this can be a disk, a plate, or a membrane. At the same time the dimensions, the shape and the properties of the vibrating structures are responsible for the characteristics of the emitted ultrasonic wave, so the acoustic characteristics. Acoustic characteristics such as the shape and width of the beam or the presents of side lobes, to name only a few. Furthermore the ultrasonic wave (ultrasonic sound wave) is direct emitted from this vibrating structure. In this case the vibrating structure is the same as the acoustic aperture. So the ultrasonic sound wave is coming out of it.

But looking besides ultrasonic transducers into other fields of sound generation in general, interesting approaches and solutions can be found. Thereby it does not matter whether it is a technical field or looking at mother nature. In many cases the vibrating structure, the sound generating one, is not equal with the acoustic aperture, the opening where the sound wave comes out.

For example most of the wind instruments, if not all, have a separation of the vibration tone or sound generating structure and the acoustic aperture, the opening. Thinking here of trumpets, tuba, or flute for example. Here the acoustic aperture is often an exponential or hyperbolic shaped horn opening, which can be seen as an acoustic impedance transformer [57]. It allows the transformation of the sound pressure level into the acoustic particle velocity in an efficient way. Therewith goes along an increasing of the volume. By minimizing reflections, which could otherwise occur due to an acoustical impedance mismatch.

Looking into mother nature and the human anatomy, the voice or sound generation takes place at the vocal cords. They are the vibrating structure and are located down in the throat (Figure 2.11) [23]. However the acoustic aperture is the mouth opening with the lips (Figure 2.11). It is a complex structure with resonator cavities and sound waveguides, but also here the vibrating structure is separated from the acoustic aperture.

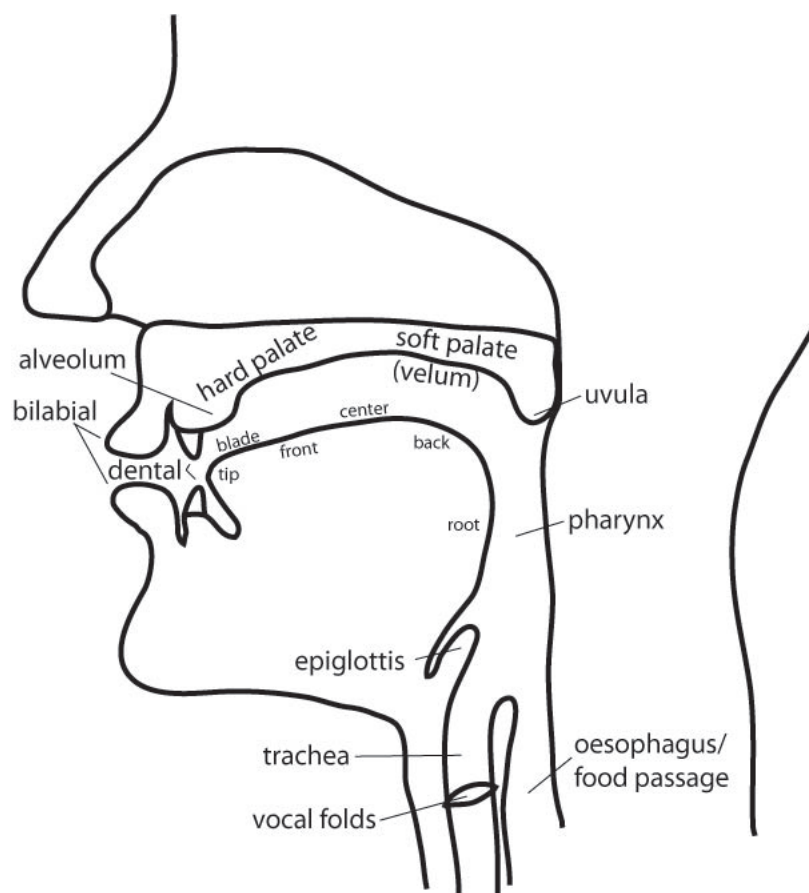


Figure 2.11: An example of a separation of sound generating structure and the acoustic aperture. At the complex vocal tract of a human, the sound generating structure, the vibrating vocal cords, the vocal folds, are located down in the throat. The acoustic aperture however is the opening of the mouth, the lips. Copyright 2013 B. V. Tucker [23].

In the field of ultrasonic transducers, waveguides were investigated in a previous work done in 1993. Langen describes a process of development for ultrasonic sensors based on the waveguides [24], which are then being used in automation and robotic industry. An ultrasonic transducer generates the ultrasound, the vibrating structure, into a compression chamber with a first aperture at its end, followed by a waveguide and then the second aperture which is the opening [24]. The compression chamber in combination with the first aperture increases the acoustical impedance, such as a Helmholtz-Resonator. So the attached ultrasonic transducer couples more acoustic energy through the first aperture into the waveguide [24]. Overall the vibrating structure, the ultrasonic transducer, is separated from the aperture, the opening, through a waveguide and so the acoustic properties can be manipulated.

A similar but even simpler approach of this, to build a single line phased array, which consists of six MA40S4S (Murata Manufacturing Co. Ltd., Higashikotari, Kyōto, Japan) ultrasonic transducers was used by Takahashi et al. in 2007. In this work the dimension of 10 mm Murata ultrasonic transducers were reduced by polyvinyl chloride (PVC) sound tubes [25] to achieve half wavelength criteria. They also separate the vibrating aperture from the acoustic aperture.

Looking into these fields several advantages for ultrasonic transducers can be identified. First, the addition of the degree of freedom for shaping the new acoustic aperture and therefore manipulating the properties of the sound beam. Second, using this approach for harsh environments such as high temperature ones. Due to the separation, with the waveguide the ultrasonic transducers can be protected against the harsh media building simply a temperature gradient by passive cooling through distance or even active cooling. Third, in the field of array applications almost every type and size of ultrasonic transducer can be used with waveguides and therewith the half wavelength criteria can be achieved. In chapter 5 the approach of separation using waveguides is shown with such a prototype 1 D air coupled phased array.

3 Methods of Characterization

This chapter describes several methods of characterization of ultrasonic transducers. Starting with an electrical impedance measurement, calibrated with a network analyzer and a non-calibrated with higher excitation voltages using a function generator and oscilloscope. The investigation of the electrical impedance is done over a wide temperature range from -190°C to $+250^{\circ}\text{C}$ and two setups are described to achieve these test conditions. Furthermore the measurement of the surface velocity and sound pressure levels are also essential for ultrasonic transducer characterization. A volumetric acoustic sound pressure scan and a Schlieren setup are used to visualize the acoustic field in front of the transducers.

3.1 Electrical Impedance Measurements

The electrical impedance measurement is one of the most essential tools for first characterization. It is a quick and accurate measurement at the same time. These measurements can be done at the very end of a transducer assembly, as well as direct on waver level during a CMUT production as example using a prober.

"Impedance Z is generally defined as the total opposition a device or circuit offers to the flow of an alternating current (AC) at a given frequency." [58].

Overall there are many measurement methods to obtain an unknown impedance $Z_x = R_x + jX_x$ of a device under test (DUT). Where R_x is the real part as resistance and an imaginary part as reactance X_x indicated via j as imaginary unit. So the complex impedance is as a vector in the complex plane. It consists of an absolute value, its length, and its phase angle $\varphi_x = \arctan\left(\frac{X_x}{R_x}\right)$, which gives the direction. Knowing this fact that impedance is a complex quantity, it is important that two values have to be measured. Obviously with advantages and disadvantages in ease of use, frequency range, accuracy and measurements conditions. There are basically six impedance measurement methods which are commonly used. Bridge method, resonant method, I-V method, RF I-V method for low and high impedance, network analysis method [58].

The bridge method uses a regular bridge circuit layout but with different combinations of inductors, capacitors and resistors. By varying these components an unknown impedance Z_x can be obtained in relationship to the given components by matching these. The bridge method is most accurate (0.1% typ.) one for frequencies up to 300 MHz [58]. But there is a drawback, it needs to be manually balanced, which is a non practical approach for automatic measurements with a high throughput. However, there are analyzers on the market, which can perform an auto-balancing by them self, but such a device is not available in the research laboratory at the time this research was done.

Using the resonant method a DUT is in resonance by adjusting a tuning capacitor in an oscillating circuit. By doing so Z_x can be recalculated using frequency, tuned capacitance value and measured Q value direct

at the capacitor. This method can be used up to $Q \approx 300$ and frequencies up to 70 MHz [58]. Again this method needs to be manually tuned and it has a low impedance measurement accuracy [58].

The I-V method uses measured voltage and current to calculate the impedance Z_x . Current is again calculated with Ohms law by measuring the voltage across a well known low ohmic resistor. It is an accurate technique from 40 Hz and above [59]. Instead of a resistor a low loss transformer can be used to prevent any influence a resistor would do to the DUT circuit. However, due to this low loss transformer I-V method has its limits in low frequency range [58].

Next method is an extension of the I-V method. Radio frequency or RF I-V method is based on the same principle. But the impedance is matched to 50 Ω circuit and can measure impedance from 100 MHz up to 3 GHz [58]. There are two different configurations of voltmeter and current meter for measuring the impedance. One is for low impedance DUTs and another for high impedance DUTs. As a rule of thumb below 1 k Ω is low impedance and above 100 k Ω the DUT is high impedance [58]. The range in between is a kind of soft transition, so there is no exact number as a switching point.

From 3 GHz and up, the network analysis method is commonly used. Basically it measures the reflection at the DUT using a directional coupler or bridge. In doing so the reflection coefficient is the ratio of an incident signal to the reflected signal. For more detailed information please see "Impedance Handbook" [58].

Since all measurements were performed with the I-V method, the focus is now on this method. The complex impedance \underline{Z} is defined by Ohms law

$$\underline{Z} = \frac{\underline{v}}{\underline{i}}, \quad (3.1)$$

where \underline{v} is the instantaneous value of an alternating voltage defined by

$$\underline{v} = \hat{v} [\cos(\omega t + \varphi_v) + j \sin(\omega t + \varphi_v)] = \hat{v} e^{j(\omega t + \varphi_v)} \quad (3.2)$$

and \underline{i} is the instantaneous value of the alternating current with

$$\underline{i} = \hat{i} [\cos(\omega t + \varphi_i) + j \sin(\omega t + \varphi_i)] = \hat{i} e^{j(\omega t + \varphi_i)}. \quad (3.3)$$

Hereby is $\omega = 2\pi f$ the angular frequency with frequency f itself and t is time. Then electrical impedance Z is calculated by the absolute value of the complex impedance

$$Z = |\underline{Z}|. \quad (3.4)$$

In case of periodic harmonic signals such as a sinusoidal signal and using rules of complex calculating theory for alternating current, Z can be simply calculated by

$$Z = |Z| = \frac{\hat{v}}{\hat{i}} = \frac{V_{\text{RMS}}}{I_{\text{RMS}}}, \quad (3.5)$$

with $\hat{v} = \sqrt{2}V_{\text{RMS}}$ and $\hat{i} = \sqrt{2}I_{\text{RMS}}$ as the amplitude or peak values of voltage and current. Where U_{RMS} and I_{RMS} correspond to root mean square (RMS) value of each signal. It does not matter whether amplitude or RMS is used, because the crest factor of $\sqrt{2} \approx 1.414$ for sinusoidal is canceling out. The phase angle φ_x is calculated by the difference of phase angles, i.e.

$$\varphi_x = \varphi_v - \varphi_i \quad (3.6)$$

of voltage and current.

3.1.1 Measurement Setup Network Analyzer

Many impedance measurements are performed using a dedicated impedance analyzer or a network analyzer which also can feature an impedance measurement as an option. In this work most of the impedance measurements were conducted with the Keysight Network Analyzer E5061B-3L5 with impedance analysis function 3L5 as option (KEYSIGHT TECHNOLOGIES, Santa Rosa, CA, USA). Additionally, a test fixture Keysight 16047E (KEYSIGHT TECHNOLOGIES, Santa Rosa, CA, USA) for leaded components, a 16034E test fixture for surface mounted devices (SMD), a 16089B test fixture with Kelvin Clip Leads, or 16334A with extension cables equipped with a tweezer are required. Also measurements were conducted with Anritsu MS4630B Network Analyzer using a PI-Network MA1506A (Anritsu Cooperation, Atsugi, Kanadawa Prefecture, Japan).

Both network analyzers require a warm up time and a calibration before measurements [60, 61]. The calibration procedure is described for the Keysight E5061B-3L5 Network Analyzer only. After a warm up time of 90 min [60] and before calibration all settings for impedance measurements are entered and an appropriate test fixture is connected. The measurement method is set to *Gain-Phase-Series-Thru* which enables the impedance analyzes from 5 Hz to 30 MHz. Next *Channel1 Trace1* is set to $|Z|$ and *Trace2* is set to $\varphi(Z)$. The input impedance of the network analyzer is set to $50\ \Omega$ or $1\ \text{M}\Omega$ and the attenuation is set to 0 dB or 20 dB. For impedance measurement of piezos typically T is set to $50\ \Omega$ 20 dB, R is set to $1\ \text{M}\Omega$ 20 dB [60], where T stands for transmission (current) input and R stands for reflection (voltage) input. Next, the source power is set to desired level ranging from $-30\ \text{dBm}$ to $10\ \text{dBm}$ or $3.556\ \text{mV}_{\text{pp}}$ to $2\ \text{V}_{\text{pp}}$ at $50\ \Omega$ respectively. Then frequency range, intermediate frequency band with (IFBW), number of points (*min* 201 – *max* 1601 points [60]), and sweep time is set to desired needs fitting the DUT. The 2-port calibration is performed in three steps open, short, and load (low loss capacitance optional).

First, for an open calibration set the connectors (*HIGH*, *LOW*) is a defined state. Each contact should be closed but not shortened by a bridge [Figure 3.1 (a)]. Now, the open compensation data can be obtained. These are used to reduce or eliminate stray capacitance [59]. This is only valid if an open compensation impedance value of 100 times greater than the maximum DUT impedance can be achieved [59].

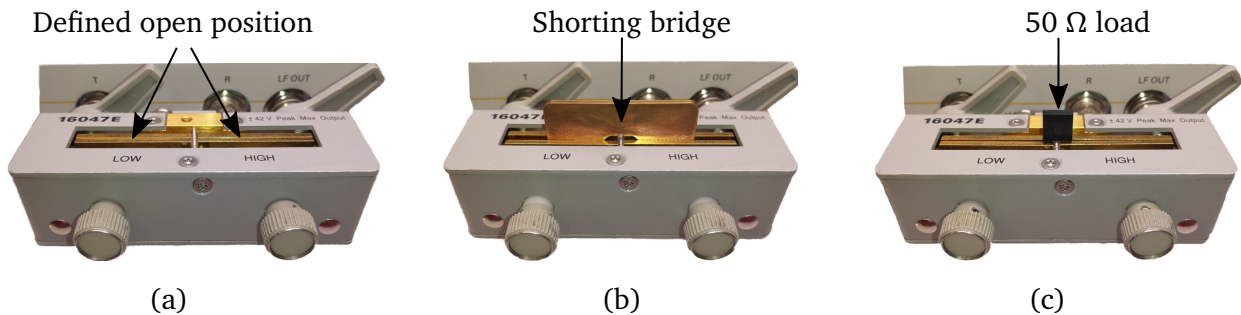


Figure 3.1: Calibration of the Keysight 16047E test fixture for leaded DUT, in open calibration the connectors (*HIGHT*, *LOW*) should be in a defined position (a) e.g. closed, during short calibration the shorting bridge should be cleaned and inserted completely (b), for load calibration a precise $50\ \Omega$ resistor should also be inserted completely (c), to avoid parasitics [60].

Second, for a short calibration the connectors (*HIGH*, *LOW*) are shorted by a bridge [Figure 3.1 (b)]. Now, the short compensation data can be obtained. These are used to reduce or eliminate resistance and inductance [59]. This is only valid if a short compensation impedance value of 100 times smaller than the minimum DUT impedance can be achieved [59].

Third, for a load calibration a precision $50\ \Omega \pm 0.01\%$ resistor is connected to the connectors (*HIGH*, *LOW*) as load and as low as possible, to avoid any parasitics inductance or capacitance [Figure 3.1 (c)]. Now, the load compensation data can be obtained. These are used to reduce the influence of passive circuit or components (e.g. Bias-T) or when the measurement port is extended [59].

Optional a low loss capacitor calibration can be performed, too. Note all measurements were conducted using calibration step open, short, and load only. After calibration is done all compensation data are only valid for mentioned boundary condition and chosen frequency range. This implies that if e.g. the frequency range changes, the entire setup has to be re-calibrated. Note, when measurements at higher frequency are conducted then the impedance measurements are even more sensitive to the change of temperature or humidity for instance and a re-calibration should be done more frequently [58]. In doing so a long term steady performance is more likely given. However, a successfully calibration does not reduces or eliminate the given measurement uncertainties of the measurements. So a frequency dependent measurement uncertainty calculation has to be done.

3.1.1.1 Measurement Uncertainty

The measurement uncertainty of the Keysight E5061B-3L5 Network Analyzer can be found as supplemental performance data (SPD) in its data sheet [60]. When using a test fixture such as the Keysight 16047E an additional error has to be considered, supplemental performance characteristics (SPC) can be found in its data sheet [62]. The measurement uncertainty is a combined frequency f and measured impedance Z_m dependent calculation [60]. Where impedance accuracy $[Z_a] = \%$ is calculated [Figure 3.2 (a)] by [60]

$$Z_a = A + \left(\frac{B}{|Z_m|} + C|Z_m| \right) 100\%, \quad (3.7)$$

using A as basic accuracy given in $[A] = \%$, B as short offset given in $[B] = \text{m}\Omega$, and C as open offset given in $[C] = \mu\text{S}$. Where the basic accuracy is calculated by

$$A = \begin{cases} 2 & \text{if } 5 \text{ Hz} \leq f < 1 \text{ MHz} \\ 2 + 0.15 \frac{F_2}{1 \text{ MHz}} & \text{if } 1 \text{ MHz} \leq f \leq 30 \text{ MHz}, \end{cases} \quad (3.8)$$

the short offset is calculated with

$$B = \text{m}\Omega \begin{cases} 500 \left(\sqrt{\frac{1 \text{ kHz}}{F_1}} \right) & \text{if } 5 \text{ Hz} \leq f < 1 \text{ kHz} \\ 500 & \text{if } 1 \text{ kHz} \leq f < 100 \text{ kHz} \\ 250 & \text{if } 100 \text{ kHz} \leq f \leq 30 \text{ MHz}, \end{cases} \quad (3.9)$$

and the open offset is then calculated by

$$C = \mu\text{S} \begin{cases} 6 \left(\sqrt{\frac{1 \text{ kHz}}{F_1}} \right) & \text{if } 5 \text{ Hz} \leq f < 1 \text{ kHz} \\ 6 & \text{if } 1 \text{ kHz} \leq f < 100 \text{ kHz} \\ 2 & \text{if } 100 \text{ kHz} \leq f \leq 30 \text{ MHz}, \end{cases} \quad (3.10)$$

with $[F_1] = \text{kHz}$ and $[F_2] = \text{MHz}$ [60]. Once, the impedance accuracy Z_a is calculated it can be used to calculate phase accuracy $\varphi_{z,a}$ by

$$\varphi_{z,a} = \arcsin\left(\frac{Z_a}{100}\right), \quad (3.11)$$

with $[\varphi_{z,a}] = \text{rad}$ [Figure 3.2 (b)]. Both measurement uncertainties equations 3.7 and 3.11 are only valid for the chosen settings of input impedance and attenuation of T, R [60].

Since, an additional test fixture is required for almost all impedance measurements, also an additional measurement uncertainty has to be calculated. Following equations are only valid for Keysight 16047E

test fixture. The measured impedance uncertainty $[Z_{a, \text{fixture}}] = \%$ of the test fixture [Figure 3.3 (a)] is calculated by

$$Z_{a, \text{fixture}} = \pm \left[D + \left(\frac{Z_s}{Z_m} + Y_o Z_m \right) 100\% \right], \quad (3.12)$$

where D additional error is given in $[D] = \%$, $[Y_o]$ as the open repeatability of the admittance given in $[Y_o] = \text{S}$, Z_s as the short repeatability of the impedance given in $[Z_s] = \Omega$, and Z_m is the measured impedance. The open repeatability is then calculated by

$$Y_o = 2 \text{ nS} + 10 \mu\text{S} \frac{f}{100 \text{ MHz}}, \quad (3.13)$$

the short repeatability is calculated by

$$Z_s = 2 \text{ m}\Omega + 600 \text{ m}\Omega \frac{f}{100 \text{ MHz}}, \quad (3.14)$$

and the additional error is calculated by

$$D = \begin{cases} 0.2\% \frac{f^2}{100 \text{ MHz}} & \text{if } f \leq 15 \text{ MHz} \\ 4.0\% \frac{f}{100 \text{ MHz}} & \text{if } f > 15 \text{ MHz}, \end{cases} \quad (3.15)$$

with $[f] = \text{MHz}$ as the measured frequency. Due to the passive structure of the test fixture the additional measurement uncertainty $Z_{a, \text{fixture}}$ of the impedance is less significant [Figure 3.3 (a)] than the impedance accuracy Z_a of the network analyzer [Figure 3.2 (a)].

Next, with this additional uncertainty $Z_{a, \text{fixture}}$ of the test fixture and equation 3.11 the phase uncertainty of the text fixture 16047E can be calculated. Although this phase uncertainty [Figure 3.3 (b)] is relatively small in comparison to the overall phase accuracy [Figure 3.2 (b)]. Therefore, the phase accuracy $\varphi_{z, a, \text{fixture}}$ scale is limited to a maximum of π [Figure 3.3 (b)] instead of 2π [Figure 3.2 (b)]. Furthermore, the test fixture 16047E is over a wide range of frequency and measured impedance transparent to the total phase accuracy and the uncertainty calculation could be neglected in most measurement scenarios. Note again, the calculated measurement uncertainty is only valid for the current settings. Thus, a recalculation is necessary, when a measurement setting such as frequency range is changed.

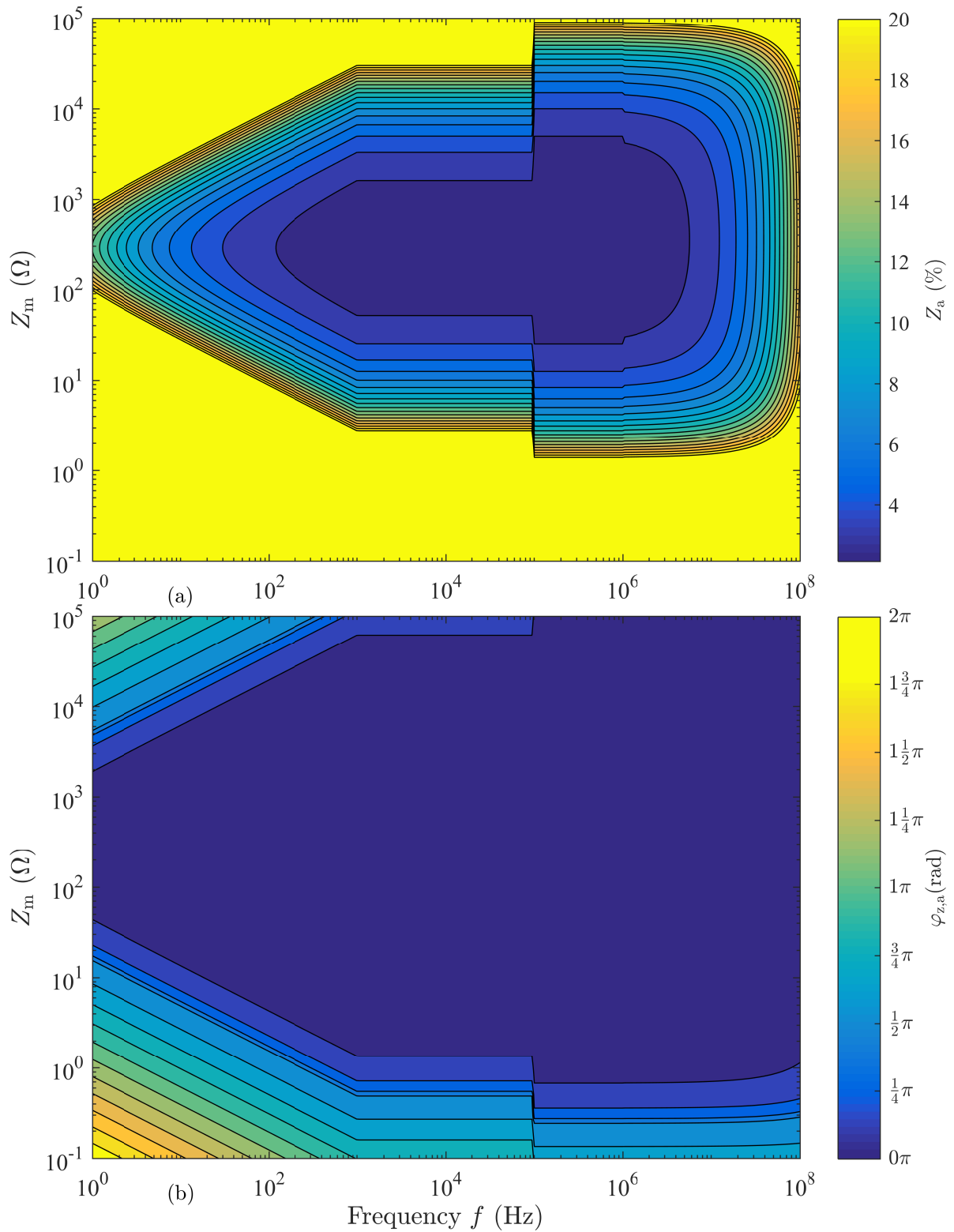


Figure 3.2: Overall calculated (Equation 3.7) impedance accuracy Z_a (a) and calculated (Equation 3.11) phase accuracy $\varphi_{z,a}$ (b) at given frequency and measured impedance Z_m of the Keysight E5061B-3L5 network analyzer itself. Note, Z_a is here manually limited to 20% (a), so it is not the maximum error meaning at any dataset beyond the 20% contour the error becomes bigger scaled in logarithmic manner.

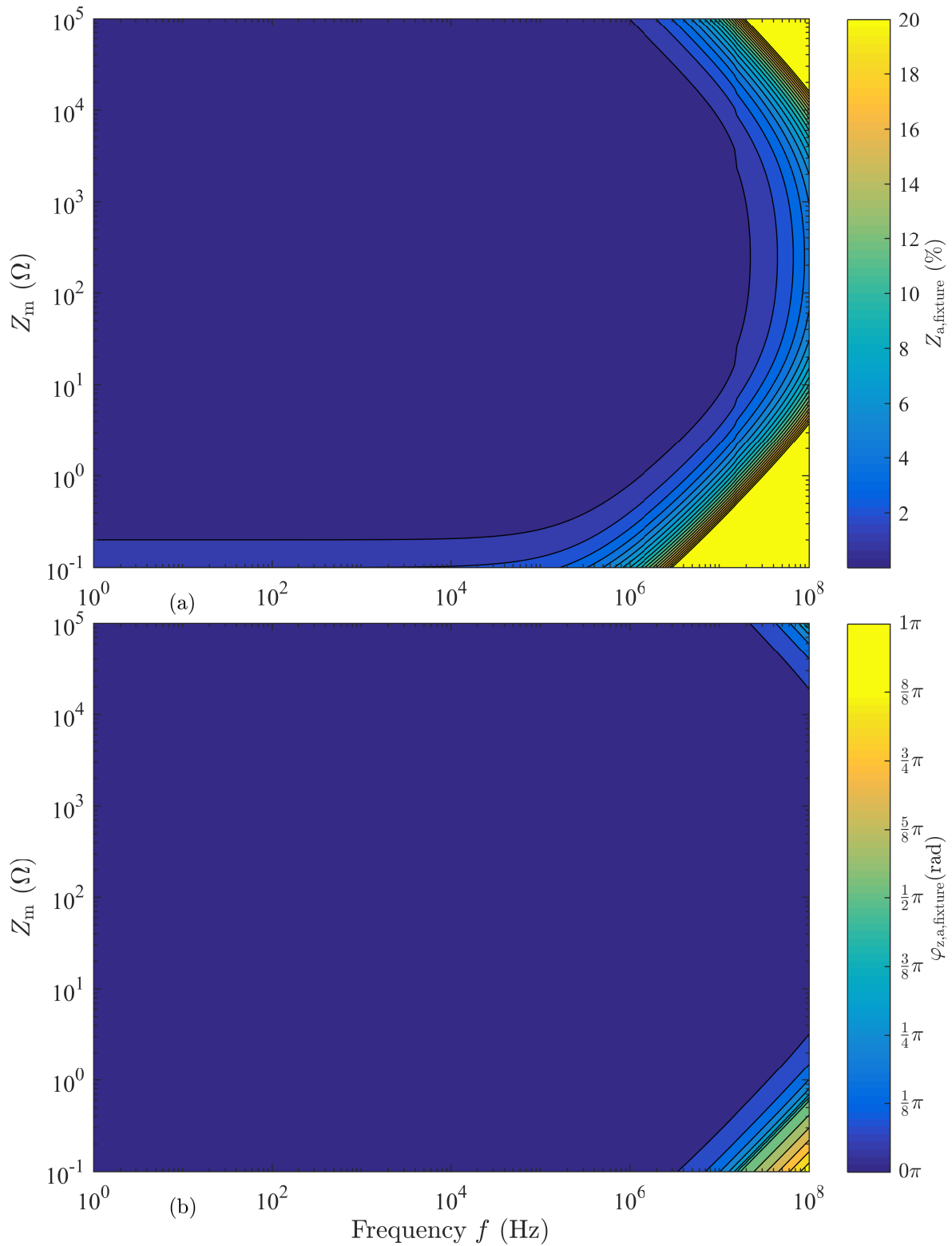


Figure 3.3: Overall calculated (Equation 3.12) additional impedance accuracy $Z_{a, \text{fixture}}$ (a) and calculated (Equation 3.11) additional phase accuracy $\varphi_{z, a, \text{fixture}}$ (b) at given frequency and measured impedance Z_m of the Keysight 16047E test fixture itself. Note, Z_a is here manually limited to 20% (a), so it is not the maximum error meaning at any dataset beyond the 20% contour the error becomes bigger scaled in logarithmic manner. Also $\varphi_{z, a, \text{fixture}}$ is manually limited to π , cause of its maximum value.

3.1.1.2 Bias-T with Protection Circuit

As described in chapter 2.2.2, capacitive ultrasonic transducers need, in addition to the AC excitation voltage, a DC bias voltage to linearize their operation around an operating point. As a rule of thumb the DC bias voltage is thereby often chosen at 80% of the pull-in voltage. A circuit called Bias-T [Figure 3.4 (a)] is used to superimpose a small AC excitation voltage and an often higher DC voltage. Hereby a high voltage capacitor C_1 is used to block the DC voltage going in to the output stage of a signal generator delivering the AC voltage. However, the AC signal can pass the capacitor C_1 , because of $x_{C_1} = \frac{1}{j\omega C_1}$, with $\omega = 2\pi f$, and the resistor R_1 protects the DC source, using simply a voltage divider [Figure 3.4 (a)]. Thus the DUT is provided with AC+DC signal. Furthermore, a good construed combination of C_1, R_1 can improve the electrical impedance matching to a DUT. Note, when larger AC signal level is needed, then the output stage of the DC power supply must also be protected by using an inductor L_1 instead of a resistor R_1 [Figure 3.4 (b)]. Then the inductor blocks the AC signal, due to its increasing resistance $x_L = j\omega L$ with $\omega = 2\pi f$.

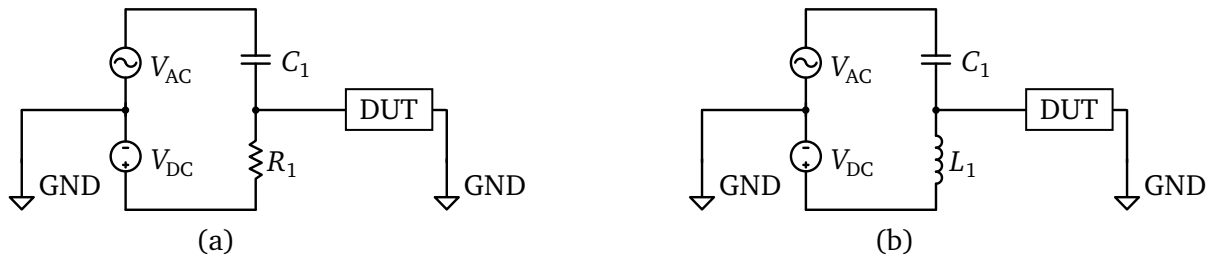


Figure 3.4: Bias-T schematic for small AC signal level and DC coupling into a DUT (a) and Bias-T schematic for larger AC signal level and DC coupling into a DUT (b).

The network analyzer E5061B-3L5 can only handle 42V at 1 M Ω or 7V at 50 Ω input impedance at maximum for T and R [60]. Thus, it must be protected when using higher DC voltages. A Bias-T circuit with protection diodes was designed. It features in addition to the coupling capacitor C_1 two transient voltage suppressor diodes (TVSDs) P6KE6.8CA ST[®] (STMicroelectronics, Geneva, Switzerland) D_1 and D_2 (Figure 3.5), which have a breakdown voltage of 6.8V nominal each [63]. Below this voltage these diodes are suspending any significant current flow. However, they are rated with a leakage current of maximum 1 mA at 5.8V stand-of-voltage [63]. Beyond 6.8V nominal they become conductive and discharge the current of the high DC voltage against ground (GND). As mentioned before two of these TVSDs are being used to protect the network analyzer E5061B-3L5. Diode D_1 protects the output of the E5061B-3L5 (LF_{OUT}) and input R . The diode D_2 protects input T and is connected after the DUT in case of a short cut failure of the DUT. In doing so, all three connections to the network analyzer E5061B-3L5 are protected against voltages above 6.8V nominal. Its design fits directly at the connectors LF_{OUT} , R , T of the network analyzer E5061B-3L5 [Figure 3.5 (a)].

In addition the circuit features four jumpers JP_{1-4} to deliver a better matching option for the electrical impedance of the DUT. They set four fixed high voltage SMD HVC2512 (Welwyn Components, TT Electronics, Woking, UK) resistors R_{1-4} [Figure 3.5 (b)], soldered to the bottom side, ranging from

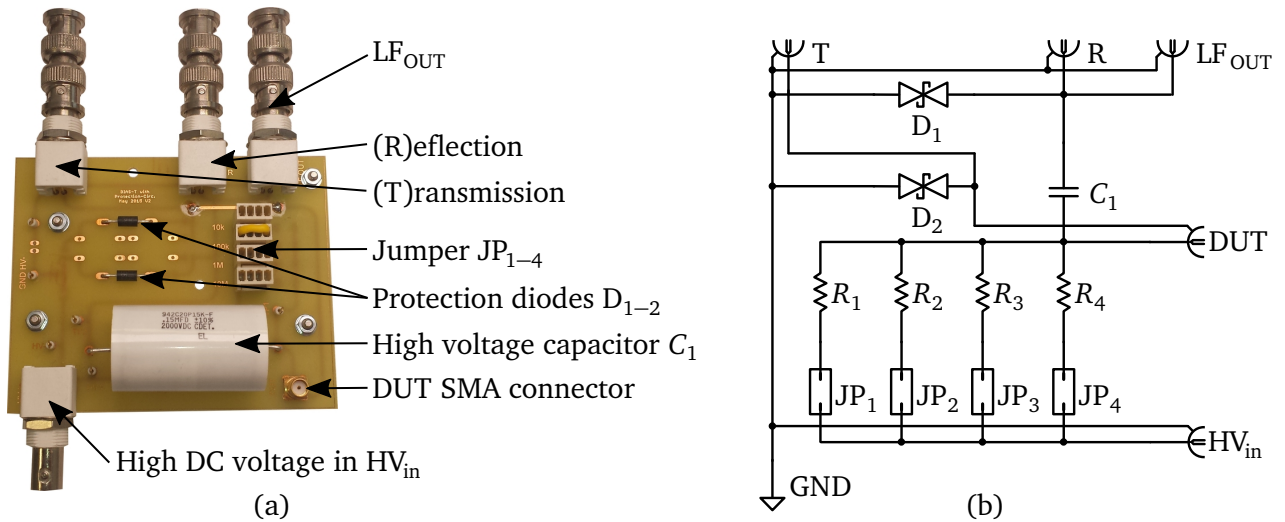


Figure 3.5: Bias-T circuit for AC and DC (up to 2.0 kVDC) coupling extended with protection diodes for usage with the Keysight impedance analyzer E6051B including interchangeable resistors, via jumpers, for better DUT matching (a) its design fits directly to the connectors of the Keysight Network Analyzer E5061B-3L5 and the schematic of the Bias-T with two bipolar protection diodes D_1 , D_2 P6KE6.8CA ST[®] (STMicroelectronics, Geneva, Switzerland) (b). The jumpers JP_{1-4} feature a better DUT electrical impedance matching by choosing a resistor R_{1-4} .

$R_1 = 10\text{ k}\Omega$, $R_2 = 100\text{ k}\Omega$, $1\text{ M}\Omega$ to $10\text{ M}\Omega$. They have power rating of 1 W at 70°C and a limiting element voltage of 3 kV [64], which is ideal for a high DC voltage Bias-T. Note that the $10\text{ k}\Omega$ resistor is not soldered yet, due to shortness of supplies when buying only a few. Also the capacitor C_1 must be suitable for high DC voltages. Here a polypropylene capacitor (942C20P15K-F, Cornell Dubilier Electronics, Inc., Liberty, SC, USA) was used to block the DC voltage. It has a voltage rating up to $2000\text{ V}_{\text{DC}}$ and 500 V_{AC} [65]. So it can be used for a combined AC+DC signal without being damaged.

To test this circuit a high voltage DC power supply PS310 (SRS, Stanford Research System, Sunnyvale, CA, USA) is used to provide DC voltages up to 1250 V [66]. It is connected to the HV_{in} input via BNC [Figure 3.5 (a)]. The jumper JP_2 was bridged so that $R_2 = 100\text{ k}\Omega$ was chosen. Next an oscilloscope RTB2004 (Rohde & Schwarz GmbH & Co. KG, Munich, Germany) was connected via a 100:1 probe TT-HV-250 (TESTEC Electronic GmbH, Frankfurt, Germany) to measure the high DC voltage directly at channel one. This channel also was used to trigger the signal. Then channel two, three and four were connected to the LF_{OUT} , R respectively T of the Bias-T with its protection circuit. Within these test conditions several scenarios were tested.

First, a dummy DUT with an electrical impedance of $50\ \Omega$ was connected to the circuit and 250 V was set to the PS310. Its current limit was set to the maximum of 20 mA [66] to avoid any restrictions. The power supply then was switched on and off several times and the voltage was recorded over time [Figure 3.6 (a)]. Because a DC voltage has many higher frequency components at its switching moments the capacitor C_1 cannot block them. As expected the TVSD D_1 cuts off the voltage levels according to their specification at around 6 V [Figure 3.6 (a)]. After DC voltage is established the capacitor C_1 blocks the it totally. Hence, the voltage levels become zero again. Therefore later the connected

network analyzer would be protected at its output and inputs [60]. The discontinuity at each rising slope of LF_{OUT} , R can not be explained in the moment. It could be perhaps the current limitation of the PS310 power supply, which occurs during the first milliseconds of charging the capacitor C_1 in combination with R_2 . The voltage drop at T is negligible small due to the $50\ \Omega$ of the dummy DUT.

Second, to test TVSD D_2 here the test conditions were changed to a DUT with a short cut, pretending a failure such as a break down which could happen during a normal impedance measurement. Again 250V were applied to the HV_{in} and the voltages were recorded [Figure 3.6 (b)] with the oscilloscope RTB2004 using the same configuration as before.

The TVSD D_1 does cut off the voltage level this time around 4V at connector LF_{OUT} , R . The voltage level at T is cut off stable at 7V by TVSD D_2 . Due to the short cut at the DUT the voltage level at D_2 stays at this maximum level of the TVSD. In doing so, the network analyzer also is protected in case of a short cut failure of the DUT.

Third, the voltage level was recorded when the applied 250V DC voltage was switched off. Again as expected the TVSDs do cut off the voltage at their ratings. The network analyzer is protected in all cases. However, an impedance measurement should only be conducted when the DC voltage is settled to its target value. Here enough time should be considered depending on given time constants of the combination of DUT and R_x and C_1 of the Bias-T.

Next, a comparison measurement was performed between the original 16047E test fixture and the Bias-T with protection circuit, to obtain the influence. Although a Bias-T is originally used to provide a AC+DC voltage for capacitive DUTs, the comparison is done with a piezoelectric DUT. Because measuring a capacitive DUT with a DC voltage leads often to weak performance and a piezoelectric DUT does not change its behavior when zero DC voltage is applied. Therefore the electrical impedance Z and the phase φ of a Murata MA40B8S was measured directly at the 16047E test fixture and at the Bias-T [Figure 3.7 (a), (b)]. The applied DC voltage was set to 0V to see the influence of the Bias-T with protection circuit. Overall, both measured impedance and phase curves are in good alignment of each other [Figure 3.7 (a), (b)], which is indicated by the median error $Z_{med} = 1.82\%$ and $\varphi_{med} = 0.063\%$. Furthermore a wide range of the Bias-T measurement is within the accuracy of the Keysight E5061B-3L5 and therefore the measurements are within specifications. However, the maximum error of the impedance $Z = 28\%$ and its mean error is $Z_{mean} = 2.7\%$ and also the maximum error of the phase $\varphi = 7.04\%$ and its mean error $\varphi_{mean} = 0.37\%$ showing that the Bias-T is not totally transparent for these measurements [Figure 3.7 (c), (d)]. In particular sharp shapes such as changing slope of the curves e.g. peaks in impedance [Figure 3.8 (a) I, II, III] and peaks in phase [Figure 3.8 (b) IV, V] are to be considered with more uncertainty. Considering these facts the Bias-T with the protection circuit can be used for DUT measurements.

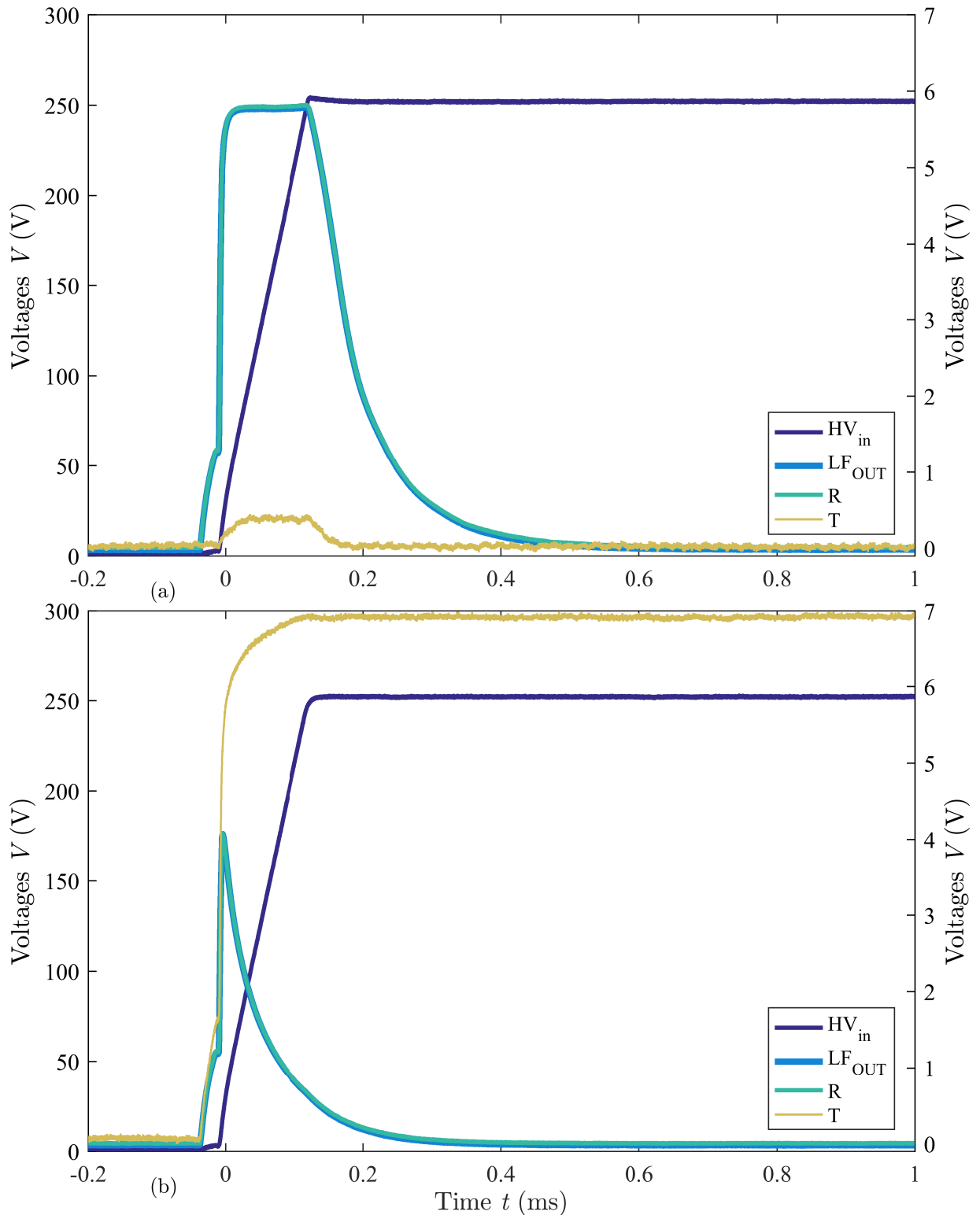


Figure 3.6: Measured voltage levels at the connectors LF_{OUT} , R and T (right axis), when 250V is applied the HV_{in} (left axis). A dummy DUT with 50Ω is connected (a). The protection diode D_1 does cut off the voltage level to maximum around 6V at connector LF_{OUT} , R . The voltage level at T is also negligible small (a). A dummy DUT with short cut is connected (b). The protection diode D_1 does cut off the voltage level around 4V at connector LF_{OUT} and R . The voltage level at T is cut off stable at 7V, due to D_2 .

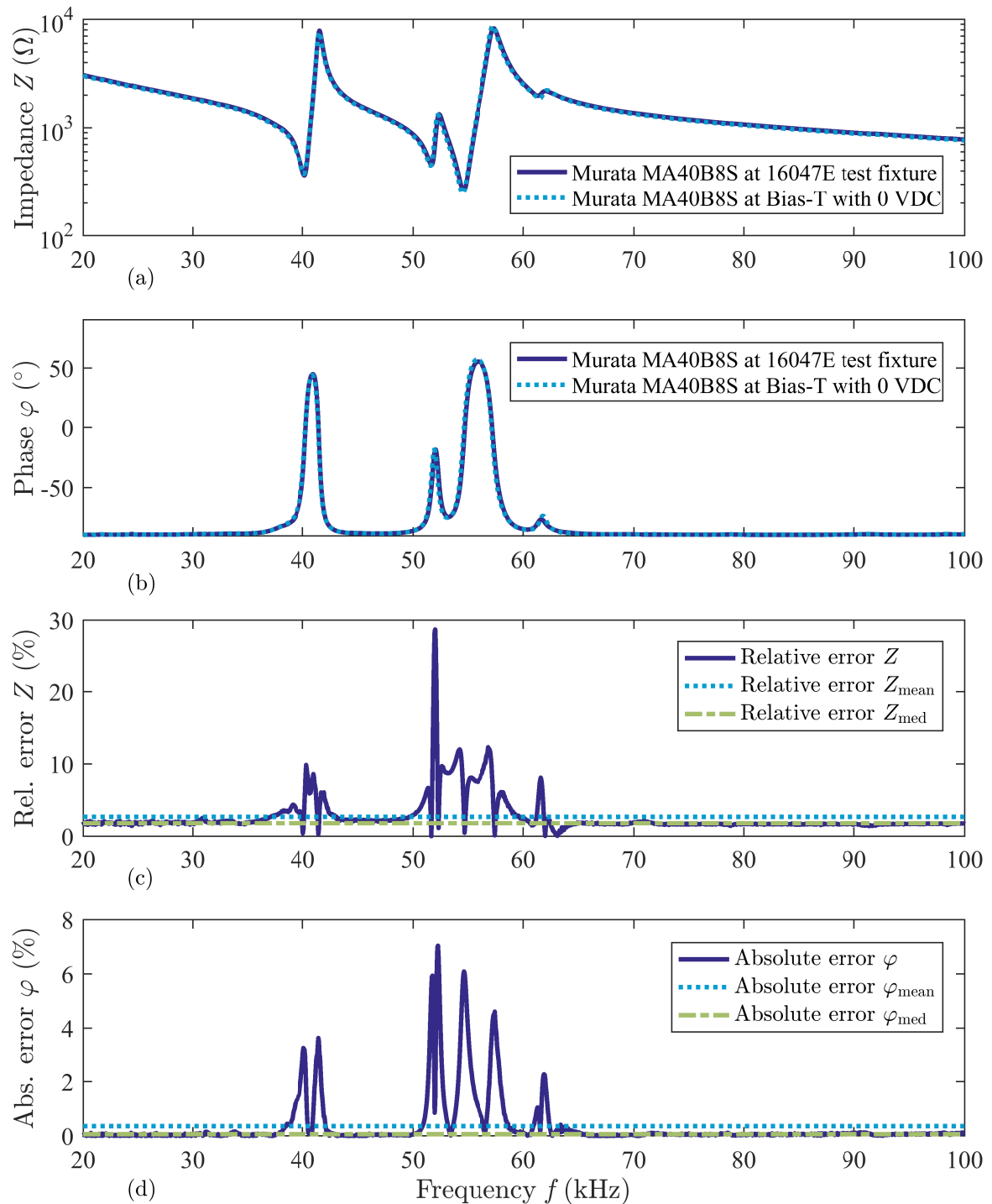


Figure 3.7: Comparison between a Murata MA40B8S ultrasonic transducer measured at the original 16047E test fixture and measured at the Bias-T with protection circuit for impedance (a), phase (b) and the introduced relative error of the Bias-T with protection circuit for impedance (c) and the absolute phase error with reference to maximum 180° (d).

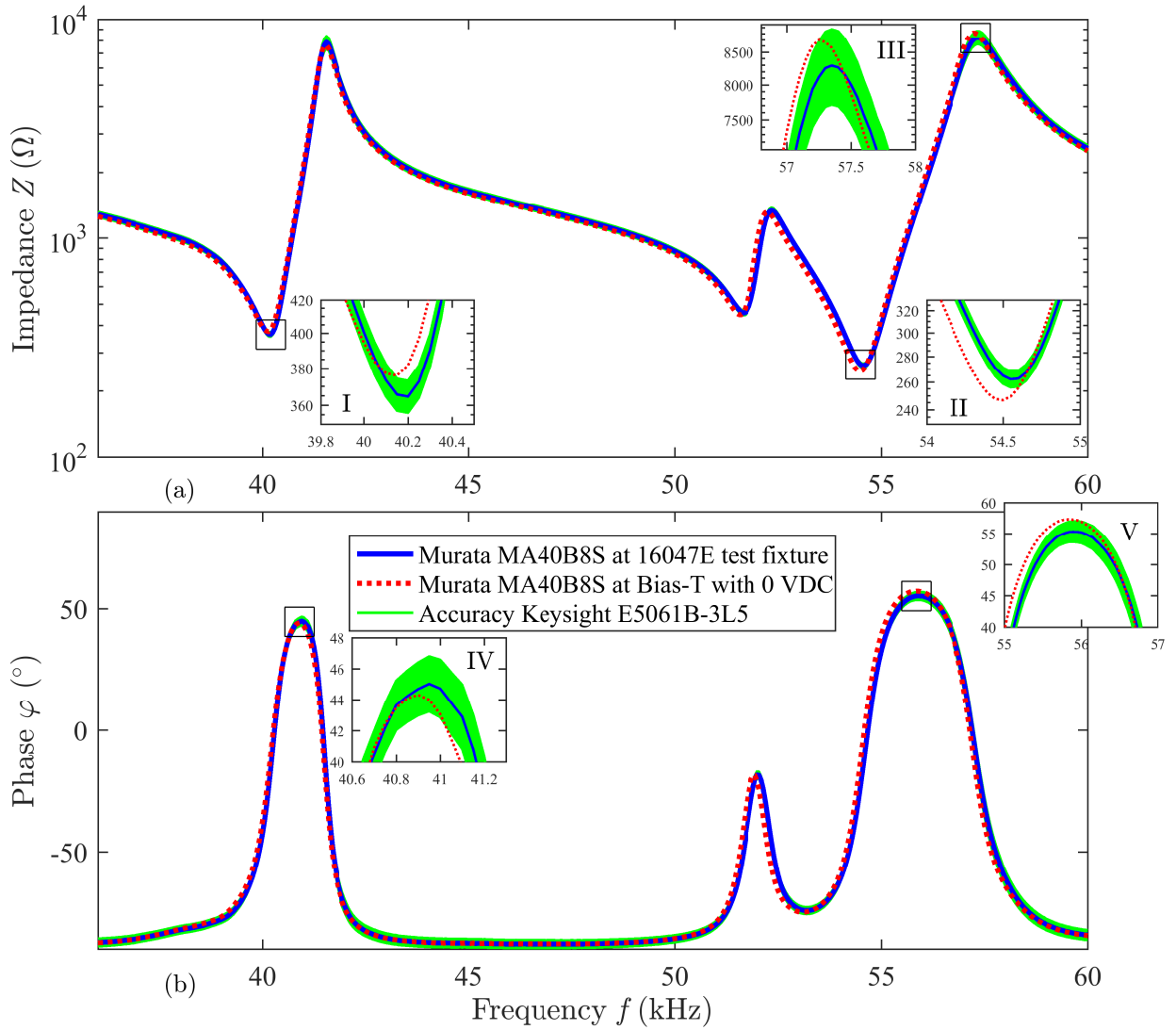


Figure 3.8: Detail view of measurements [Figurere 3.7 (a), (b)] including calculated (Equation 3.7) impedance accuracy Z_a (a) and calculated (Equation 3.11) phase accuracy $\varphi_{z,a}$ (b). Inlets I, II, and III are showing close ups of the impedance values and IV and V of the phase values.

3.1.2 Impedance Measurement Setup for Higher Excitation Voltage

The electrical impedance measurement of DUT is conducted with a dedicated impedance analyzer or a network analyzers with impedance measurement option built in (Chapter 3.1.1). Those measurement devices are being used to perform a small signal analysis. Therefore, they have a built in small AC signal source of a few volts only. Keysight network analyzer delivers only $2V_{pp}$ at 50Ω (Chapter 3.1.1) [60]. In this chapter a measurement setup is described to measure the electrical impedance at higher AC excitation voltages. Using a waveform generator, an amplifier and an oscilloscope the characterization of DUTs up to $70V_{AC}$ are performed. In doing so, often disregarded, for example the frequency dependency on higher excitation voltage $f(V_{AC})$, meaning regular driving voltage, is investigated which can lead into nonlinearities in its performance e.g. bifurcation.

A waveform generator Keysight 33522B-OCX (KEYSIGHT TECHNOLOGIES, Santa Rosa, CA, USA) with a high-stability Oven Controlled Crystal Oscillator (OCXO) timebase is used to generate a sinusoidal AC voltage. So its frequency accuracy of $\pm(0.1 \text{ ppm of setting} + 15 \text{ pHz})$ is $\pm(2 - 5) \text{ mHz} + 15 \text{ pHz}$, which refers to $(20 - 500) \text{ kHz}$ ultrasonic frequency range can be neglected [67]. Its output voltage can be set up to maximum $20V_{pp}$ when the output impedance is set to *high Z* [67], meaning feeding into open circuit. If even higher voltage amplitudes are needed an audio amplifier Dynacord SL2400 (Dynacord GmbH (Bosch), Straubing, Bavaria, Germany) is then connected to the output of the waveform generator (Figure 3.9). It is a Class H amplifier and according to its specification it can be used up to $40 \text{ kHz} \pm 1 \text{ dB}$ (Table 3.1) [68]. Using a class H amplifier, which is a cascaded AB amplifier[68], gives at least the possibility to drive a capacitive load unlike modern high end class D amplifiers. Next, the generated and amplified sinusoidal signal then drives the DUT with a voltage divider in place.

Table 3.1: Main specification of the audio amplifier Dynacord SL2400 [68].

Properties	Values	Units	Annotations
Frequency response	0.01 – 40	kHz	$\pm 1 \text{ dB}$ ref. 1 kHz
Maximum voltage swing	65.1	V_{RMS}	1% THD, 1 kHz
Voltage gain	32	dB	Ref. 1 kHz
Maximum input level	+21	dBV	
Maximum input level	8.69	V_{RMS}	
Slew rate	26	$\frac{V}{\mu\text{s}}$	
Maximum output power	420	W	CW 1 kHz
Output stage topology			Class H

To calculate the electrical impedance Z_{DUT} with equation 3.5, the voltage over the DUT and the current through the DUT have to be measured. Therefore, an oscilloscope Keysight DSO-X 2002A (KEYSIGHT TECHNOLOGIES, Santa Rosa, CA, USA) with 70 MHz analog bandwidth is used. The entire voltage V of the circuit is measured at channel one. When the amplifier is used, the higher voltage is measured with a N2862B 150 MHz 10:1 passive probe (KEYSIGHT TECHNOLOGIES, Santa Rosa, CA, USA). Thereby voltages up to $300V_{\text{RMS}}$ could be measured without damaging the oscilloscope [69, 70]. The voltage V_s over a shunt resistor R_s is at channel two. Later it is used to calculate the current I_{DUT} through the DUT (Equation 3.17). In doing so the phase can be measured with the oscilloscope directly.

Both devices are remotely controlled via PC using LabVIEW™ (National Instruments, Austin, TX, USA). LabVIEW™ is sweeping through the specified frequency in equidistant steps. At each step the voltage V , voltage V_s and phase shift φ_{V-V_s} between both voltages are measured. The correct voltage V_{DUT} over the DUT needs to be calculated with

$$V_{\text{DUT}} = V - V_s. \quad (3.16)$$

The current I_{DUT} through the DUT is calculated by

$$I_{\text{DUT}} = \frac{V_s}{R_s}. \quad (3.17)$$

Combining equation 3.16 and 3.17 in equation 3.5 finally the electrical impedance Z_{DUT} is calculated with

$$Z_{DUT} = \left(\frac{V}{V_s} - 1 \right) R_s. \quad (3.18)$$

In the end, the frequency f , calculated electrical impedance Z_{DUT} , measured phase shift φ_{V-V_s} and both measured voltages V , V_s are stored in a text file for further post processing and evaluation in MATLAB R2016b (The MathWorks[®], Natick, MA, USA).

Beforehand R_s value was chosen not to small, because the voltage drop V_s would be to small too and so difficult to measure with an oscilloscope. If R_s value is chosen too big it would have to much influence on the DUT. The measured electrical impedance Z_{DUT} would be distorted. Considering these cases it is always a trade of between enough SNR and less distortion of the electrical impedance. Knowing this fact R_s is chosen to $6.8 \Omega \pm 1\%$ from the E-24 row when higher voltages of $(15 - 70)V_{pp}$ are needed. It was also measured with a high precision $7\frac{1}{2}$ digit digital multimeter DMM 7510 (Tektronix, Beaverton, OR, USA). Its actual value at ambient temperature of 20°C and in consideration of the accuracy of the DMM 7510 [71] is so determined to $R_s = 6.5072 \Omega \pm 245.3 \mu\Omega$ using averaging of 10,000 times.

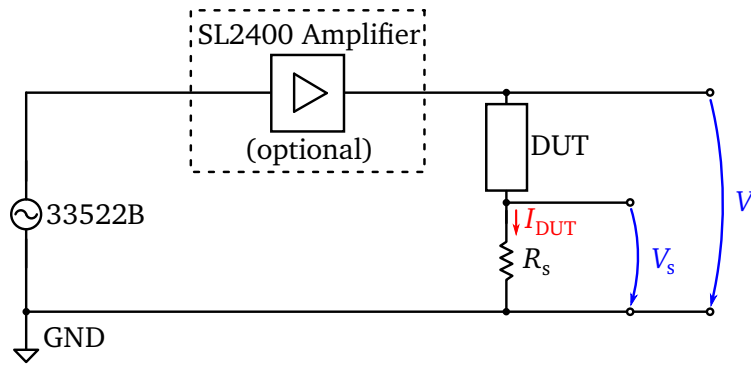


Figure 3.9: Schematic for electrical impedance measurements at higher AC voltages. If the SL2400 amplifier is used then the entire voltage V must be measured with at least a 10:1 probe.

The accuracy of these simple electrical voltage divider (Figure 3.9) impedance measurement was checked with a comparison measurement of a Bolt-Clamped-Langevin Transducer (BLT) using the Keysight network analyzer E5061B-3L5 and the voltage divider circuit (Figure 3.10). The accuracy V_{error} of the Keysight DSO-X 2002A is given by [69]

$$V_{error} = \pm (\text{DC vertical gain accuracy} + \text{DC vertical offset accuracy} + 0.25\% \text{ full scale}), \quad (3.19)$$

with [69]

$$\text{DC vertical gain accuracy} = \pm \begin{cases} 3\% \text{ full scale} & \text{if } \geq 10 \text{ mV/Div} + 0.25\% \text{ full scale} \\ 4\% \text{ full scale} & \text{if } < 10 \text{ mV/Div} + 0.25\% \text{ full scale} \\ 4\% 32\text{mV} & \text{if } \leq 2 \text{ mV/Div} + 0.25\% 32 \text{ mV.} \end{cases} \quad (3.20)$$

and with the offset accuracy [69]

$$\text{DC vertical offset accuracy} = \pm 0.1\text{Div} \pm 2 \text{ mV} \pm 1\% \text{ of offset setting.} \quad (3.21)$$

The delta time (using cursors) uncertainty, which leads in the end to φ_{error} , is given by [69]

$$\Delta t_{\text{error}} = \pm (\text{time base accuracy reading}) \pm (0.0016\text{screen width}) \pm 100 \text{ ps} \quad (3.22)$$

where the time base accuracy is calculated with [69]

$$\text{time base accuracy} = +25 \text{ ppm} \pm 5 \text{ ppm (per year aging)}. \quad (3.23)$$

Since the comparison measurement has to be conducted with the same excitation voltage level of $2V_{\text{pp}}$ as with the network analyzer E5061B-3L5 [60] a larger value of $R_s = 22.114 \Omega \pm 997 \mu\Omega$ [71] was chosen. This is necessary to be able to measure the small voltage levels due to the small current through the shunt resistor. Assuming a uniform distribution of the given uncertainties according to the data sheet the entire uncertainty is then using equation 3.19, 3.20, and 3.21 calculated for the magnitude of the impedance by

$$Z_{\text{error}} = \sqrt{\left(\frac{1}{V_s} R_s \frac{V_{\text{error}}}{\sqrt{3}}\right)^2 + \left(-\frac{V}{V_s^2} R_s \frac{V_{\text{error}}}{\sqrt{3}}\right)^2 + \left[\left(\frac{V}{V_s} - 1\right) R_{s,\text{error}}\right]^2} \quad (3.24)$$

using the Guide to the Expression of Uncertainty in Measurement (GUM) [72]. Next the phase uncertainty is then calculated with equation 3.22 and 3.23 by

$$\varphi_{\text{error}} = \sqrt{\left(360f \frac{\Delta t_{\text{error}}}{\sqrt{3}}\right)^2} = 360f \frac{t_{\text{error}}}{\sqrt{3}} \quad (3.25)$$

again assuming the uniform distribution and using the GUM [72].

As a first result both measured curves are in good agreement over a wide range (Figure 3.10). However, at a closer look the uncertainties of the measured curves are not fully covered against each other [Figure 3.10 inlet I and II]. Furthermore, at the range around the anti resonance frequency is covered by a huge measurement uncertainty, due to the small signal levels [69]. As conclusion impedance measurements with a voltage divider can only be seen as a relative measurement between themselves. Absolute values, especially in the range of higher impedance, has to be considered with care of the uncertainty (Figure 3.10).

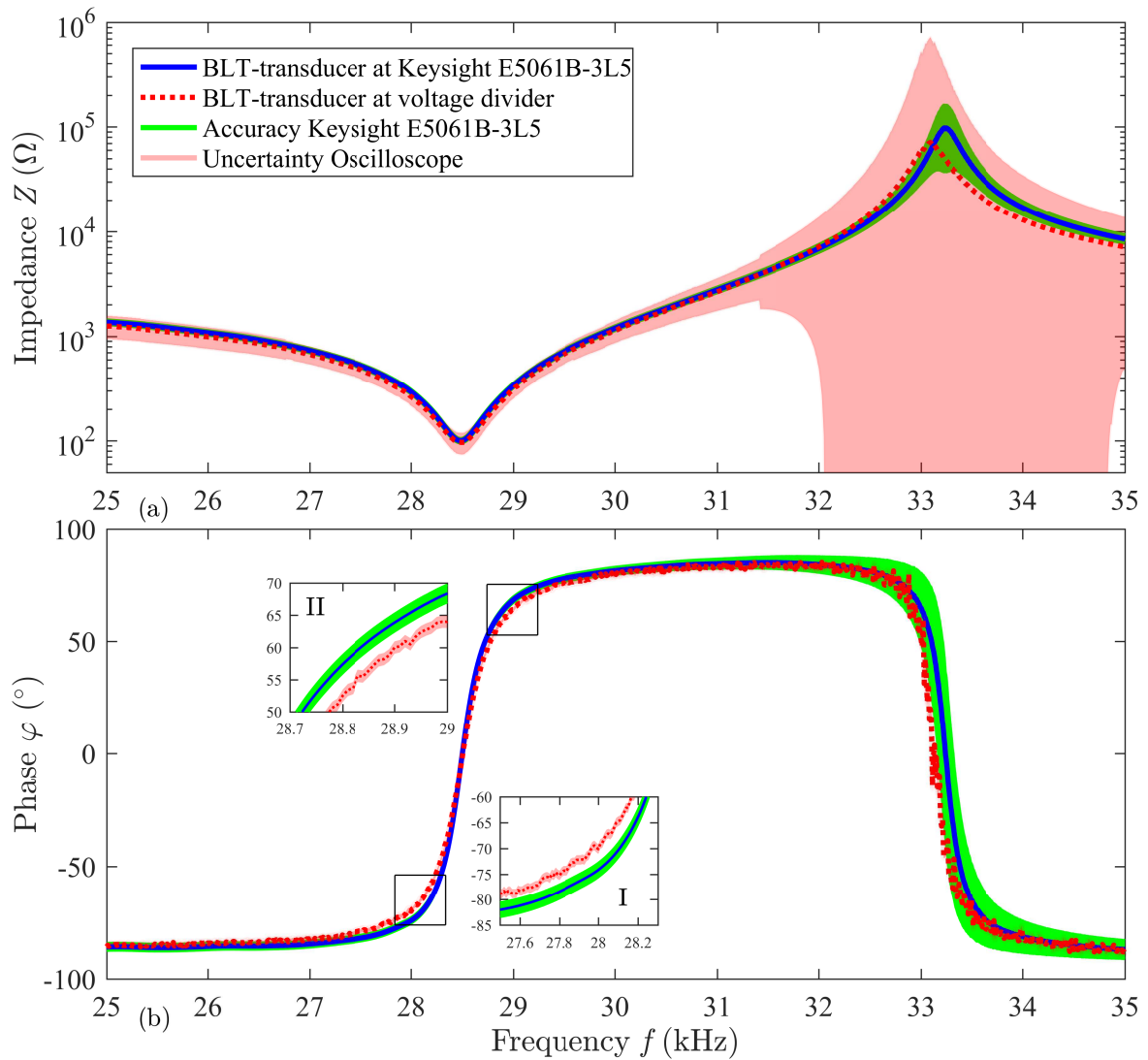


Figure 3.10: Comparison measurement of a BLT measured with E5061B-3L5 network analyzer at $2V_{pp}$ and with the voltage divider circuit (Figure 3.9) with waveform generator using $2V_{pp}$ too and oscilloscope for data acquisition.

3.1.3 Ambient Temperature Impedance Measurements

Using a network analyzer such as the Keysight E5061B-3L5 can be a fast and accurate way to measure the electrical impedance and phase of a DUT (Chapter 3.1.1). It is ideal to do these measurements at ambient/room temperature at 20°C or slightly elevated up to 40°C or lowered down to 5°C , because no special cables or adapters for harsh environment are needed [60]. Furthermore, characterization of typical ultrasonic transducers such as piezoelectric or electromagnetic ones are often done at those moderate temperatures. On the one hand, there are used later in industrial application with similar conditions. On the other hand many of such ultrasonic transducers have a Curie temperature and a temperature range in which they are specified. Common piezoelectric ultrasonic transducer for example are specified in a range of -40°C to $+85^\circ\text{C}$ [29]. Same of them such as Bolt-Clamped Langevin ultrasonic are even only tested at $(23 \pm 3)^\circ\text{C}$ [18]. However, some industrial application, in which certain ultrasonic transducer are used, have to withstand harsher environment conditions. Reaching from cryo temperatures of liquid

nitrogen below -190°C (Chapter 3.1.5) up to higher temperatures beyond $+300^{\circ}\text{C}$ (Chapter 3.1.4). In reason of that, two different setup scenarios were built.

3.1.4 High Temperature Impedance Setup

For high temperature measurements two completely different setups were built. The first one is simply an industrial oven ULA 400 (Mettler GmbH + Co.KG, Schwabach, Bavaria, Germany) reaching up to 220°C [73]. It is controlled by a standard PID controller by manual setting a target temperature value with a dial. Knowing this fact the target temperature can be reached with an overshoot of 30% [74]. This oven covers a volume of $(40 \times 40 \times 33)\text{cm}^3$ and uses a fan for a homogeneous temperature distribution. Using this oven for impedance measurements, the entire DUT can be placed inside the oven, which minimizes any temperature gradient along the DUT. The connection cables are loosely laid through the gasket of the front door. Here special cable with polytetrafluoroethylene (PTFE, Teflon) isolation enable measurements up to approximately 260°C [75].

The second setup is a special designed high temperature setup (HTS) done during its authors Diploma thesis. It is a precise controlled oven. The adaptive PID controller allows different temperature gradients from 1 K/min up to 30 K/min, but most important, it minimizes any significant overshoots. During long term measurements at 1000°C , the system was able to reach the target temperature with a overshoot of 0.08 K only [76]. Since, the inner volume is only $(169 \pm 8.48)\text{cm}^3$ [76], larger DUTs, which are then feed through an opening in the lid, are exposed to a temperature gradient from inside to outside of the oven along the DUTs.

So both high temperature setups are useful for DUTs characterizations under temperature loads. In doing so, they can either be used with the network analyzer E5061B-3L5 (Chapter 3.1.1) or with the voltage divider circuit using waveform generator and oscilloscope (Chapter 3.1.2).

3.1.5 Cryo Temperature Impedance Setup

To reach lower temperatures below ambient a non-controlled passive cryo setup was built using two styrofoam containers with dimensions of $(48 \times 48 \times 38)\text{cm}^3$ with a wall thickness of 4 cm and $(39.5 \times 33.5 \times 36.5)\text{cm}^3$ and 3.5 cm thick. Thereby the smaller container is nested in the bigger one [Figure 3.11 (a)], which gives a total thermal insulation layer of 7.5 cm of styrofoam. Next, DUTs mounted in holders equipped with a thermo couple at bottom and top were placed in each corner [Figure 3.11 (a)].

In doing so the thermo couples monitoring the temperature gradient along the DUTs. Between them two aluminum foil pans were placed and later filled carefully with liquid nitrogen. On top of the inner styrofoam container, which was cut in height, a metal grid is then placed with further six aluminum foil pans [Figure 3.11 (b)] and filled with liquid nitrogen too. They act as a cooling curtain because the cooler dry air is falling down pushing out the warm more humid air. So there is slight excess pressure which is also keeping moisture out during the measurements. After closing the outer styrofoam container with

its lid (not completely) it takes about approximately half an hour to cool it down to -190°C . Reaching this stable temperature point the characterization of the DUTs using again the voltage divider circuit with waveform generator and oscilloscope (Chapter 3.1.2) is started. Now the entire system is slowly warming up until the ambient temperature is reached again. During this process several impedance measurements are conducted. This takes several hours depending on the ambient temperature and energy which is pumped into the system through the impedance measurements of the DUTs. Especially measurements at higher excitation voltages can heat up the DUTs.

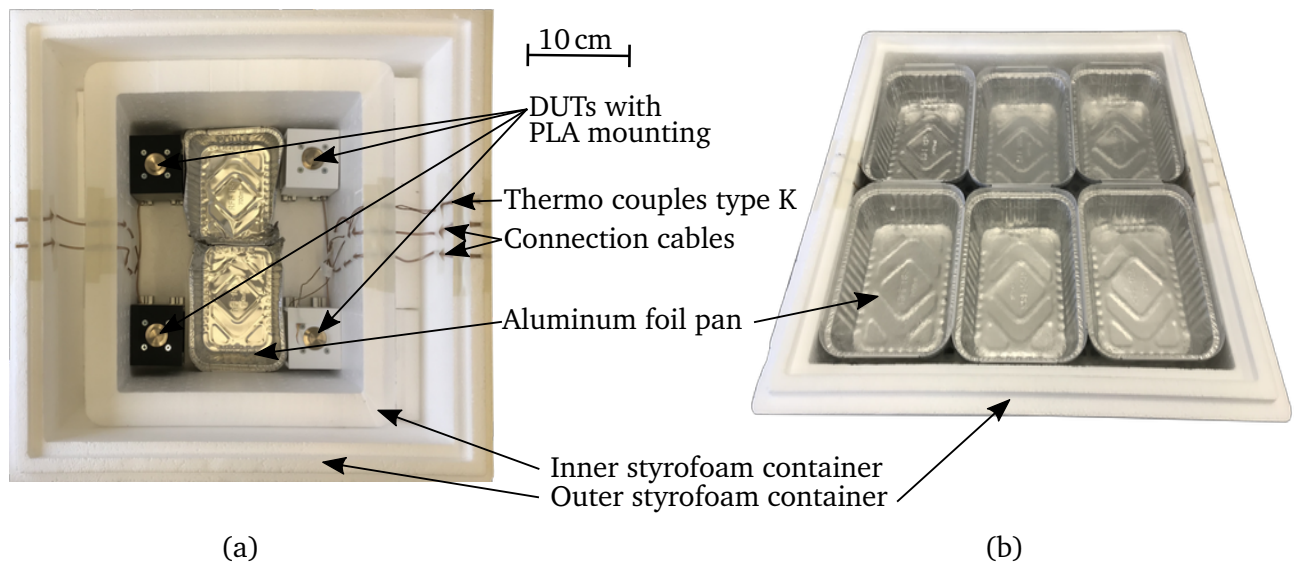


Figure 3.11: Cryo temperature measurement setup inner view with four DUTs one in each corner(a) and covered setup with aluminum foil pans to store the liquid nitrogen (b). Picture take by Steffen Elgner [35].

3.2 Surface Velocity and Displacement

Another important characterization method of ultrasonic transducers is the measurement of their surface velocity and displacement. The electrical impedance gives a quick and first indicator of the characteristic of an ultrasonic transducer e.g. resonance frequency f_r (Chapter 2.3). But it gives no information about the vibrational modes. To get most sound pressure level (3.3) it is essential to operate ultrasonic transducers in their fundamental mode. For this reason a Laser Doppler Vibrometer (LDVM) was extended with three translational linear stages to feature a scanning option in addition to its single point velocity and displacement measurement. This step was chosen, because a new scanning vibrometer costs starting at 75,000€ and can cost up to 300,000€. Furthermore the post processing is more versatile such as generating video sequences of transient events.

3.2.1 Measurement Setup

The Laser Doppler Vibrometer (LDVM) measurement setup is built on a passive damped optic table (Newport, Irvine, CA, USA) to minimize disturbances (3.12). For example someone is walking by in the laboratory or heavy vehicles are driving by outside in the streets. The main component is a single point Polytec LDVM controller OFV 3001 (Table 3.2) with a OFV 534 (Table 3.3) laser unit (Polytec GmbH, Waldbronn, Baden-Wuerttemberg, Germany). Thereby the sensor head of the OFV 534 is mounted facing down on a z-axis translational linear stage PI-M403.4 DG (Physik Instrumente (PI) GmbH & Co. KG, Karlsruhe, Baden-Wuerttemberg, Germany) with a travel of 100 mm [Figure 3.12 (b)] (Table 3.4), which is mainly used to fine adjust the necessary focal distance of 200 mm (Table 3.3) [77]. The z-axis itself is mounted on an aluminum T-slot profile (40 mm grid). This is needed to roughly adjust the position in 40 mm steps or to adjust it freely along the vertical aluminum T-slot profiles [Figure 3.12 (b)]. These rough adjustments are only needed if the size of the DUT including mounting varies more than the 100 mm travel of the translational linear stage between measurements.

To achieve the scanning option two of these PI-M403.4 DG translational linear stages are mounted on top of each other at an angle of 90° [Figure 3.12 (a)]. They are then mounted centered below the sensor head OFV 534 [Figure 3.12 (b)]. In doing so the scannable area is movable ± 50 mm in both x-direction and y-direction [Figure 3.12 (a)], resulting in a total scan area of 10 cm². Since, the focal diameter of the OFV 534 is 25 μ m at its focal distance of 200 mm, a sensible minimum scanning step size of 50 μ m is recommended by the author of this work (Table 3.3) [77]. But if needed, the area could be scanned with 200 nm step size (Table 3.4) [79]. However, bear in mind this will result in 250.001 billion measurement points.

Since the translational linear stages feature only four M4 threaded holes in a (70 × 72) mm distance grid, there are only a few possibilities to mount a DUT on the X-Y-axes. To overcome this issue a special mounting plate was designed (Figure 3.13). This plate features more versatile mounting possibilities with M3, M5, M6, and M8, which are mostly arranged in a rotational pattern rotated by 22.5°. In particular M5 threaded holes having the standard distance of a 20 mm grid aluminum T-slot profile.

Table 3.2: Main specification of the Polytec LDVM controller OFV 3001 [78].

Properties of velocity	Values	Units	Annotations
Range	1 – 1000	$\frac{\text{mm}}{\text{s}}/\text{V}$	Max. 50 kHz, max. 20 kHz @ $1 \frac{\text{mm}}{\text{s}}$ range
Full scale output	20 – 20,000	$\frac{\text{mm}}{\text{s}}$	Max. $20 V_{\text{pp}}$
Resolution	0.3 – 2	$\frac{\mu\text{m}}{\text{s}}$	$\text{SNR}_{\text{RMS}} = 0 \text{ dB}$
Maximum acceleration	150 – 200,000	g	$g = 9.81 \frac{\text{m}}{\text{s}^2}$
Accuracy	± 1	% of RMS	$T = (25 \pm 5) ^\circ\text{C}$
Accuracy	± 1.2	% of RMS	$T = (5 - 40) ^\circ\text{C}$
Max. linearity error	± 0.5	% of RMS	One particular vel. range
Max. linearity error	± 1	% of RMS	Overall
Flatness	min ± 0.1	dB	Please see manual [78]
Flatness	max ± 0.5	dB	Please see manual [78]
Time delay	23.9 – 5.2	μm	
Properties of displacement	Values	Units	Annotations
Range	0.5 – 5, 120	$\mu\text{m}/\text{V}$	
Full scale output	320 – 81,920	μm	Max. $16 V_{\text{pp}}$
Resolution	0.08 – 20	μm	
Maximum velocity	2.5 – 10	$\frac{\text{m}}{\text{s}}$	$g = 9.81 \frac{\text{m}}{\text{s}^2}$
Accuracy	± 1	% of RMS	± 1 increment
Max. linearity error	± 2	increment	$(0.5 - 8) \mu\text{m}/\text{V}$
Max. linearity error	± 1	increment	$(20 - 5, 120) \mu\text{m}/\text{V}$

Table 3.3: Main specification of Polytec laser unit with sensor head OFV 534 [77].

Properties	Values	Units	Annotations
Laser type			Helium Neon (HeNe)
Laser class	2		Eye secure
Laser power	< 1	mW	
Wavelength	633	nm	Visible
Focal length	200	mm	Minimal distance
Maximal distance			Depending on surface quality
Coherency maxima	$91 + n 204$	mm	$n = 0; 1; 2; \dots$
Depth of field	± 1	mm	@ 200 mm distance
Focal diameter	25	μm	@ 200 mm distance

Table 3.4: Main specification of PI M-403.4 DG translational linear stages [79].

Properties	Values	Units	Annotations
Travel range	100	mm	
Design resolution	0.018	μm	
Encoder steps	2000		Rotary decoder
Minimum incremental motion	0.2	μm	
Backlash	10	μm	
Unidirectional repeatability	1	μm	
Pitch	200	μrad	Typ. over 100 mm
Yaw	200	μrad	Typ. over 100 mm
Maximum load	200	N	Centered, linear stage horizontal
Velocity	2.5	$\frac{\text{mm}}{\text{s}}$	Maximum
Reference point switch repeatability	1	μm	

All three axes (x-y-z-axis) are controlled by PI C-863.11 (Physik Instrumente (PI) GmbH & Co. KG, Karlsruhe, Baden-Wuerttemberg, Germany) controller each and then daisy chained and connected via USB to a PC. In addition a joystick PI C-819.30 (Physik Instrumente (PI) GmbH & Co. KG, Karlsruhe, Baden-Wuerttemberg, Germany) is setup. Its is used for an easy an quick alignment of the DUT. In doing so, start and end points of an automatic movement pattern can be set as well later in software.

To excite the DUT a waveform generator GW Instek AFG-2225 [Good Will Instrument Co., Ltd., New Taipei City, Republic of China (RoC, Taiwan)] is used [Figure 3.12 (b)]. Its output signal is connected via BNC cable to drive the DUT and via T-piece adapter directly feed into channel one of a Keysight DSO-3024 oscilloscope (KEYSIGHT TECHNOLOGIES, Santa Rosa, CA, USA) [Figure 3.12 (b)]. So the driving signal and its voltage level drop due to the load of the DUT is monitored. If larger excitation levels beyond $20V_{pp}$ [80] are needed, the SL2400 amplifier and again a N2862B 10:1 probe can be used (Chapter 3.1.2). It is stored later in software by the control PC. Furthermore, the phase shift from the excitation signal to the measured surface velocity at channel two, introduced by the DUT, is determined. In doing so, frequency or excitation voltage level dependency are later investigated. Also the measured and calculated displacement, by OFV 3001 vibrometer controller, is measured using channel three of the oscilloscope.

A standard PC with Windows[®] 10 64 Bit Education (Microsoft Cooperation, Redmond, WA, USA) running a LabVIEW[™] (32 Bit, 2016 Fall) program performs the automatic measurements . Once this program is launched the translational linear axes (y-x-z), the waveform generator and the oscilloscope are remotely controlled through this software. All setting have to be input here. However, the OFV 3001 vibrometer controller has some issues getting detected by Windows[®] 10. So by the time this work is written the settings have to be done manually. Switching on the laser and setting both ranges of the velocity and displacement decoder (Table 3.2).

At the moment the program is capable of conducting single point (0D), linear line (1D), circular area (2D) and rectangular area (2D) measurements. The movement pattern of the axes x and y is optimized for speed and it is calculated in equidistant steps by the program. Boundary conditions such as step size and dimensions are given by the operator guided by the program. For example a circular area is

described by its center point and its radius, a rectangular area is described by two opposites corner coordinates.

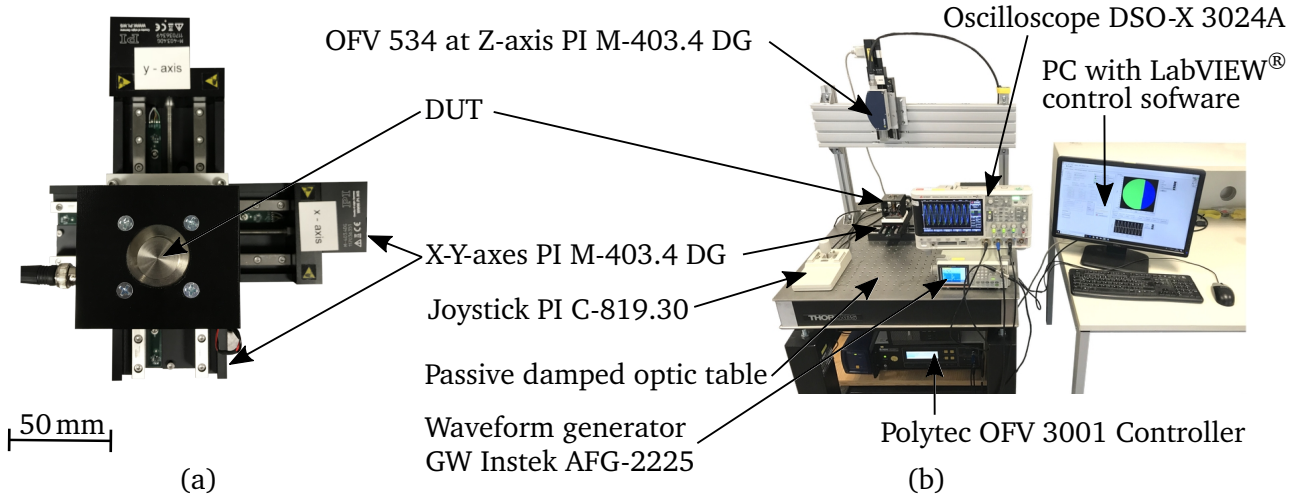


Figure 3.12: DUT holder mounted on x-y translational stages (a). Entire laser doppler vibrometer setup extended with 100 mm travel x-y-z scanning option (b). Copyright Steffen Elgner [35].

For each measurement point $[x:y:z]$ the A-scans (amplitude over time) of the excitation signal (channel one), surface velocity (channel two) and displacement (channel three) are being stored in a binary format of single precision (16Bit floating point) with little endian convention. Storing all the A-scans allows a post processing in a way that each time step of each spatial measurement point can be synchronized to obtain the transient movement by using burst signal as excitation. In doing so, a video is generated, using post processing, of the transient behavior looking at the entire measured surface. The position $[x:y:z]$ and its surface velocity, displacement, and phase measurement is stored in a text file. For reasons of reproducibility all settings for a measurement set are stored in a special setup.ini file. It can be used to read in later and repeat this particular measurement with exactly the same settings.

3.2.2 Surface Velocity and Displacement Measurement

Since, the OFV 3001 vibrometer controller is equipped with a velocity decoder OVD-01 and a displacement decoder OVD-20 the operator has to make a choice which to use for a reliable measurement. In particular when harmonic vibration signals are measured, these provide the same information in both velocity and displacement. When a given harmonic displacement $x(t)$ with

$$x(t) = \hat{x} \sin(\omega t), \quad (3.26)$$

is measured with \hat{x} as the amplitude of displacement and angular frequency ω then the velocity $v(t)$ is calculated by

$$v(t) = \frac{dx(t)}{dt} = \frac{d[\hat{x} \sin(\omega t)]}{dt} = \hat{x} \omega \cos(\omega t). \quad (3.27)$$

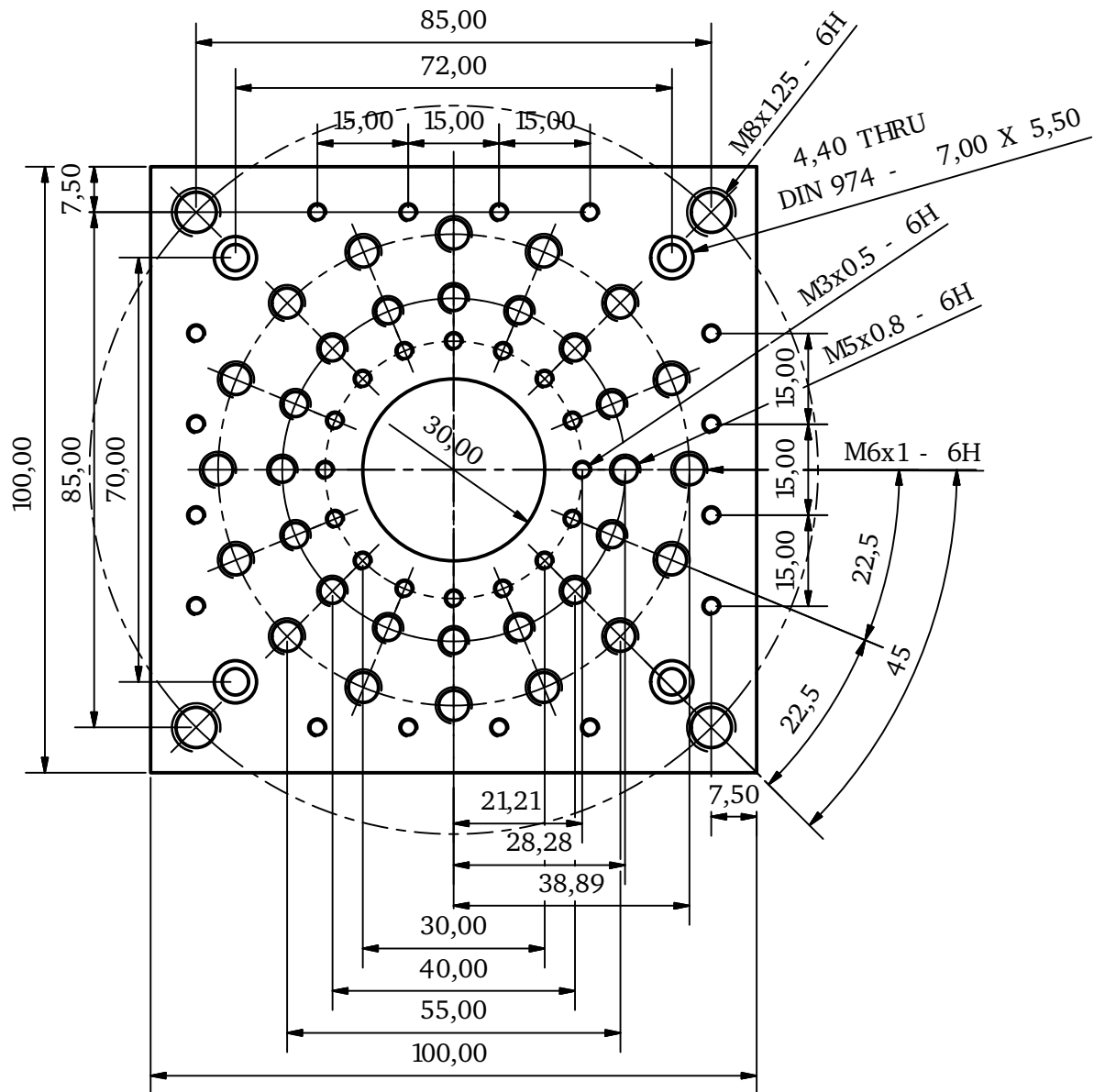


Figure 3.13: Special designed versatile mounting plate for DUTs with M3, M5, M6, and M8 threaded holes, especially M5 threads that feature a standard mounting distance of 20 mm of a aluminum T-slot profiles.

Assuming $t = 0$ and with $\omega = 2\pi f$ then the amplitude of the velocity \hat{v} is given by [78]

$$\hat{v} = 2\pi f \hat{x}. \quad (3.28)$$

The signals are shifted by 90° only, because of the derivative of a harmonic sine which is cosine.

Transient movements can be measured more clearly using the displacement information [78] by experience. Due to the design configuration of the displacement decoder it has a dynamic range of $DR = 66 \text{ dB}$ [78], which is in most cases enough, the measurements are not affected by the background noise, since the resolution is higher [78]. In contrast, the resolution of the velocity decoder OVD-01 is

limited only by the background noise ($0.2 \frac{\mu\text{m}}{\text{s}}/\sqrt{\text{Hz}}$) and becomes better the higher the frequency [78]. Using good reflecting films, e.g., leads to 50 times higher dynamic range of $\text{DR} = 100 \text{ dB}$ [78].

Assuming a surface velocity and displacement are always superimposed by background noise with lower frequency but therefore higher vibration amplitudes e.g. walking by. Using equation 3.28 for the same displacement amplitude the measured velocity would be larger by factor $2\pi f$. For example a 40 kHz Murata MA40S4S ultrasonic transducer with a displacement of $\hat{x} = 1 \mu\text{m}$ would have a surface velocity of $\hat{v} = 251.3 \frac{\text{mm}}{\text{s}}$. Compared to background noise of typically frequency below $f < 100 \text{ Hz}$ and displacements up to $\hat{x} = 10 \mu\text{m}$, would result in a 40 times smaller noise velocity of $\hat{v}_n = 6.28 \frac{\text{mm}}{\text{s}}$. Thus the SNR of the velocity is higher per definition than the SNR of the displacement. Hence, all measurements in this work are harmonic excited measurements the velocity decoder OVD-01 will be used and the displacement is calculated with equation 3.28 rearranged after \hat{x} . So the total measurement uncertainty V_{error} including the oscilloscope before scaling with the range (Table 3.2) is calculated with equation 3.21 [35].

3.2.3 Surface Pressure

The acoustic pressure p is also an important parameter and is usually measured with a microphone (Chapter 3.3). However, a rough estimation can be taken also from the surface velocity measurement of a vibrating surface (Chapter 3.2.2). Assuming a surface is infinite in two dimensions e.g. in $y-z$ and it is vibrating in x direction with a surface velocity \tilde{v} then this surface is emitting a plane wave. Therefore the pressure p and the particle velocity v depend on the direction of propagation x only. So that any spatial points either of the same pressure or any spatial points with the same particle velocity lies on the same plane. All of these points and so all planes are orthogonal to the direction of propagation. The dependency on only one variable, the spatial location, for the pressure and for the particle velocity simplifies Euler's equation of motion to [81]

$$\frac{\hat{p}}{\hat{v}} = \rho c_0 = Z_a \quad (3.29)$$

with the acoustical impedance Z_a , the density ρ of the media (air), the speed of sound c_0 and the amplitude of the pressure \hat{p} and the amplitude of the particle velocity \hat{v} . With the assumption the particle velocity is smaller than the speed of sound and those particles are smaller than the vibrating surface, which is measured by the LDVM, then the vibrating surface looks such as an infinite rigid plane against the small particles in front of it. So the particle velocity \hat{v} , near the surface, must be the same as surface velocity \tilde{v} , which is measured. Thus, with the acoustical impedance [81] of air $Z_a \approx 414 \frac{\text{Ns}}{\text{m}^3}$ the surface pressure can be estimated with equation 3.29

$$\hat{p} = \tilde{v} Z_a = \tilde{v} 414 \frac{\text{Ns}}{\text{m}^3}. \quad (3.30)$$

This estimation is also built in the LabVIEW™ program which is used to control the LDVM. So the surface velocity, the displacement and the surface pressure are measured.

Furthermore, when the sound pressure level is measured using a calibrated microphone (Chapter 3.3) the surface pressure can then be calculated using the "Diffraction Loss Calculator" written in Mathematica by René Golinske [9].

3.3 Sound Pressure Level

As mentioned before the sound pressure level (SPL) of an ultrasonic transducer is one of the most important characteristic property. The sound pressure level and its specific characteristics determine if an ultrasonic transducer is generally useful for an industrial application or even more for a specific one. The higher the sound pressure level the better. But this statement comes often with a trade off with one or more of some additional characteristics of the beam profile such as:

- Beam width of the main lobe;
- Side lobes, their position and width;
- Symmetry;
- Directivity.

Therefore a volumetric measurement setup, based on a goniometer, was built by Axel Jäger and Matthias Rutsch inside an anechoic chamber [Figure 3.14 (a), (b)] and a volumetric 3D stage was built by Maik Hoffmann [14]. Both setups are described and compared in most important properties.

3.3.1 Measurement Setup Based on a Goniometer

The entire measurement setup was built in an anechoic chamber with the dimensions of approximately $(7 \times 5 \times 5)\text{m}^3$ of usable workspace [Figure 3.14 (a)]. Its absorption coefficient is up to 99% of sound waves above 70 Hz [82]. This anechoic chamber minimizes almost any acoustic reflections if continuous measurements are required. Furthermore, this anechoic chamber reduces also any influence coming from the environment, e.g. heavy vehicle driving by or even some noise from inside the building, because it is positioned on 28 spiral springs. In doing so the chamber is mechanically decoupled from the rest of the building.

The basic measurement principle of this volumetric measurement setup, the Goniometer, is widely used in the lighting industry and research. It consists of two rotational axes and one translational linear axis. The two rotational axes are mounted on top of each other with an aluminum T-slot profile elbow of 90° [Figure 3.14 (b)]. The bottom one PI M-062.2S (Physik Instrumente (PI) GmbH & Co. KG, Karlsruhe, Baden-Wuerttemberg, Germany) is thereby rotating horizontally (θ -axis) and the top one PI M-061.2S (Physik Instrumente (PI) GmbH & Co. KG, Karlsruhe, Baden-Wuerttemberg, Germany) vertically (φ -axis). Each axis is controlled by a PI C-663 (Physik Instrumente (PI) GmbH & Co. KG, Karlsruhe, Baden-Wuerttemberg, Germany) controller. The top axis is holding a special designed mounting rack in which the DUTs are mounted properly. In such way that the front face of the DUT are perfectly centered to

Table 3.5: Main specification data of rotational stages M-061.2S and M-062.2S [83]

Properties M-061.2S (φ)	Values	Units	Annotations
Rotation range	> 360	$^{\circ}$	Rotary decoder
Design resolution	1.2	μrad	
Encoder steps	2000		
Minimum incremental motion	6	μrad	
Backlash	200	μrad	
Unidirectional repeatability	50	μrad	
Maximum load	550	N	
Velocity	9	$^{\circ}/\text{s}$	
Maximum torque $\Theta_x, \Theta_y, \Theta_z$	± 6	Nm	Maximum
Properties M-062.2S (θ)	Values	Units	Annotations
Rotation range	> 360	$^{\circ}$	Rotary decoder
Design resolution	0.96	μrad	
Encoder steps	2000		
Minimum incremental motion	5	μrad	
Backlash	240	μrad	
Unidirectional repeatability	60	μrad	
Maximum load	650	N	
Velocity	7.5	$^{\circ}/\text{s}$	
Maximum torque Θ_x, Θ_y	± 7	Nm	Maximum
Maximum torque Θ_z	± 8	Nm	

Table 3.6: Main specification of the 4138-A-015 microphone unit [85]

Properties	Values	Units	Annotations
Pressure filed response	0.0065 – 140	kHz	± 2 dB
Max. sound pressure level	171	dB	peak
Combined sensitivity (2670)	-65.8	dB	Ref. 1 V/Pa
Combined sensitivity (2670)	0.513	mV/Pa	
Polarization voltage	200	V	external through Type 2829

both rotational axes. This guarantees always the same distance the microphone, which is measuring the sound pressure level, when rotating 180° in the horizontal plane and 360° in the vertical plane.

This microphone is a calibrated 1/8" 4138-A-015 microphone combination (Brüel & Kjær, Nærum, Denmark) (Table 3.6) with a 1/4" 2670 preamplifier (Brüel & Kjær, Nærum, Denmark). It is mounted on the 6m translational linear axis LEZ 1 L5998 (isel Gemany AG, Eichenzell, Hessia, Germany) [Figure 3.14 (a)] driven by a MS135HT2 stepper motor (isel Gemany AG, Eichenzell, Hessia, Germany) [84]. This combination has a accuracy of ± 0.2 mm [84]. Thereby it is facing up so the free field response is measured. Furthermore, the translational linear stage is covered completely in felting to minimize any reflections. In such way, that the microphone can move freely through an opening such as a zipper principle. The movement of the translational linear stage is referred to r -axis.

Table 3.7: Main specification data of NI PXI-5922 24-Bit PXI oscilloscope [88]

Properties	Values	Units	Annotations
Full scale range (2 or 10)	± 1 or ± 5	V	
Resolution	16 – 24	bits	
Sample rate	15 – 0.05	MS/s	
Channel	2		
Input impedance	$50\ \Omega$ or $1\ \text{M}\Omega$		
DC accuracy	$\pm(500\ \text{ppm of input} + 50\ \mu\text{V})$		2V range
DC accuracy	$\pm(500\ \text{ppm of input} + 100\ \mu\text{V})$		10V range
DC drift	$\pm(20\ \text{ppm of input} + 5\ \mu\text{V per } ^\circ\text{C})$		2V range
DC drift	$\pm(20\ \text{ppm of input} + 10\ \mu\text{V per } ^\circ\text{C})$		10V range

The DUTs are driven by an Keysight 33522B-OCX waveform generator to provide a stable excitation signal (Chapter 3.1.2. Again if higher signal level amplitudes are needed then the amplifier SL2400 can be used to amplify the output signal. For data acquisition a high resolution PXI-5922 24 Bit (National Instruments, Austin, TX, USA) data acquisition card is used. For most of the measurements this card is set to 1 MS/s, which gives 22Bit of resolution (Table 3.7). Therefore, the overall noise floor of the goniometer inside the anechoic chamber is $\text{Noise}_{\text{RMS}} \pm 1\ \sigma = (60.7 \pm 0.6)\ \text{dB SPL}$ [86, 87].

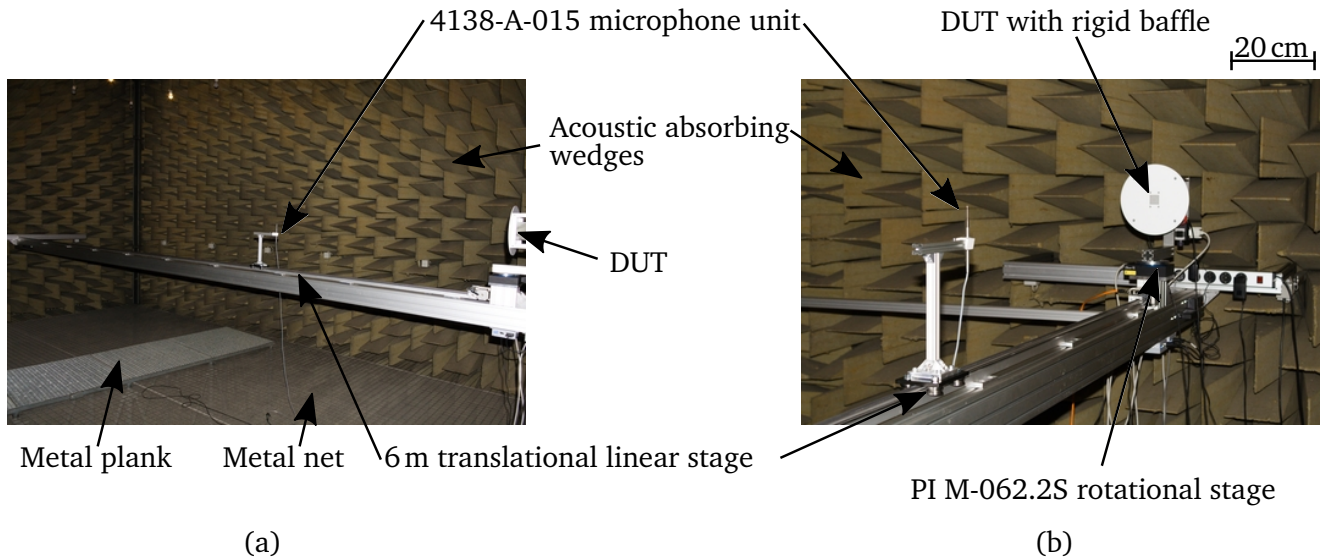


Figure 3.14: Volumetric sound pressure measurement setup built in anechoic chamber with acoustic absorbing wedges mounted at all walls with 6 m translational linear stage with microphone unit (a) and DUT fixed in a rigid baffle mounted on rotational stages (b). Annotation, the felting is not mounted to show the mechanical translational linear stage. Copyright Matthias Rutsch [87]

The entire measurement setup is again controlled by a standard PC with Windows[®] 10 64 Bit and a LabVIEW[™] (32Bit Fall) Bit program. The measured data including position of the axes, in spherical coordinate form, are stored in a text file for post processing. Also the A-scans of the measured waveforms stored in a binary file format of 64Bit real values with little endian convention [87].

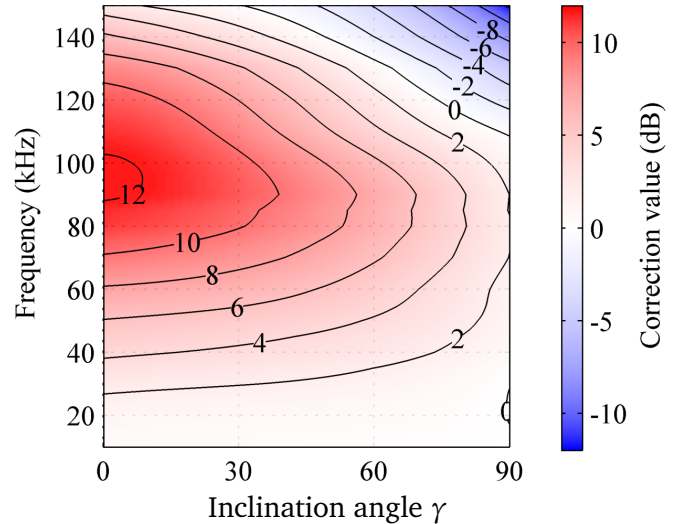
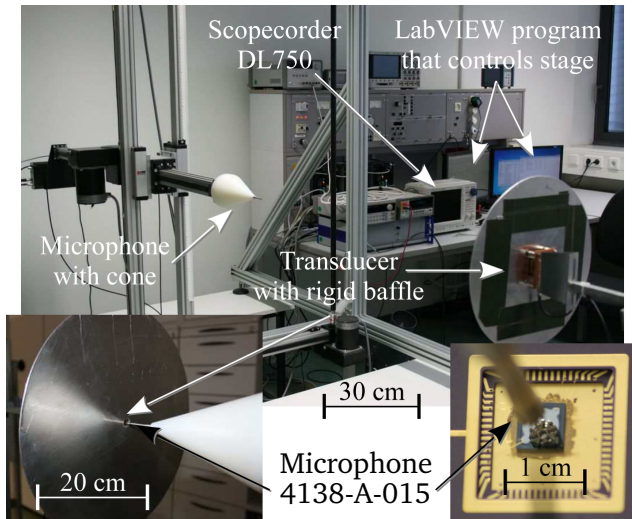
3.3.2 Measurement Setup Based on 3D Linear Stages

The entire setup of the 3D linear stage scanning system was built in a standard laboratory environment and is controlled via a standard PC using Windows® 7 Professional 64-Bit and LabVIEW™ (32-Bit, 2014 Fall). The system consists of X-Y-Z aluminum T-slot profiles translational linear stages (BAHR Modultechnik, Luhden, Lower Saxony, Germany) which are driven by a stepper motor SM 87 218 M6N (Stögra Antriebstechnik eh. Zebotronics, Bavaria, Munic) and controlled via stepper motor controller PP 92–70 (Phyton-Elektonic GmbH, Gröbenzell, Bavaria, Germany) each. They mounted in a way that a volume of 1 m^3 can be screened [14]. The axes X-Y-Z move a calibrated microphone - B&K 4138-A-015 (Brüel & Kjær, Nærum, Denmark) (Table 3.6), which is mounted on the Z-axis facing horizontally against the DUT [Figure 3.15 (a) and inlets]. Hence, the measured sound pressure levels have to be corrected by a free field correction factor [Figure 3.15 (b)], depending on the inclination angle of the acoustic sound pressure wave hitting the microphone membrane [89]. Furthermore, the microphone housing is capsuled in a teflon cone, therewith the Z-axis is mostly hidden behind this cone and direct reflections are minimized by reflecting intentionally to all sides of X and Y through the shape of the cone [Figure 3.15 (a) and left inlet] Here the DUT is mounted in a fixed position, unlike the goniometer in a non-moving position, centered relative to X and Y [Figure 3.15 (a)].

The data acquisition is done via a Scopecorder DL750 (YOKOGAWA™, Musashino, Tokio, Japan). It is a combination of an oscilloscope and a long term data recorder and can be equipped modular by with up to eight data acquisition modules [90]. Here a 16-Bit isolated module 701251 (YOKOGAWA™, Musashino, Tokio, Japan) with a sample rate or 1 MS/s is used. A sufficient bandwidth of 200 kHz is given for measurements of air coupled ultrasonic transducers below 200 kHz . This module delivers in combination with the microphone unit a noise level of the entire system of $75\text{ }\mu\text{V}$ without any averaging [14]. This corresponds to a sound pressure level of 73 dB SPL .

Upgrading the system by a high resolution data acquisition card PXI-5922 24 Bit (National Instruments, Austin, TX, USA) improved the performance even more (Table 3.7). Therefore, the overall noise level of the 3D linear stage scanning system inside a standard laboratory using expectation time window, to avoid any interference due to reflections, could be reduced to overall $55\text{ }\mu\text{V}$, which corresponds to a sound pressure level of 68 dB SPL .

In a direct comparison both volumetric measurement systems are accurate and precise tools to characterize the sound pressure field of air coupled ultrasonic transducers. Where one or another system has some advantages and also some disadvantages (Table 3.8). The advantage of the 3D linear stage volumetric measurement system is the simplicity of the cartesian coordinates and therewith the same resolution in any direction of X-Y-Z. The goniometer volumetric measurement system is able to characterize a bigger volume with more dynamic range of $\approx 110\text{ dB SPL}$, without averaging, due to the overall lower noise level. It is also faster, cause less mass has to be moved, in a smarter way e.g. by simply rotation, in each measurement step.



(a)

(b)

Figure 3.15: Volumetric sound pressure measurement setup based on 3D linear stages (a) and extrapolated correction values for the free field response for the B&K 4138-A-015 microphone combination (b). [14]

3.3.3 Sound Pressure Field

Since it is not so intuitive, the sound pressure field measurements is described using the goniometer. Loading the LabVIEW™ program with a precomputed coordinates matrix using a MATLAB R2017b measures automatic in a time optimized moving pattern the sound pressure field in front of a DUT. Thereby the DUT has to be mounted in a rigid baffle [Figure 3.14 (b)] and is then rotating horizontally and vertically. Is one entire rotation set is measured then the microphone is moving one step further away and the rotation of the DUT starts over. In doing so a half spheres of a half solid angle $\Omega = 2\pi$ is measured. Next plotting all the half spheres at once is the adding up to a complete volumetric scan of the sound pressure field of the DUT. Since these measurement consist of several thousand points it takes many hours to gather the data. Furthermore the gathered information is often redundant in each half sphere. The sound pressure level decays in the far field with $1/R$ behavior where R is the distance to the source also the radius [16]. So it is enough to measure one half sphere and weight the sound pressure level with $1/R$. However, in the near field or if the setup is deliberately built with reflections the entire volume has to be measured.

Besides half sphere sound pressure level measurements other patterns can be performed as well. So, measurement along the r -axis only can give a quick overview of the sound pressure level trend of a DUT within distance. Furthermore, a scan along the θ -axis at a given distance allowing the visualization of the beam profiles. Same as for the volumetric scans when rotating around the θ -axis only and varying thereby the distance of the microphone at the r -axis slice of a plane can be measured.

Table 3.8: Comparison of volumetric measurement systems 3D stage linear vs. Goniometer.

*Depends on the measurement pattern.

**Depends on the combined sensitivity of the microphone unit and using PXI-5922 data acquisition.

Property	3D linear stage	Goniometer
Measurement pattern	cartesian coordinates	spherical coordinates
Measurement time (30000 points)	≈ 8 h	≈ 2.5 h*
Maximum measurement volume	1 m^3	$144\pi \text{ m}^3$
Free field correction	yes [Figure 3.15 (b)]	no
Spatial resolution	$50 \mu\text{m}$ any direction	$200 \mu\text{m}$ in z-direction ($0.05 - 30$) μm at ($0.01 - 6$) m θ -axis ($0.06 - 36$) μm at ($0.01 - 6$) m φ -axis
Noise level without averaging**	68 dB SPL	(60.7 ± 0.6) dB SPL
Maximum sound pressure level	≈ 171 dB SPL	≈ 171 dB SPL
Dynamic range**	≈ 103 dB SPL	≈ 110 dB SPL

3.4 Schlieren Photography Setup

Especially for industrial application, the knowledge of shape of the ultrasound beam is an advantage for the design process e.g. ultrasonic flow meters (UFMs). Besides measurements methods which were used to obtain quantity numbers e.g. electrical impedance, surface velocity, or sound pressure levels, also methods which can mostly deliver only quality statements can be useful for the characterization of ultrasonic transducers. The Schlieren photography is one of them.

The Schlieren photography is based on the utilization of the refractive index of light. Usually light spreads and moves uniformly in a homogeneous media. However, light also gets diffracted at boundary layers with different refractive indices. Such areas e.g. with different pressure or temperature have a different refractive index and they are called a Schliere [91]. The pressure or temperature differences are then visualized as light and dark areas respectively. So a quality statement of the sound pressure field of DUT, the ultrasonic transducer can be obtained.

3.4.1 Schlieren Setup

The Schlieren setup built by Yannik Bendel [91] consists of a LED light source, a parabolic mirror, a razor blade as a aperture and a digital single lens reflex camera (DSLR) (Figure 3.16). Hereby the LED light source is synchronized with the excitation signal of the ultrasonic transducer of which the sound pressure field is visualized. The parabolic mirror has a diameter of 200 mm (GSO Newton Hauptspiegel 8" f/4) and a focal length of $f_1 = 800$ mm. Therefore the light source and the aperture made of a razor blade have a distance of $L = 2f_1 = 1600$ mm (Figure 3.16). The mirror is mounted on aluminum T-slot profiles and is facing with its opening towards the camera (Figure 3.16). The camera a Canon 1300D (Canon Inc., Ōta, Tokio, Japan) is equipped with a Canon EF 100/2.8 L IS Marco USM lens (anon Inc., Ōta, Tokio, Japan). The DUT is placed direct in front of the mirror and the Schliere is then photographed

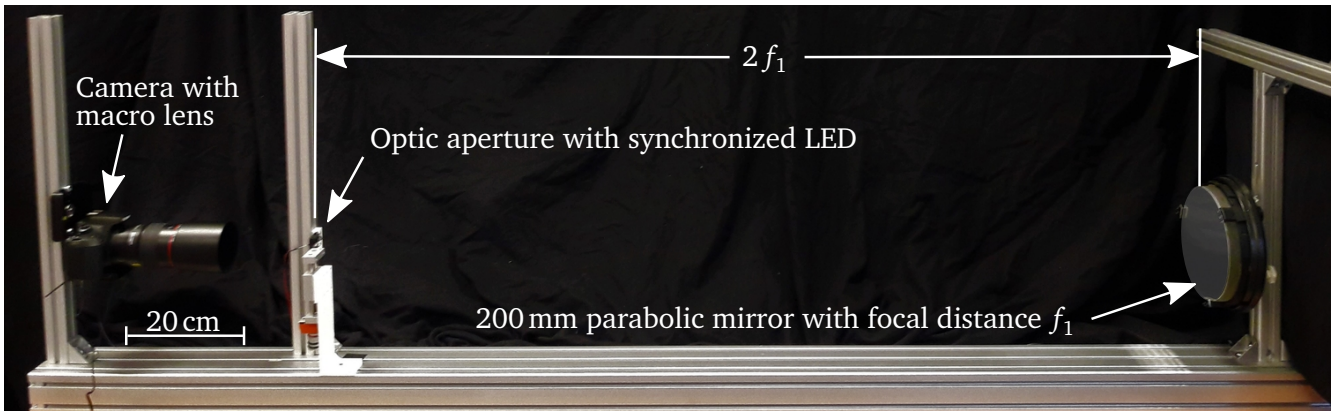


Figure 3.16: Schlieren setup with a parabolic mirror with a focal length of $f_1 = 800$ mm facing towards the optic aperture and camera. Copyright Yannick Bendel [91].

by the camera but cut of by the razor blade, the aperture or the optic filter. The entire Schlieren setup is controlled with MATLAB R2018a (The MathWorks[®], Natick, MA, USA).

3.4.2 Sound Pressure Field

Using the Schlieren setup several ultrasonic transducers were investigated by Yannick Bendel [91]. So the ultrasonic wave distribution of a 40 kHz Murata ultrasonic transducer with a diameter of 16 mm MA40B8S (Murata Manufacturing Co. Ltd., Higashikotari, Kyōto, Japan) is visualized [Figure 3.17 (a)]. The directivity pattern of this DUT can be seen more clearly by the light and dark areas after the post processing [Figure 3.17 (b)] due to the enhanced contrast. The sound pressure maxima and minima represented by the light and dark areas express the wavelength of 8.575 mm as the distance between them.

A 40 kHz parametric array consisting of 222 MA40S4S Murata ultrasonic transducer with a diameter of 180 mm built by Matthias Rutsch [92] emits an almost planar wave [Figure 3.18 (a)], due to its large aperture size in comparison to the wavelength of 8.575 mm. So it is ideal to be used as a 40 kHz ultrasound source. Therefore a 1D phased array could be investigated in receive mode [5] using a planar wave generated by this parametric array. In contrast to this parametric array, a focused array [93], where the ultrasonic transducer are mounted in a parabolic manner to create a focus, and, thus, a higher sound pressure in there but in a small area only [Figure 3.18 (b)]. Even without enhancing the contrast in a post process more difference in contrast can already be seen, which indicates a higher sound pressure than at the parametric array [Figure 3.18 (a)]. Also the resulting sound pressure field due to interferences and effacements can clearly be captured.

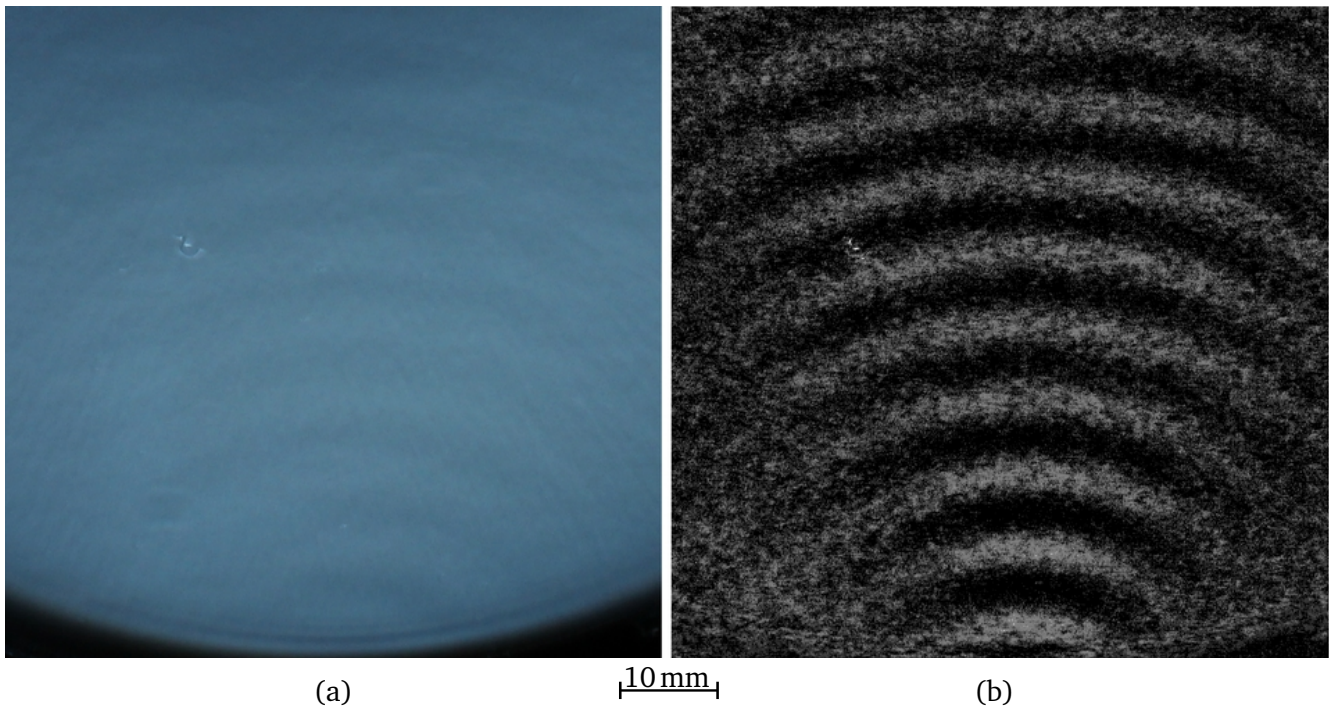


Figure 3.17: Schlieren photography of a 16 mm MA40B8S ultrasonic transducer (a) [91] and post processed to enhance to contrast (b) [91]. The directivity pattern of the ultrasonic wave can be clearly seen, visualized by the light and dark areas (b) due to the pressure differences. The DUT is located down below the frame of the captured image.

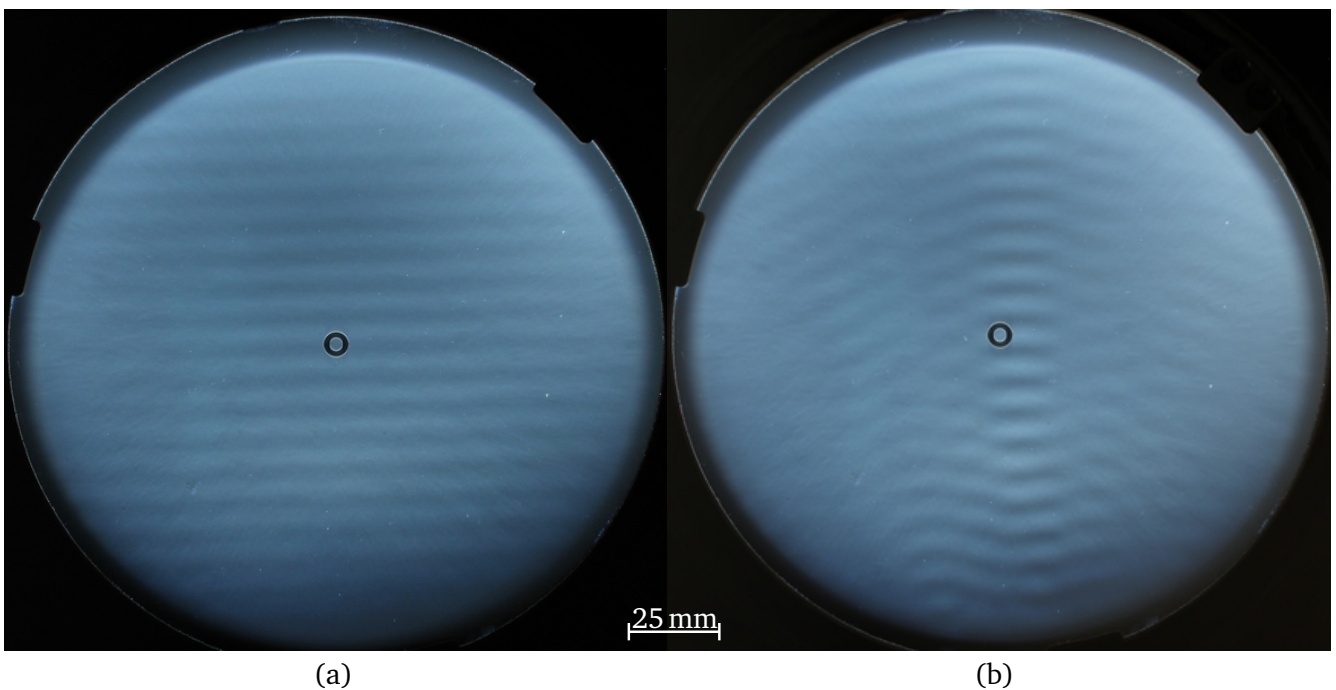


Figure 3.18: Schlieren photography of a parametric array (a) [92] with an almost planar ultrasonic wave distribution and a focused array (b) [93] where the focus effect is visualized [91]. The parametric array (a) was used to characterize the 1D phased array with separation of the acoustic aperture by a smart packaging layer (Chapter 5) [5]. The DUTs are located down below the frames of the captured images.

4 Automatic Parameter Extraction

This Chapter describes several variations and extensions of the Butterworth-van Dyke model, which are needed to characterize ultrasonic transducers in a more detailed way depending on the type and additional physical effects. Here the focus lies on a 5-elements, 6-elements, and on a 7-elements model all based on the standard 4-elements BvD model (Chapter 2.3). A complex curve fit algorithm is introduced, analyzed and implemented in MATLAB[®] and a second one using Mathematica. Based on these curve fit results important parameters (Chapter 2.3) are extracted. It is used to fit these model to the measured electrical impedance data.

An important method of characterization of ultrasonic transducers is the electrical impedance measurement (Chapter 3.1.1, 3.1.2). This method is quick and can be performed already direct during a fabrication process of ultrasonic transducers. For example characterizing piezoelectric layer or disks (Chapter 2.2.1) before or after assembling as a first functionally test. During a CMUT fabrication the electrical impedance can already be measured in-situ direct on wafer level with special contact probes. Before dicing the wafer and bonding each individual element (Chapter 2.2.2) can be tested and evaluated. In doing so, the fabrication process and parameters can be monitored and therefore yield can be optimized.

However, after the electrical impedance is measured, these data need to be analyzed. Hence, the automatic parameter extraction of useful information and parameter is necessary, since there are many of them such as short and open circuit resonances, quality factors at these resonance frequencies, bandwidths, coupling efficiencies and the equivalent circuit parameters of the BvD model itself (Chapter 2.3) [94]. These parameters can directly being used to understand and optimize a CMUT fabrication process for example, due to the analogies between electrical and mechanical domain (Chapter 2.3) [94]. In order to fulfill these tasks of an automatic parameter extraction, is a need of a good model, an equivalent circuit and a robust algorithm to extract these parameters.

4.1 Extended Butterworth-van Dyke Model

Only a selection of common important extensions of BvD models are introduced and described. The Butterworth-van Dyke (BvD) model is an equivalent circuit based on 4-elements (Chapter 2.3) [46, 49], which is used to describe quartz oscillator, piezoelectric, or electrostatic ultrasonic transducer. However, the BvD model [Figure 4.1 (a)] is not sufficient enough to explain various additional physical effects and has to be extended [95, 96].

- 5-elements model

So it is common to add a fifth element to the standard BvD model. This fifth element can be seen as a contact resistance R_c [Figure 4.1 (b)]. Such additional contact resistance is often related to the resistance of the silver epoxy glue to contact the back electrode or it is based on too thin or to

less bonding wires e.g. CMUTs fabrication. Bad ohmic contacts can also occur due to the lower conductance of polysilicon [97].

- 6-elements model

It is known when a bulk component such as in high temperature langasite resonators is present [98] then a parallel resistance R_p [Figure 4.1 (c)] is added to the BvD model [95]. This parallel resistance is often a temperature dependent component [95] and to minimize the fit effort, of fitting algorithms, this parameter is often extracted by low impedance spectra data and fed then as a good start value into the fitting algorithm [95]. This parallel resistance can also being seen as a non ideal dielectric material of the capacitor C_p .

- 6-elements model

Going back to the 5-elements model [Figure 4.1 (b)], a parasitic contact capacitance has to be considered as well. In general a bad ohmic contact acts in addition as a capacitance depending on the frequency. Often this parasitic contact capacitance C_c [Figure 4.1 (d)] affects the ultrasonic transducer operating at higher frequency usually more than such devices working at lower frequencies.

- 7-elements model

Finally the 7-elements model [Figure 4.1 (e)], which is the combination of the two 6-elements models [Figure 4.1 (c)] and [Figure 4.1 (d)]. Here actually all introduced extra parameter are combined in one. Meaning it represents a BvD model or an ultrasonic transducer which has a bad ohmic contact and introducing a parasitic capacitance due to its higher frequency of operation and the electrodes having a bad electrical insulation.

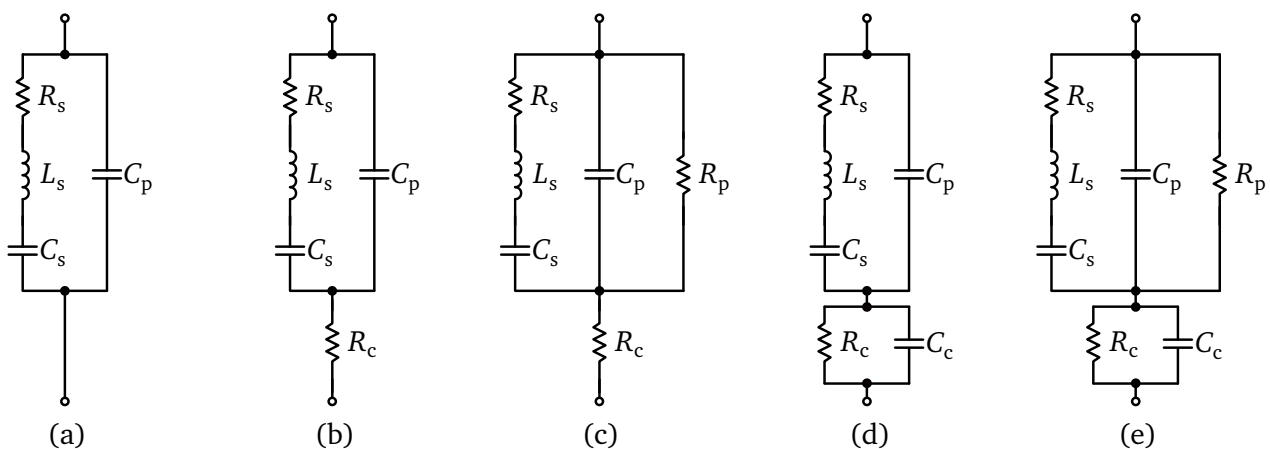


Figure 4.1: Overview of a selection of the different extensions of the original BvD model (a). The 5-elements model, BvD model extended with a contact resistance R_c (b). A 6-elements model, with R_c and an additional parallel resistance R_p (c). Another 6-elements model, with R_c with an additional contact capacitance C_c (d). The 7-elements model, with R_c , C_c and R_p .

4.2 Extended 7-elements Butterworth-van Dyke Model and the Influence of its Parameters

Before fitting a model to a set of measured data, the model has to be found first. Especially when new DUTs were measured and their behavior can not be described well with the standard BvD (Chapter 4.3.2) due to additional physical effects. Here the influence of the seven parameter extended BvD model are described individually. Thus, this model was investigated using a LabVIEW™ program written by the author (Chapter 4.3.2, Figure 4.10). In doing so step by step a good model can be found and the complex curve fit algorithm has a chance to fit in the first place. Denotation the following seven figures are all structures as follow:

- All plots are normalized on the abscissa to the short circuit resonance frequencies;
- Every figure consists of four subplots from top to bottom as:
 - (a) The Magnitude of $|Z|$;
 - (b) the phase φ_Z ;
 - (c) the real part $\Re\{Z\}$;
 - (d) the imaginary part $\Im\{Z\}$.
- Every subplot consists of seven plots;
- Thereby the scale is always fixed;
- Within the same type of subplot the scale is always the same;
- Subplots (a) and (c) are scaled logarithmic;
- Subplots (b) and (d) are scaled linear;
- Subplots (b) and (d) are scaled symmetric positive and negative;
- Subplots (a), (c), and (d) are scaled in the same order of magnitude;
- Only the indicated parameter was varied at once;
- The parameter was always increased in the direction as the arrow points;
- The indices mark the points where individual significant changes take place;
- Parameter who were not varied were held at their individual center value.

First parameter, the series resistance R_s , was varied and all other parameters were held fixed (Figure 4.2). With increasing R_s the magnitude of the impedance is flattened, so the magnitude value of the open circuit resonance is decreased and the short circuit resonance is increased. Furthermore both resonance frequencies become more separate [Figure 4.2 (a) R_{s1} and R_{s2}], which can be explained by equation 2.16 and 2.17. Therewith comes an increased coupling efficiency (Equation 2.27). This behavior is non-intuitive, because a resistance does not depend on frequency.

The phase is flattened out too. At the short circuit resonance side the phase is lifted more [Figure 4.2 (b) R_{s2}] than on the open circuit resonance side [Figure 4.2 (b) R_{s3}]. Therewith the slope becomes flatter on both resonance frequencies, the flatter these slopes the more broadband but also more damped the ultrasonic transducer. The maximum peak of the phase is decreased and shifted slightly to higher frequencies [Figure 4.2 (b) R_{s1}]. The overall a separation of the zero crossings of the phase leads to a more broadband but less efficient ultrasonic transducer.

The real part is flattened overall as well and the change of the shape is similar to the change of the phase. The short circuit resonance side is again more affected than the open circuit resonance side [Figure 4.2 (c) R_{s1} and R_{s3}]. As conclusion, a variation R_s affects the real part in an asymmetric way. Since on both sides the real part increases so it is indicating more damping. However, whenever operating in between the resonance frequencies the damping decreases with increased R_s [Figure 4.2 (c) R_{s1}].

The imaginary part flattened as well but the effect is only in the range of the resonance frequencies. Here the maximum and the minimum and therefore the zero crossings separate again [Figure 4.2 (c) R_{s1} and R_{s2}] with increased R_s , indicating the increased coupling efficiency.

Second parameter, the series inductance L_s , was varied and all other parameters were held fixed (Figure 4.3). It is well known that an inductance or better its reactance is frequency dependent. Therefore the influence of L_s is more significant over the frequency range. With increased L_s both resonance frequencies, respectively their minima and maxima of the magnitude of the impedance, getting shifted to lower frequencies [Figure 4.3 (a) L_{s1}]. Thereby an overall slightly increased magnitude was observed [Figure 4.3 (a) L_{s3}]. Furthermore the resonance frequencies are less separated [Figure 4.3 (a) L_{s2}], so the coupling efficiency is decreased (Equation 2.27).

The phase is shifted overall to lower frequencies [Figure 4.3 (b) L_{s1}] as well with increased L_s , it becomes more narrow and its slopes become steeper [Figure 4.3 (b) L_{s2}]. The maximum peak of the phase is slightly increased.

The same frequency shift to lower frequencies was observed in the real part [Figure 4.3 (c) L_{s1}] and as well in the imaginary part [Figure 4.3 (d) L_{s1}] with increasing L_s . Again the overall shapes become less separated, therewith the zero crossings, [Figure 4.3 (d) L_{s2}] and the values of minimum and maximum getting slightly increased [Figure 4.3 (d) L_{s3}].

Third parameter, the series capacitance C_s , was varied and all other parameters were held fixed (Figure 4.4). With increased C_s also both resonance frequencies and thus the maximum and minimum of the magnitude of the impedance are shifted to lower frequencies [Figure 4.4 (a) C_{s1}] such as it happens when L_s was increased. The values of the magnitudes become lower at minimum and higher at maximum respectively [Figure 4.4 (a) C_{s3}]. But unlike before here the resonance frequencies are now separated [Figure 4.4 (a) C_{s2}] which indicates a better coupling efficiency (Equation 2.27).

The phase is shifted also the lower frequency values [Figure 4.4 (a) C_{s1}] and is widened [Figure 4.4 (b) C_{s2}]. So the coupling efficiency is slightly increased.

Again the real part and the imaginary part are shifted to lower frequency values [Figure 4.4 (c) C_{s1} , (d) C_{s1}]. Thereby both values, minimum and maximum of the imaginary part are slightly decreased and increased respectively, [Figure 4.4 (d) C_{s2}].

Fourth parameter, the parallel capacitance C_p , was varied and all other parameters were held fixed (Figure 4.5). Increasing C_p , meaning the electrodes of an ultrasonic transducer are bigger or have less distance to each other, reduces the magnitude of the impedance [Figure 4.5 (a) C_{p3}], whereby the effect is more significant at higher frequencies [Figure 4.5 (a) C_{p2}] (Equation 2.10). Only a small range around the short resonance frequency becomes slightly larger and the short circuit resonance is getting shifted to lower frequency [Figure 4.5 (a) C_{p4}] but only a small fraction of the shift of the open circuit resonance frequency [Figure 4.5 (a) C_{p1}]. Again the coupling efficiency is decreased (Equation 2.27).

Like the magnitude also the phase is affected asymmetrically by increasing C_p and the zero crossing of the open circuit resonance frequency is more shifted to lower frequencies [Figure 4.5 (b) C_{p2}]. Also the overall phase becomes lower [Figure 4.5 (b) C_{p4}], even below zero [Figure 4.5 (b) C_{p1}]. When C_p is further increased then the phase becomes higher again [Figure 4.5 (b) C_{p*}]. The short circuit resonance side is hardly affected [Figure 4.5 (b) C_{p3}]

The real part becomes smaller [Figure 4.5 (c) C_{p1} and C_{p2}] such as the magnitude of the impedance. Again the affect is asymmetric with more influence at higher frequencies [Figure 4.5 (c) C_{p1}] whereby the rising slope increases [Figure 4.5 (c) C_{p3}].

However, the imaginary part increases overall again asymmetrically [Figure 4.5 (d) C_{p2} and C_{p3}]. At the same time the imaginary part is flattened out [Figure 4.5 (d) C_{p4}] and the shape, therewith its peaks, are shifted to lower frequencies [Figure 4.5 (d) C_{p1}].

Fifth parameter, the contact resistance R_c , was varied and all other parameters were held fixed (Figure 4.6). The influence of an increasing contact resistance is relatively small against the other parameters. But in combination with a parasitic parallel capacitance interesting phenomenas can be observed such as the change of directions of the shifts [Figure 4.6 (a) R_{c*} and R_{c**}]. However, the short circuit resonance frequency is more affected [Figure 4.6 (a) R_{c*}]. The magnitude of the impedance is overall slightly increased [Figure 4.6 (a) R_{c1}].

The phase is again affected asymmetrically, the short circuit resonance side is shifted to higher frequencies [Figure 4.6 (b) R_{c2}] and the open circuit resonance is hardly affected. Furthermore the phase is shifted up and with higher contact resistance shifted down again [Figure 4.6 (b) R_{c*}] and it is slightly damped [Figure 4.6 (a) R_{c1} and R_{c3}].

The real part shows similar behavior but not in the range of its maximum. First it is shifted up and then down again [Figure 4.6 (c) R_{c*} and R_{c**}]. The influence on the imaginary part is almost negligible small [Figure 4.6 (d) R_{c1} , R_{c2} , and R_{c3}].

Sixth parameter, the parallel resistance R_p , was varied and all other parameters were held fixed (Figure 4.7). The parasitic parallel resistance shifts mostly the open circuit resonance frequency to

lower frequencies and thereby the magnitude or the impedance is higher [Figure 4.7 (a) R_{p2}]. However the short circuit resonance and its magnitude of the impedance is affected less [Figure 4.7 (a) R_{p1}] and is only slightly increased.

The phase is also affected asymmetric, so the slope of the open circuit resonance is getting steeper [Figure 4.7 (b) R_{p1}]. The maximum peak of the phase is getting higher [Figure 4.7 (b) R_{p2}] and is slightly shifted to higher frequencies. The rest of the phase is getting lower [Figure 4.7 (b) R_{p3}].

Here again the real part shows similar behavior of the change such as the phase but with higher order of magnitudes [Figure 4.7 (c) R_{p1} and R_{p1}]. The overall real part is shifted to lower values, only its maximum is shifted to higher values instead [Figure 4.7 (c) R_{p3}]. Furthermore the maximum peak is shifted to lower frequencies.

The imaginary part is overall less affected when the parasitic parallel resistance is increased [Figure 4.7 (d) R_{p2}]. However, the open circuit resonance side is shifted stronger towards lower values and becomes more dominant [Figure 4.7 (d) R_{p1}].

Seventh parameter C_c was varied and all other parameters were held fixed (Figure 4.8). Compared to the other parameters the parasitic contact capacitance has only a smaller influence such as the contact resistance. So the overall magnitude of the impedance is shifted to lower values [Figure 4.8 (a) C_{c2}] and the short circuit resonance frequency is getting lower [Figure 4.8 (a) C_{c1}] in values than the open circuit resonance.

The phase however experiences again a change of its direction of its shift. First it becomes lower, more capacitive, and then the phase values getting increased again [Figure 4.8 (b) C_{c*}]. The slope of the short circuit resonance is getting steeper [Figure 4.8 (b) C_{c2}] and the peak of the phase is shifted to lower frequencies with getting higher in its values [Figure 4.8 (b) C_{c1}].

The real part however is only shifted to smaller values besides the range of the resonance frequencies [Figure 4.8 (c) C_{c1}]. Its peak values stay more or less the same. The imaginary part is again less affected but it is changing the direction of the value shift [Figure 4.8 (d) C_{c*}].

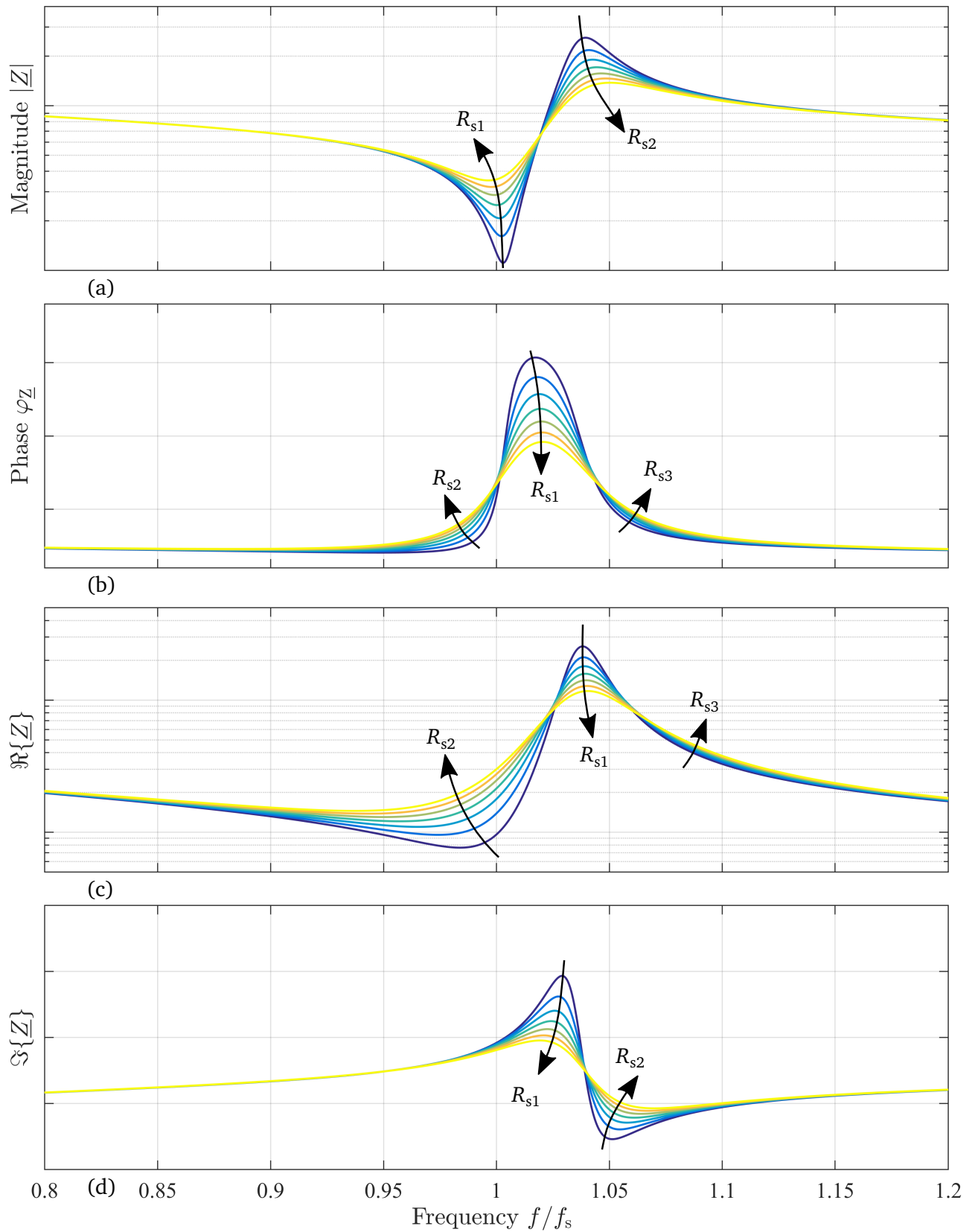


Figure 4.2: Dependency on the series resistance R_s of the 7-elements extended BvD model. For the logarithmic magnitude (a), the linear phase (b), logarithmic real part (c), and linear imaginary part (d) of the complex electrical impedance \underline{Z} normalized to short circuit resonance frequency. Only R_s is varied, increasing in direction of arrow.

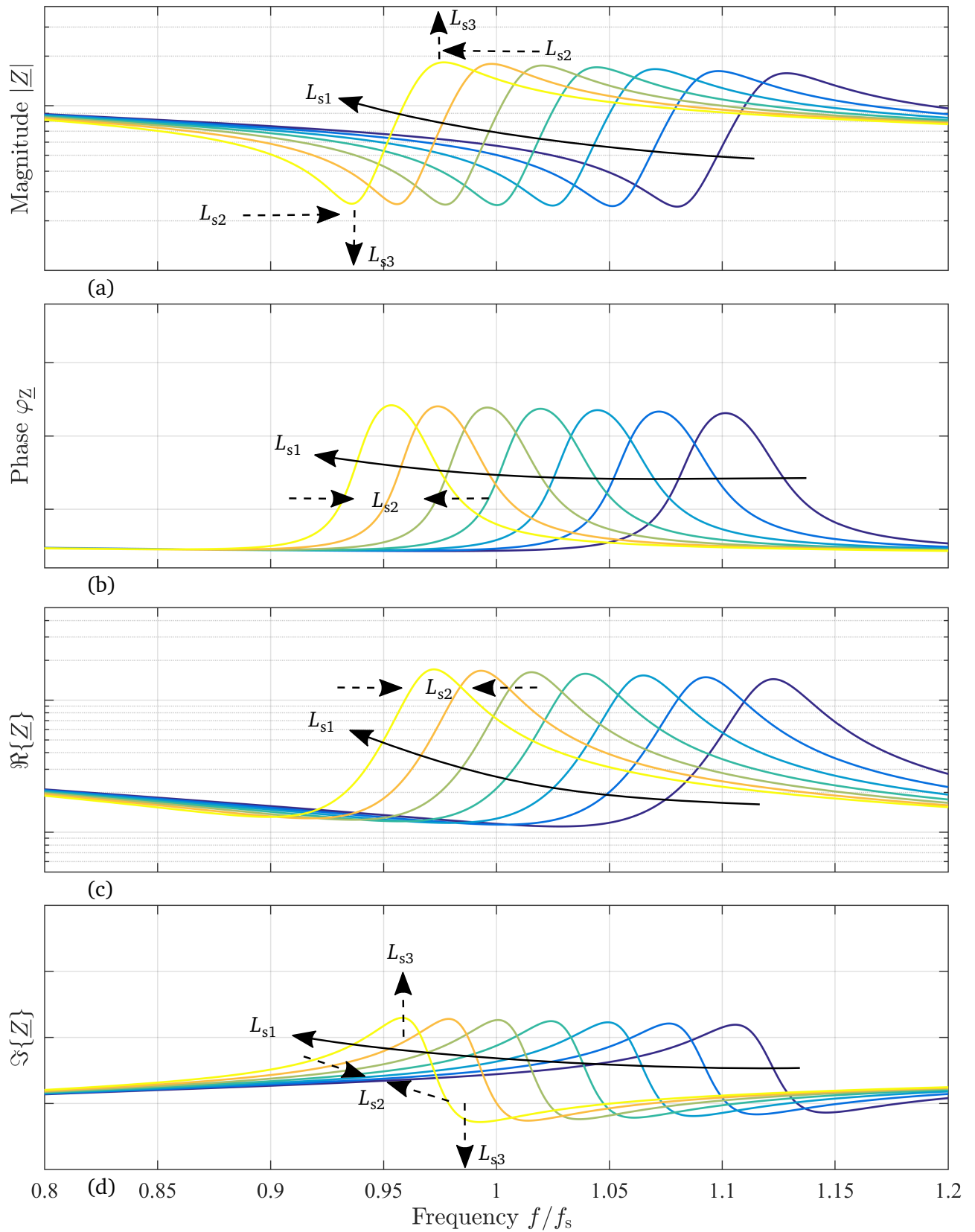


Figure 4.3: Dependency on the series inductance L_s of the 7-elements extended BvD model. For the logarithmic magnitude (a), the linear phase (b), logarithmic real part (c), and linear imaginary part (d) of the complex electrical impedance \underline{Z} normalized to short circuit resonance frequency. Only L_s is varied, increasing in direction of arrow.

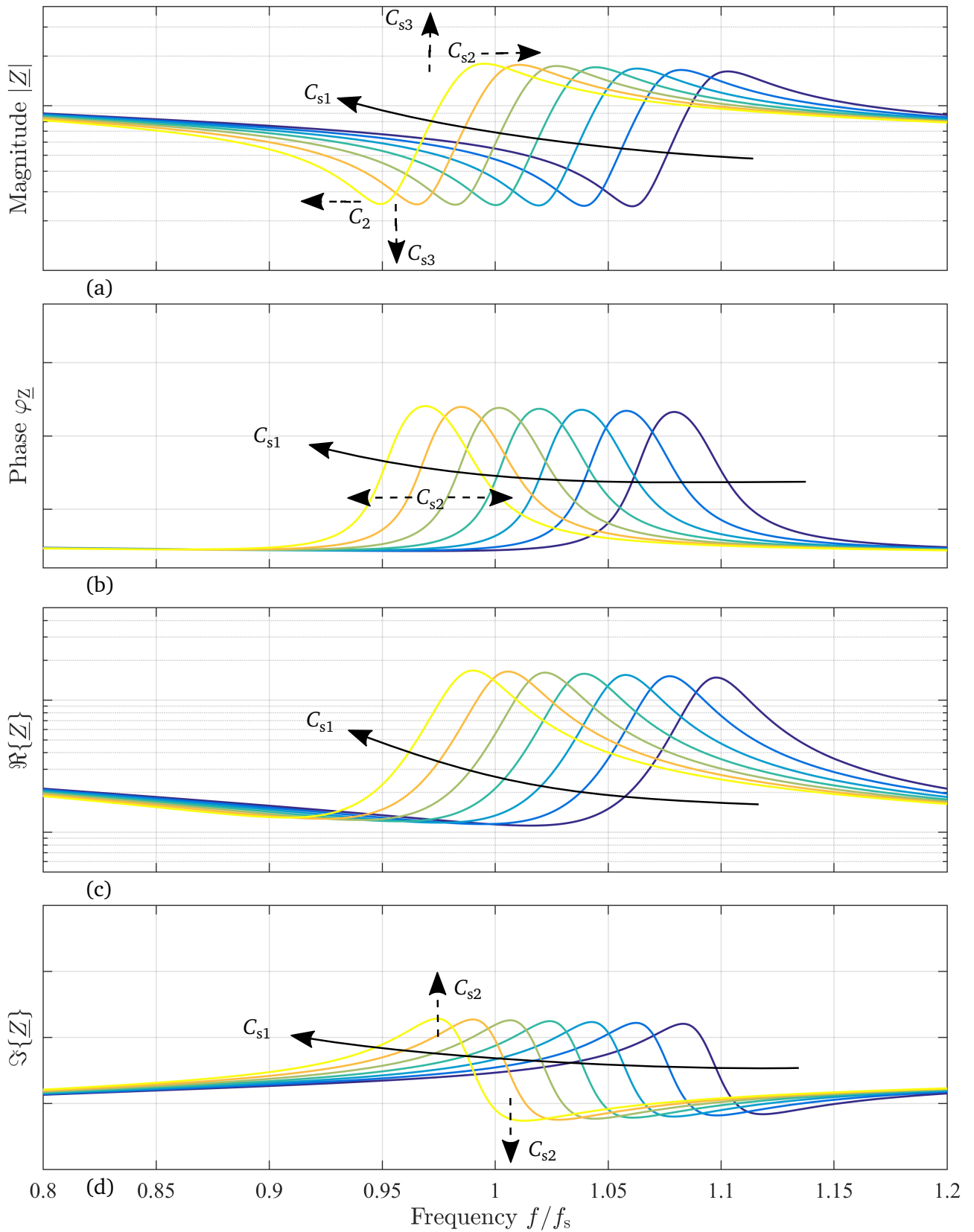


Figure 4.4: Dependency on the series capacitance C_s of the 7-elements extended BvD model. For the logarithmic magnitude (a), the linear phase (b), logarithmic real part (c), and linear imaginary part (d) of the complex electrical impedance \underline{Z} normalized to short circuit resonance frequency. Only C_s is varied, increasing in direction of arrow.

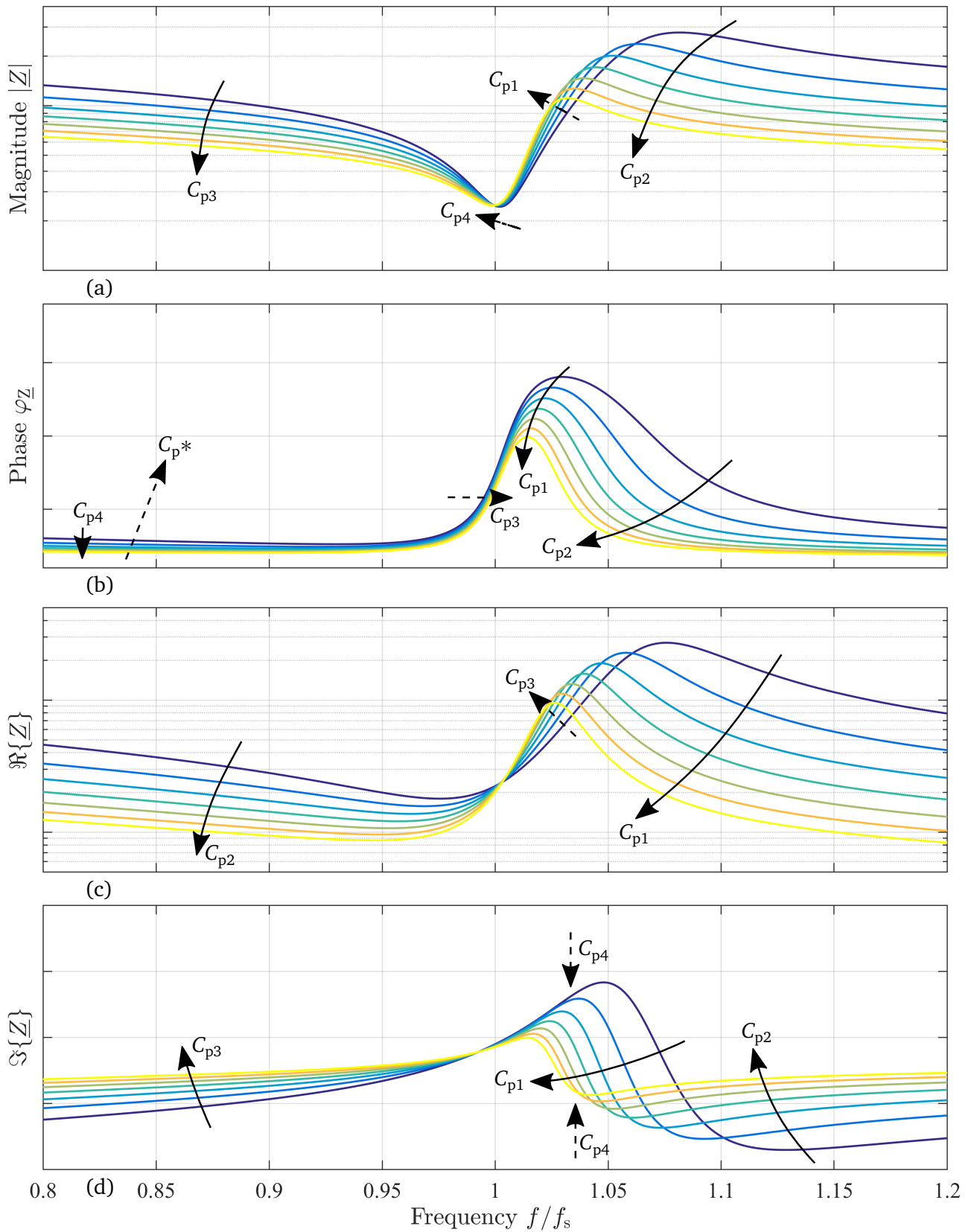


Figure 4.5: Dependency on the parallel capacitance C_p of the 7-elements extended BvD model. For the logarithmic magnitude (a), the linear phase (b), logarithmic real part (c), and linear imaginary part (d) of the complex electrical impedance \underline{Z} normalized to short circuit resonance frequency. Only C_p is varied, increasing in direction of arrow.

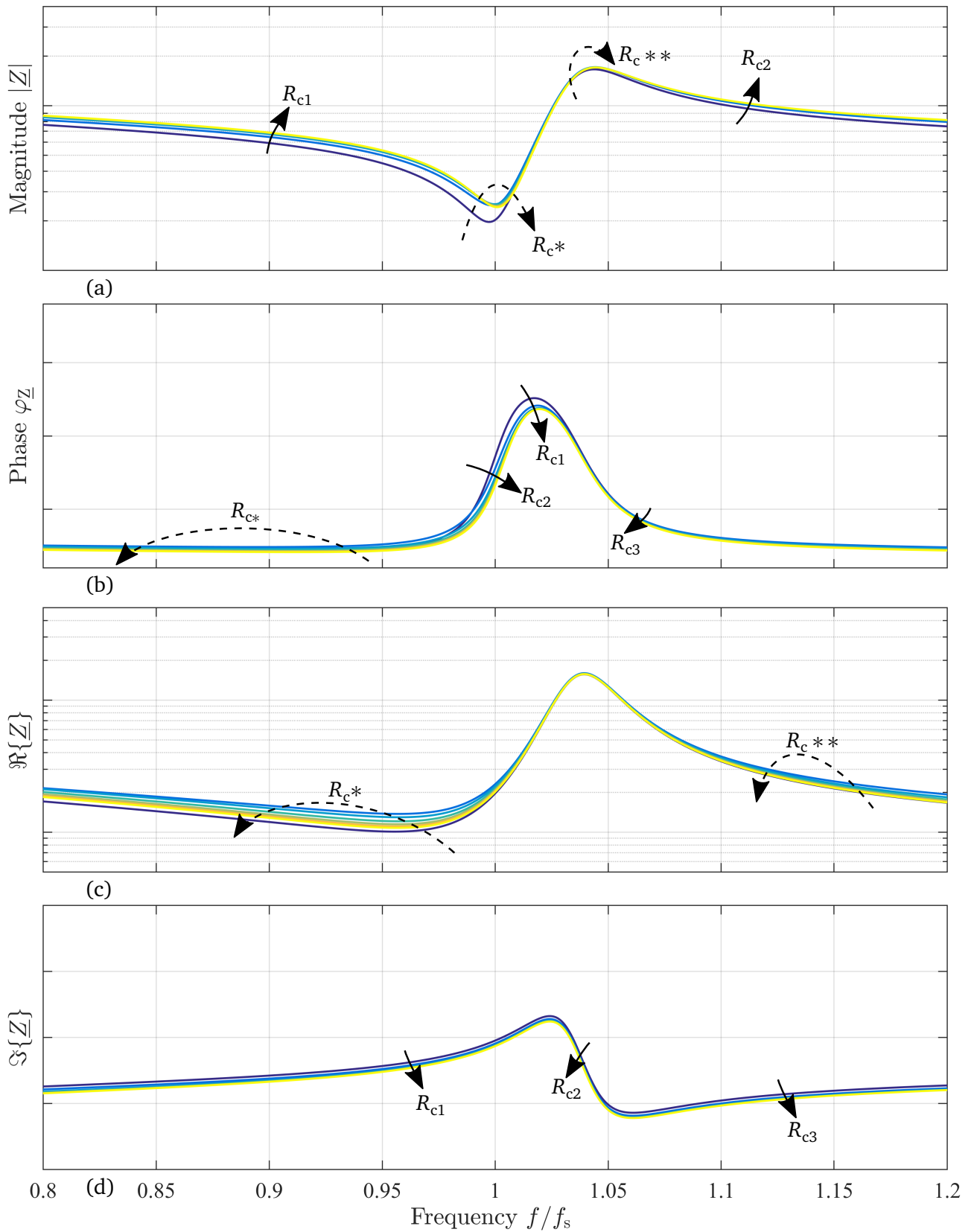


Figure 4.6: Dependency on the contact resistance R_c of the 7-elements extended BvD model. For the logarithmic magnitude (a), the linear phase (b), logarithmic real part (c), and linear imaginary part (d) of the complex electrical impedance \underline{Z} normalized to short circuit resonance frequency. Only R_c is varied, increasing in direction of arrow.

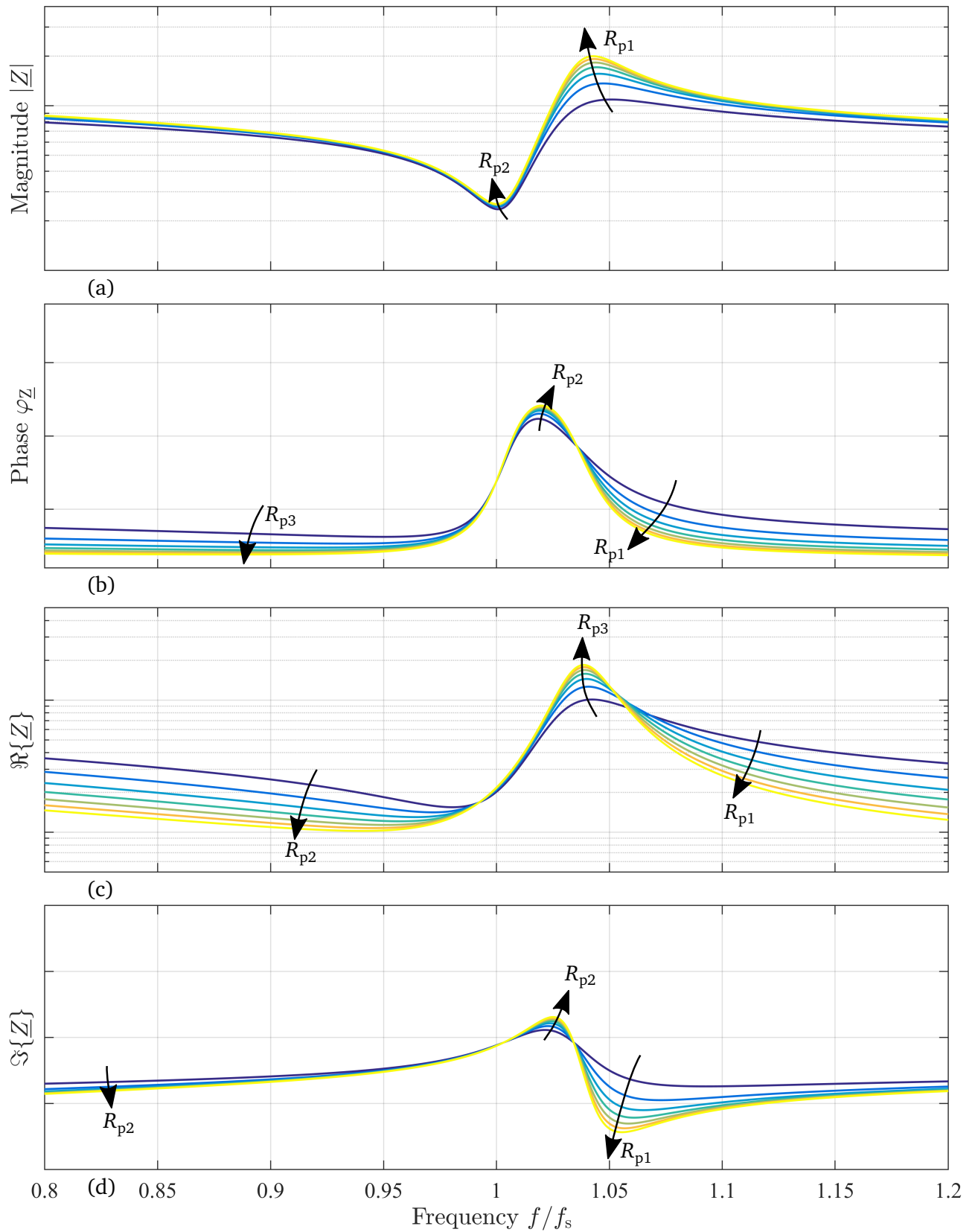


Figure 4.7: Dependency on the parallel resistance R_p of the 7-elements extended BvD model. For the logarithmic magnitude (a), the linear phase (b), logarithmic real part (c), and linear imaginary part (d) of the complex electrical impedance \underline{Z} normalized to short circuit resonance frequency. Only R_p is varied, increasing in direction of arrow.

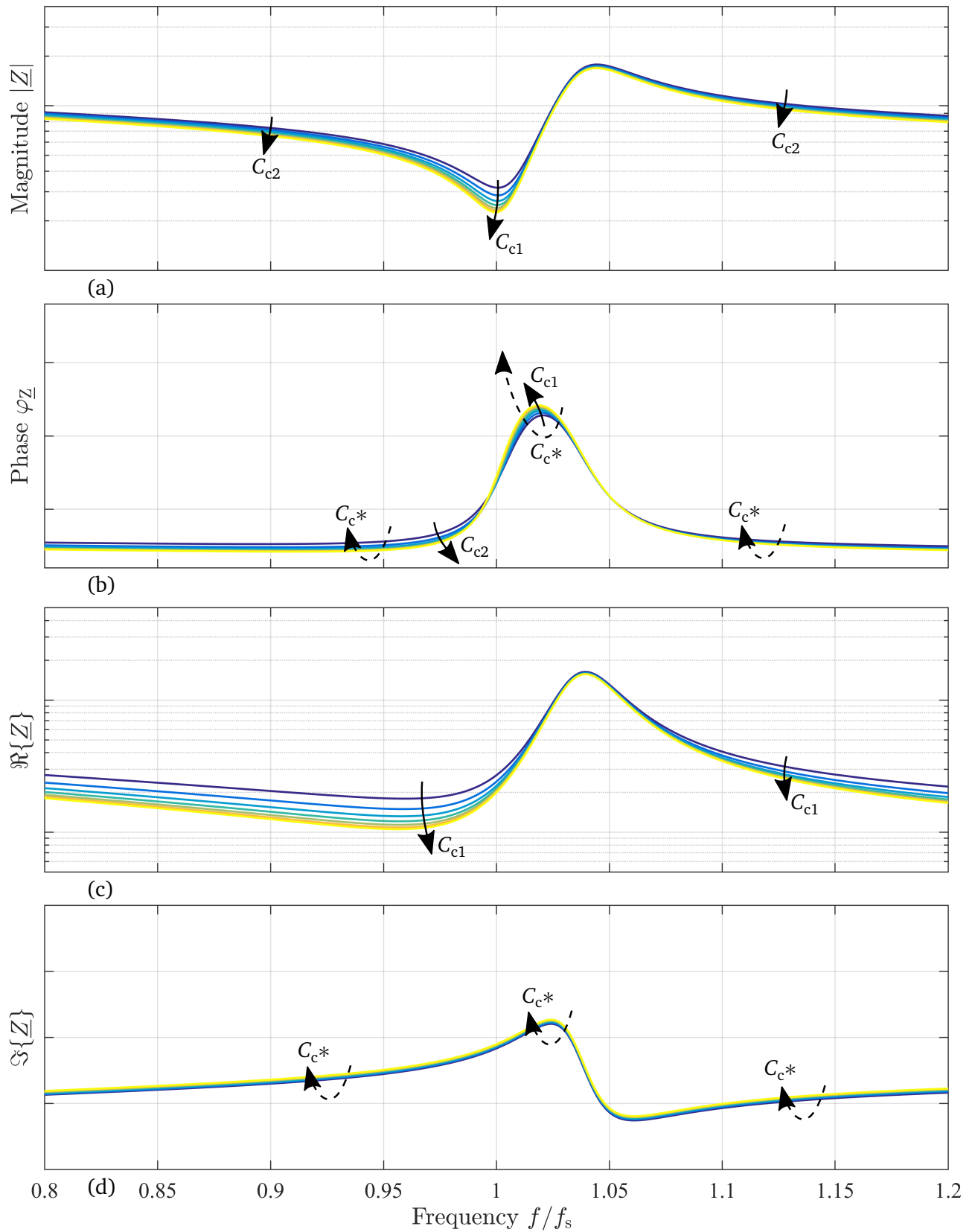


Figure 4.8: Dependency on the contact capacitance C_c of the 7-elements extended BvD model. For the logarithmic magnitude (a), the linear phase (b), logarithmic real part (c), and linear imaginary part (d) of the complex electrical impedance \underline{Z} normalized to short circuit resonance frequency. Only C_c is varied, increasing in direction of arrow.

4.3 Complex Curve Fit Algorithms

The BvD model is a common model for describing ultrasonic transducers. In its basic version, the 4-elements equivalent circuit model it consist of R_s , L_s , C_s in series and a parallel capacitance C_p (Chapter 2.3 and 4.1). Using these lumped parameter and plotting them over frequency f results in the complex impedance \underline{Z} with magnitude $|\underline{Z}|$ and phase $\varphi_{\underline{Z}}$. When measuring the electrical impedance with an impedance analyzer, network analyzer with impedance measurements option (Chapter 3.1.1), or simply with a waveform generator and oscilloscope (Chapter 3.1.2) fitting algorithms can be used to mathematically fit the BvD model to the measured data [94]. Fitting means in simple words, compare and minimize the difference between a measured set of impedance data and the BvD model by varying its parameters and therefore minimizing an objective function [99, 100]. But keeping in mind that the simplest BvD model needs four parameter to be described completely, namely R_s , L_s , C_s , C_p . This leads to a four dimensional parameter space already. Thus the complexity increases within the number of parameters [99] and therefore the overall number of evaluations.

The electrical impedance is a complex function over frequencies $\underline{Z}(\omega) = \Re\{\underline{Z}(\omega)\} + j\Im\{\underline{Z}(\omega)\}$ which consists of a real $\Re\{\underline{Z}(\omega)\}$ and an imaginary part $\Im\{\underline{Z}(\omega)\}$, thus the fit of the BvD model has to be done complex as well. However, most common fit algorithm, which are being widely used do the fit to the magnitude only, this results often in a non-optimal results of the phase [94]. In reason of that a fitting algorithm developed by M. Kupnik is used and optimized. He extended an existing easyfit algorithm, which is based on Nelder-Mead method [99, 101], to fit data in two dimensions. A complex value can be split up into its real part and imaginary part. In doing so, the impedance can be plotted as the imaginary part over the real part. Resulting in a locus done in the complex plane, the Gaussian number plane.

Knowing this fact it becomes clear that any impedance has to be fitted considering a complex fit algorithm, which is either a fit of the magnitude of the impedance and its phase at the same time or the real part and the imaginary part of the impedance at the same time. In this work MATLAB R2016b (The MathWorks®, Natick, MA, USA) is used to fit the impedance data and it is always fitted on the real and imaginary part since their dimensions are in the same order of magnitude. Other fitting algorithms are available, such as the Levenberg-Marquardt [95], which is based on the Gauß-Newton algorithm.

A second and completely different approach to fit these data is the differential evolution algorithm implemented in Mathematica 11.0.1.0 (Wolfram Research, Inc., Champaign, IL, USA) by S. Schlemmer during a student research project. The algorithm starts with a stochastically distribution of the starting values and uses the results of the objective function by weighting the results such as a population. Is the population successful so it grows and if the population is weak the population dies. Having many results of the objective function with similar values, the algorithm let them 'live' and uses this information to find new and better starting values near the latter ones. Having only a few results of the objective function with similar values, the algorithm let them 'die' and uses this information to avoid these starting values. Using the differential evolution algorithm to fit the standard BvD model with only 4-elements at the same time resulted in fitting success. However, using this algorithm to fit seven parameters of an extended BvD model at the same time the differential evolution algorithm resulted in a non-fitting result and this interesting approach needs to be further investigated. However the focus in this thesis lies on

the complex curve fit implemented in MATLAB®.

4.3.1 Finding Start Parameters

Every fit starts with initial values of the parameters. The start values are often denoted as guess values. In case of an unknown DUT, the parameters often have to be guessed, which is not ideal and results into a failing fit. Therefore, good sensible start values are a mandatory [95]. However, the more complex the model the more difficult it is to find them. In case of a 4-elements Butterworth-van Dyke (BvD) model they are calculated as follow.

First, the parallel capacitance C_p : Assuming the electrical impedance measurement is so performed, that both resonance frequencies, short and open one, are centered in the measured frequency range. Then a start value for $C_{p,guess}$ can be calculated from the imaginary part of the measured impedance by

$$X_{Cp} = \frac{1}{j\omega C_p} \quad \Rightarrow \quad C_{p,guess} = \frac{1}{2} \left(\frac{1}{2\pi f_1 \Im\{Z_1\}} + \frac{1}{2\pi f_{end} \Im\{Z_{end}\}} \right) \quad (4.1)$$

where frequency f_1 and complex impedance Z_1 are the first data points measured and f_{end} and Z_{end} are the last measured data point, X_C is the reactance of the complex impedance $X_C = \Im\{Z\}$ with the angular frequency $\omega = 2\pi f$.

Second, when $C_{p,guess}$ is calculated it can be used to obtain the next start value of the series capacitance $C_{s,guess}$ by using equation 2.11, rearranged after L_s , with

$$L_s = \frac{1}{4\pi^2 f_s^2 C_s} \quad (4.2)$$

Next put 4.2 in equation 2.12 through substituting L_s and rearranging it after C_s to

$$f_p = f_s \sqrt{1 + \frac{C_s}{C_p}} \quad \Rightarrow \quad C_{s,guess} = \left(\frac{f_o^2}{f_s^2} - 1 \right) C_{p,guess} \quad (4.3)$$

Where the short circuit resonance f_s can be found by searching for the minimum of the magnitude of the impedance, starting form the lowest frequency. Afterwards the open circuit resonance f_o can be found searching for the maximum of the magnitude of the impedance but starting from f_s . In doing so the sometimes typical higher values of magnitude of the impedance at lower frequencies, due to the overall capacitive behavior, will not be detected as open circuit resonance.

Third, after C_s is calculated it can then simply be used to get the start value of L_s by using equation 4.2. Again using the short circuit resonance frequency f_s .

Last, the start value of series resistance R_s . Assuming that at short circuit resonance the reactance $j\left(\omega_s L_s - \frac{1}{\omega_s C_s}\right)$, the imaginary part of Z_{series} , the series impedance (Equation 2.8), has to be zero

according to the conditions for resonance [53]. Then the magnitude of the impedance is left by R_s and can be obtained by searching the minimum of \underline{Z} .

Those four start or guess values of the parameters can then be fed into the easyfit algorithm. Along with criteria of tolerances and some more conditions such as the physical meaning of them, which simply says that all parameters are positive real numbers, $\{R_s, L_s, C_s, C_p\} \in \mathbb{R} > 0$.

However, the 4-elements BvD model is often not good enough to describe an ultrasonic transducer and it has to be extended (Chapter 4.1). Also for those additional elements good start values have to be found. Due to the varieties of their combination and interference or complementary properties to other existing parameters no formulas can be generalized yet, which are valid for all. Furthermore a dependence on the type of ultrasonic transducer and frequency range can be observed. In reason of that, the start values for the fifth, sixth and seventh element are guesses based on the authors experience. In addition, the dimension of the problem of the fit task, which has to be solved, raises to power of the dimension. Thus, the more parameters the less robust is the automatic fit of sets of data. In order to investigate those issues the values of the parameters were monitored (Chapter 4.3.2). But not only finding good start parameter is an issue, beforehand a proper extension of the BvD has to be found as well.

4.3.2 Monitoring of the Fit Parameters

Having multiple fit parameter based on the used type of BvD model, the robustness of a fit is in general reduced the more elements are being used. Here the algorithm can get stuck in a local minimum rather than finding the global minimum and exiting the fit at the limit of iterations. Thus, increasing the allowed total iterations does increase the overall time consumption and does not lead to a successful fit result. Also the standard built in options for further investigation are limited to only a few such as plotting the value of the objective function or the function itself [100]. Therefore the easyfit algorithm was extended by the author to gather the values of the parameters at each step of iteration. Since the amount of parameters is depending on the used BvD model (Chapter 4.1) the model function itself was utilized to obtain the internal parameter values. Furthermore, at every iteration it is called by the easyfit algorithm. Hence, the model function itself was modified by storing each individual parameter of the BvD model in addition to the iteration count in a global defined matrix. In doing so, the individual values of the parameters can be accessed later after the fit for further post processing and analyzing.

So it was possible to visualize each step of iteration by plotting any of these seven parameters at any given iteration step. This method opens an opportunity to analyze for example non fitting results or bad fits. Since the seven parameter ranging from small (e.g. pF) to big (e.g. MΩ) over multiple orders of magnitudes the parameter were plotted in a normalized manner. So each parameter value P is normalized to its maximum and to its minimum at the same time by

$$P_{\text{norm}} = \frac{P - P_{\text{min}}}{P_{\text{max}} - P_{\text{min}}}. \quad (4.4)$$

Therefore the ordinate is limited from 0 to 1.

During a bad fit, for example, it can be clearly seen that some of the seven parameters running into their lower limits of zero each, R_s , L_s , and C_c (Figure 4.9). Because negative values are not allowed due to the absence of any physical meaning. Whereas parameter C_s , R_p , C_p , and R_c running into bigger values. Here, after a total of 15,000 iterations, the algorithm was stopped by the criteria of maximum iteration. Also increasing simply the limit of this criteria or changing the alternation rate of each value did not helped to solve this issue. This is only one example of a bad fit.

In other cases when the values look good, the algorithm can get stuck in a local minima as well. Here some of the seven parameters, resulting in sensible values [Figure 4.11 C_c , C_p , and R_s] whereas other parameters R_p and L_s again get stuck at low values [Figure 4.11] and the fit was not aborted by the maximum iteration criterion.

This often happens with wrong or bad start values i.e., thus, bad guesses. So there start values are either to big or to small and they obviously are to far off from the real parameter values, which are not known up front. Also, looking only at the parameters after the fit alone is not enough to find criteria for more robustness or a good fit. Therefore using a wrong type of model and the complex curve fit algorithm can fail as well.

For further investigations, a small program in LabVIEW™ (32-Bit, 2016 Fall) was written. It enables the input of measurement data for a direct comparison with the selected BvD model. Thereby for example, the seven parameters R_s , L_s , C_s , C_p , R_c , R_p , and C_c can be manipulate manually simply by using sliders or by direct input of their values (Figure 4.10). In real time is then the magnitude of $|Z|$, the phase φ_Z , the real part $\Re\{Z\}$, and the imaginary part $\Im\{Z\}$ calculated and visualized (Figure 4.10). In addition, for the sake of completeness on the complex plane, $\Re\{Z\}$ and $\Im\{Z\}$ are visualized (Figure 4.10) as well. Here they result in a locus, due to the two resonance frequencies, i.e. short and open circuit resonance. Literally playing around with this tool, the influence of each parameter was studied.

As mentioned before, a proper model is a key part to a successful fit. Analyzing with this tool therewith a new or unknown device as a first step, the correct or better model can be obtained. Simply by looking at the influence of these parameters and how these affect the behavior of those curves. Of course for this purpose, the program can be extended to the proper need of the different BvD models.

When the model is found, the starting values were obtained (Chapter 4.3.1) and the fit always is started with a dataset that has the most pronounced magnitude of the impedance and phase which is in a case of a CMUT the one with the highest DC-bias voltage (Figure 4.12 $14V_{DC}$). Due to equation 2.4 its force is at maximum and therewith its efficiency.

After the fit for the highest DC-bias voltage is done, the result values of the seven parameter are being used as the new starting values for the next data set with a lower DC-bias voltage. Usually the electrical impedance is shifted only by a small fraction, so that the complex curve fit algorithm is robust enough to find the next fit. In doing so the complex fit algorithm and therewith the automatic parameter extraction can successively run through large sets of data. Although in this example the device suffers from some distortion the complex curve fit algorithm is robust enough to deliver a proper fit result for the magnitude of the electrical impedance [Figure 4.12 (a)] and its phase [Figure 4.12 (b)]. Then all parameters can be visualized in dependence on the bias voltage (Figure 4.13), temperature, or excitation voltage.

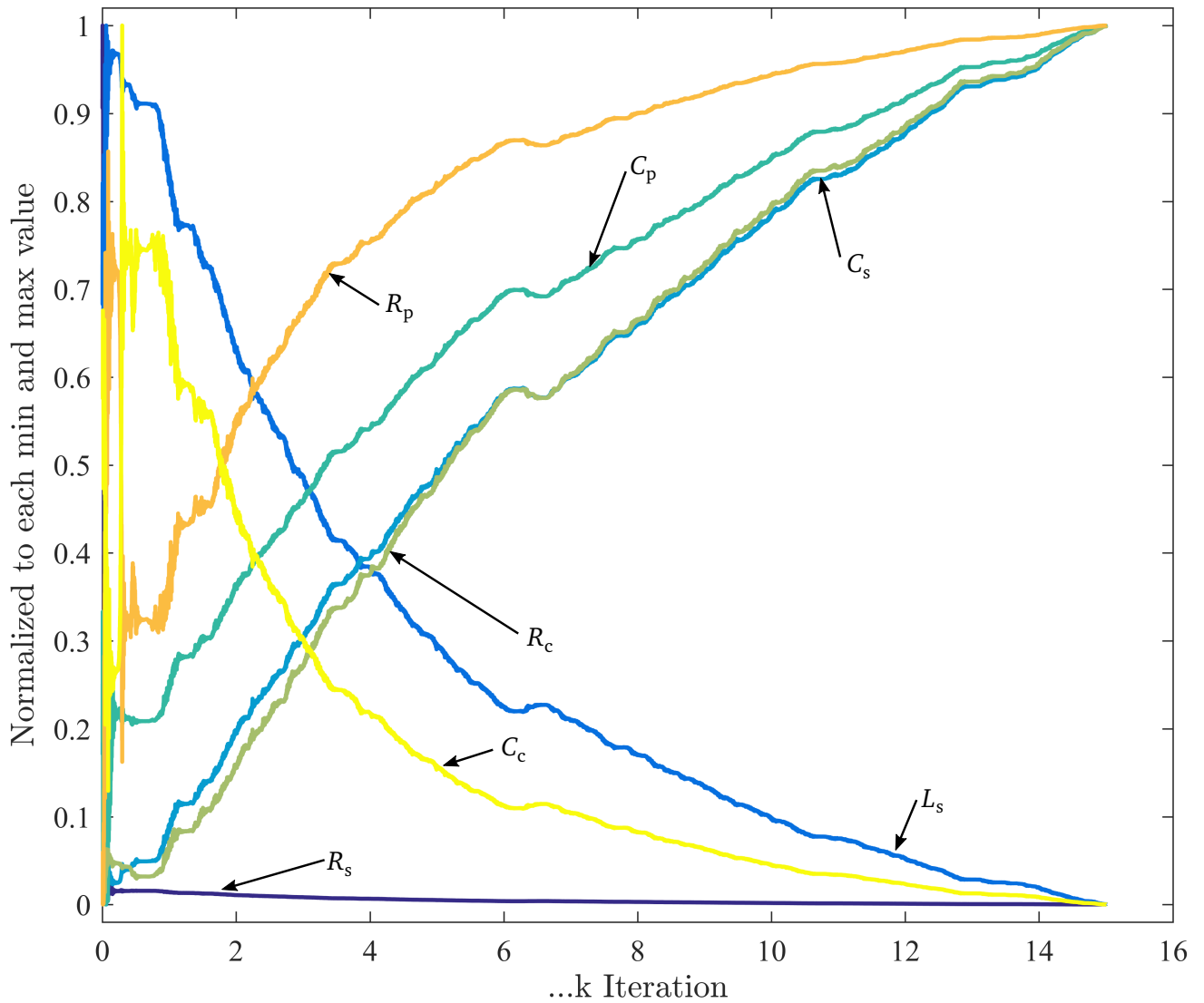


Figure 4.9: Monitoring of all seven fit parameters, the series resistance R_s , series inductance L_s , series capacitance C_s , parallel capacitance C_p , contact resistance R_c , parallel resistance R_p , and contact capacitance C_c over each iteration of a complete non successful fit of one set of electrical impedance data. Here the fit was not successful, the algorithm got stuck in a local minima and therefore a typical trend to their maximum or minimum of each value can be observed and the fit was terminated by its maximum iteration of 15,000. Values are normalized to their individual minimum and maximum.

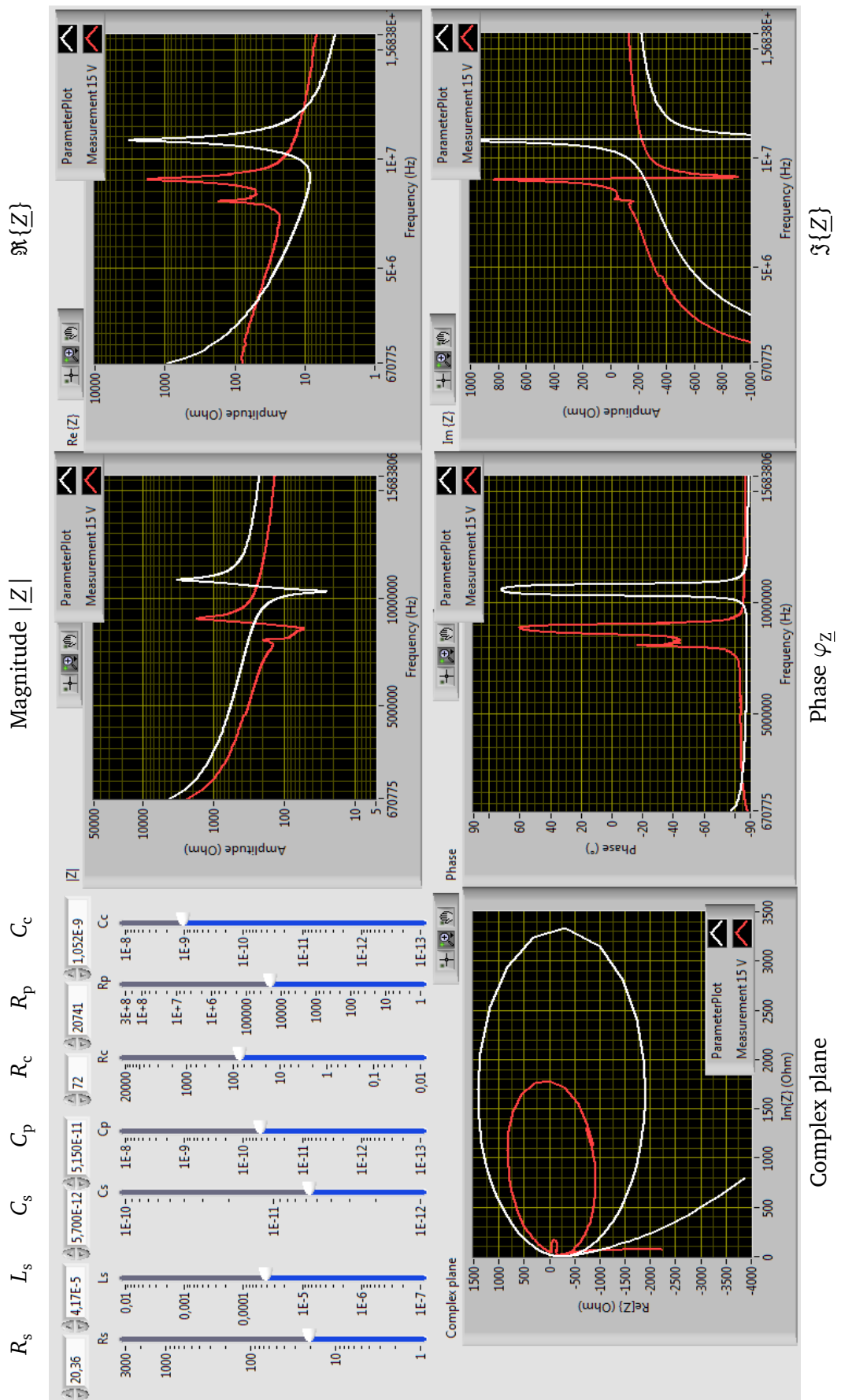


Figure 4.10: A LabVIEW™ program for visualizing the influence of the seven parameters of the extended BvD model [Figure 4.1 (e)] individually, calculated and plotted in real time.

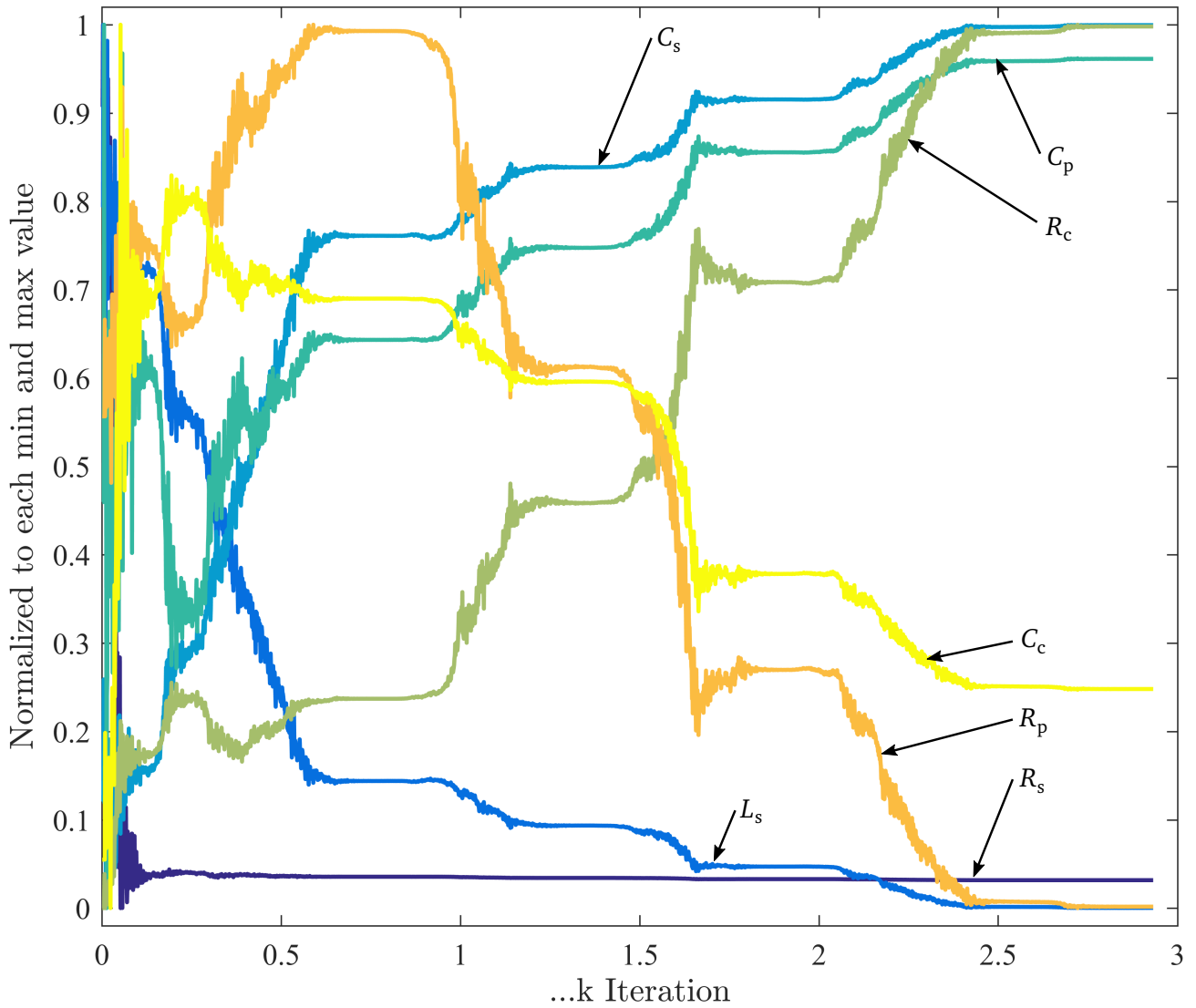


Figure 4.11: Monitoring of all seven fit parameters, the series resistance R_s , series inductance L_s , series capacitance C_s , parallel capacitance C_p , contact resistance R_c , parallel resistance R_p , and contact capacitance C_c over each iteration of a complete successful fit of one set of electrical impedance data. Values are normalized to their individual minimum and maximum.

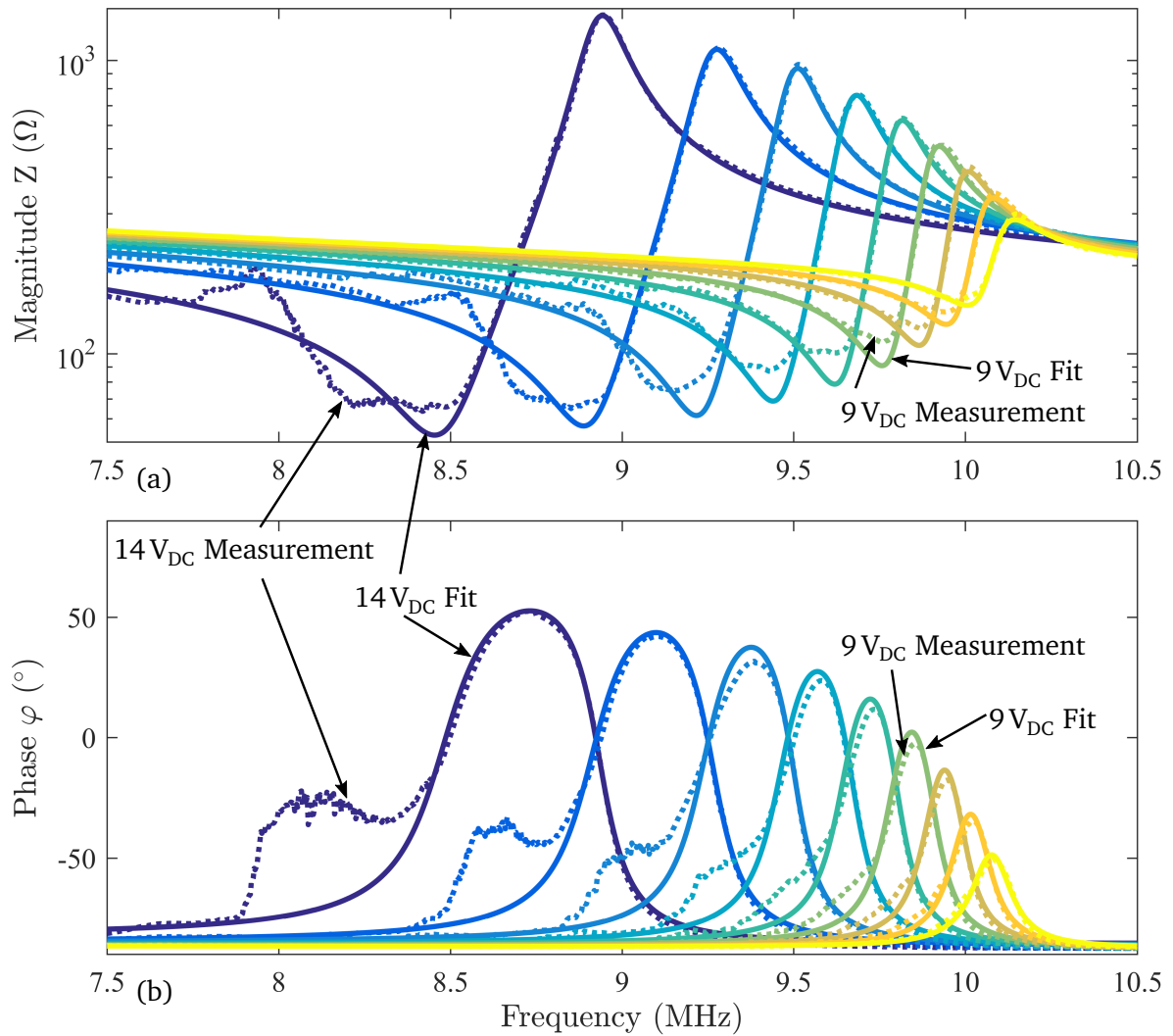


Figure 4.12: Fit results of a 8.5 MHz CMUT measured at a DC bias voltage range from $6V_{DC}$ to $14V_{DC}$ in magnitude (a) and phase (b) of the complex electrical impedance \underline{Z} . Although the device suffers from some distortion the complex curve fit algorithm is able to find a good looking fit result.

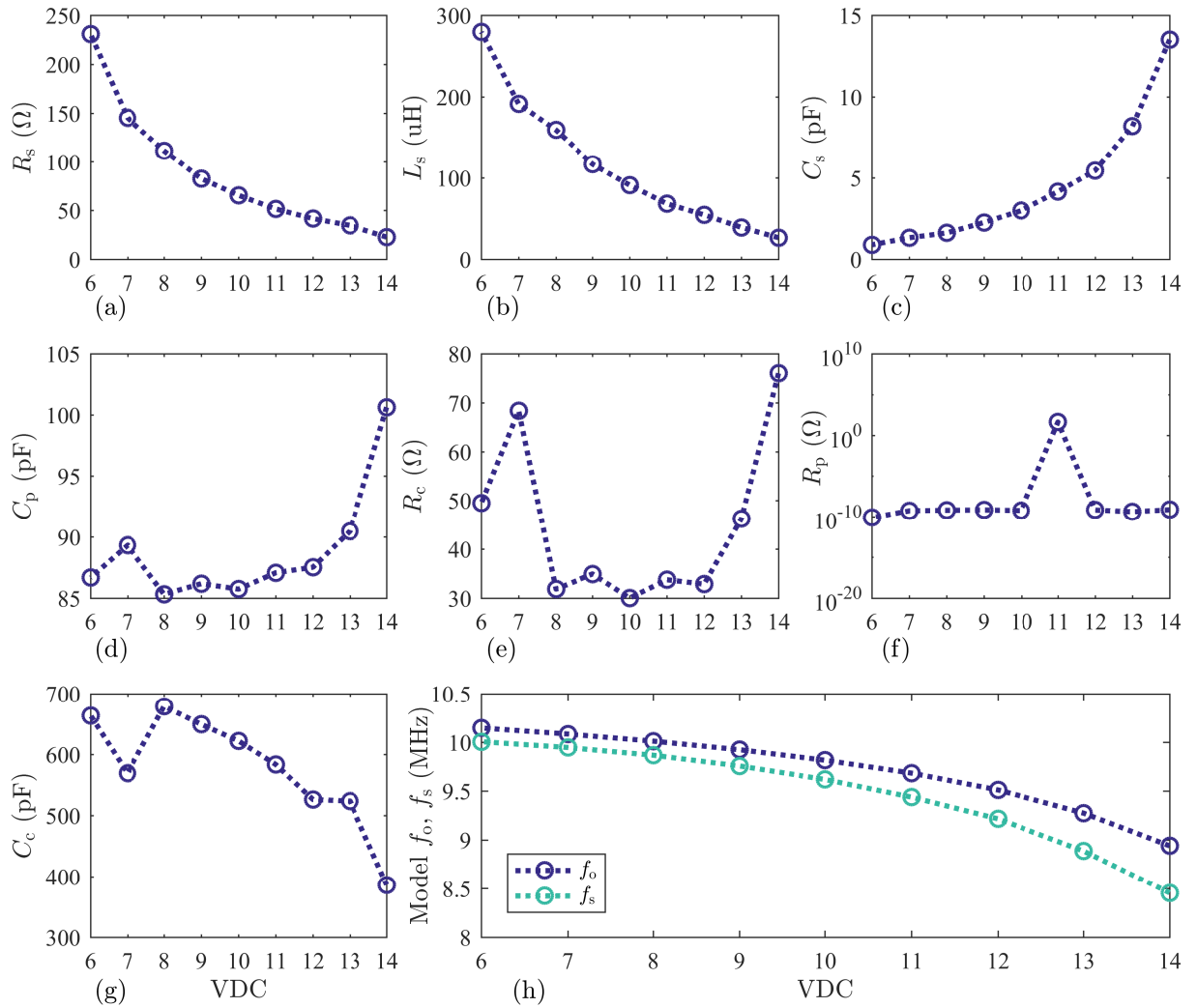


Figure 4.13: Parameter overview of a 8.5 MHz CMUT fit result measured with a DC bias voltage range from $6 V_{DC}$ to $14 V_{DC}$. With fitted values of series resistance R_s (a), series inductance L_s (b), series capacitance C_s (c), parallel capacitance C_p (d), contact resistance R_c (e), parallel resistance R_p (f), contact capacitance C_c (g), and short and open circuit frequencies obtained from the 7-elements BvD model (h) after the fit. Although in this run the fitting algorithm was not able to find valid values for the parallel resistance R_p (f).

5 Waveguides an Approach of Separation of the Acoustic Aperture

Parts of this chapter have been published already in [5].

In this chapter an approach of the separation of the actual vibrating structure from the acoustic aperture is introduced. As discussed in chapter 2.4 the separation offers many advantages in several technical fields and is utilized in nature. So the array features a simple fabrication technique using shrinking tubes for the intended separation. Measurement in transmit and as well receive mode prove the increase of performance.

Using ultrasound at a low frequency in air at a range of (20 – 500) kHz is often desirable in many real world applications. Applications such as gesture sensing, tactile display, haptic hologram, range finding, acoustic imaging of entire rooms, anemometry, directed ultrasonic communication, acoustic tweezing in air, and gas flow metering for example. Such low frequencies have the benefit of a low attenuation, which leads then of course to a bigger range of operation. However, only transmitting or receiving ultrasound at such low frequencies in air is not sufficient enough for certain sensory applications.

For example, usage in a single path ultrasonic gas flow meter (UFM). Here the entire transducer ports cavities are often tilted and shifted to an optimum, but fixed and static, position [102]. This increases the operating range from near zero gas flow to higher velocity flows. However, at higher gas flow velocities, the ultrasonic beam tends to drift due to the flow velocity of the media and the signal to noise ratio (SNR) is therefore reduced. For further improvement an adaptive asymmetric double path UFM is able to shift the ports during operation. So an optimum SNR depending on the gas flow velocity can be achieved [103]. However, a simpler solution is desirable and would be more practical for implementation in many real world applications.

Also in tactile displays, the sensible force is often too weak for the subject to feel it. Especially for recognizing a constant force input is needed [104]. Even in haptic holograms the spatial resolution often is not sufficient and undulated patterns, disturbing the hologram, thus, spoiling the overall tactile experience [105]. Here grating lobes are one of the limiting factors of such acoustic imaging in air [106]. Grating lobes result in a reduced field of view (FOV) and can cause trouble due to ghost objects. They are created due to the periodical pitch being more than the required half wavelength distance [16, 24, 25].

It is well known that an element pitch of at least half wavelength is needed to build a phased array, which can steer a beam without any significant grating lobes [16]. A huge drawback of these grating lobes is that they use a significant amount of the available total energy. Furthermore, they can disturb the performance and limit the operating range due to possible ambiguities. As far as the author knows the smallest commercially available ultrasonic transducers at 40 kHz in air, which can easily and efficiently transmit and receive signals in good quality are 10 mm in diameter. However, using those for the needed pitch of 4.3 mm, which half wavelength at 40 kHz, cannot be achieved.

Using micromachined ultrasonic transducers (CMUTs) to fulfill this half wavelength criteria is also not an easy task. For example, a circular shaped wafer bonded single cell CMUT, with a 40 μm -thick silicon plate, can barely be brought down to smaller than 45 kHz [107, 108]. Cause the plate diameter has to be limited to about 4 mm, which then leaves enough space for a sufficient bonding area at element pitch of 4.3 mm. Further thinning down the plate thickness does not work either due to non-linear geometry effects. Stress stiffening, results in an increasing resonance frequency again [108]. In addition, the initial setup cost associated with a micromachined sensor fabrication is to prohibitive.

However, phased arrays with the ability to beam forming at low ultrasonic frequencies would consequently be the next step to achieve better resolution, accuracy and overall performance. As already mentioned, performing beam forming without any significant grating lobes would be an ideal solution and this leads inevitably to the half wavelength pitch requirement. Therefore, ultrasonic channels were investigated for the use in e.g. robotic industry by [24] (Chapter 2.4). This work offers several basic approaches for the construction of ultrasonic transducer channels in front of a Helmholtz Resonator with a specialized aperture. Thereby a focused ultrasonic sensor with a wide range up to 20 m and a narrow acquisition angle can be built. Also, the suppression of side lobes is shown by an array transducer with acoustic channels [24]. Another approach is to use sound tubes [25] to decrease the pitch in transmit mode at 40 kHz to the half wavelength criteria of 4.3 mm in air.

The author shows one solution by combining these earlier approaches by using sound tubes and extending them into both transmit and receive mode with the capability of beam forming without any significant grating lobes.

5.1 Fabrication of the Phased Array utilizing Waveguides

The prototype of a 1D phased array (Figure 5.1) is fabricated with 8 x 12 commercially available 40 kHz ultrasonic transducers MA40S4S (Murata Manufacturing Co. Ltd., Kyoto, Japan)5.1. On top of them 96 tapered waveguides to achieve the half wavelength pitch. Resulting in an eight channel 1D phased array. Whereby, each channel features twelve in parallel connected ultrasonic transducers for 50Ω electrical impedance matching on the one hand and a bigger acoustic aperture in total of $(34.4 \times 79.2)\text{mm}^2$ on the other hand. The waveguides were made of shrinking tubes with a diameter of 10 mm. They have a total length of 67.1 mm each. Those then were shrunk by means of a specially designed mold made out of aluminum [Figure 5.2 (b)]

With this approach it was possible to reduce the circular shape opening of the Murata MA40S4S ultrasonic transducer with a diameter of 10 mm down to a rectangular shaped opening of $(3 \times 4.8\text{mm})$ [Figure 5.2 (a)]. Due to their shrinking behavior of 2:1 it is not possible to get a smaller opening without any additional processing (cutting or removing material). However, the half wavelength pitch of 4.3 mm in one direction can be achieved. In doing so, intentionally the separation of the active acoustic aperture from the actual ultrasonic transducers radiating aperture was achieved (Figure 5.3). Furthermore, the acoustic energy emitted becomes concentrated through the waveguides at the smaller aperture.

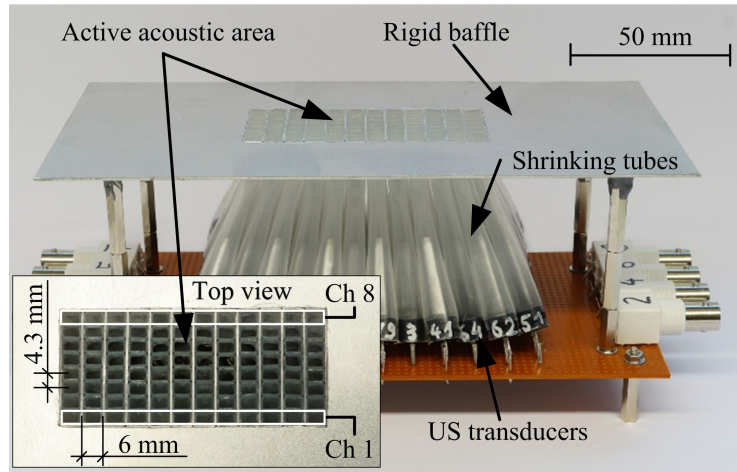


Figure 5.1: Prototype of a versatile 40kHz 1D phased array made of 96 Murata MA40S4S ultrasonic transducers featuring separated effective acoustic aperture (insert) by using shrinking tubes [5].

Table 5.1: Main characteristics of a Murata MA40S4S ultrasonic transducer[29].

Characteristics	Values
Part number	MA40S4S
Construction	Open structure type
Nominal frequency	40 kHz
Sensitivity	(-63 ± 3) dB
Sound pressure	(120 ± 3) dB
Max input voltage (square wave)	$20V_{pp}$ continuous signal
Directivity	80°
Operating temperature range	$(-40 - +85)^\circ\text{C}$
Dimension ($\text{\O} \times h$)	$(9.9 \pm 0.3 \times 7.1 \pm 0.3)\text{mm}$

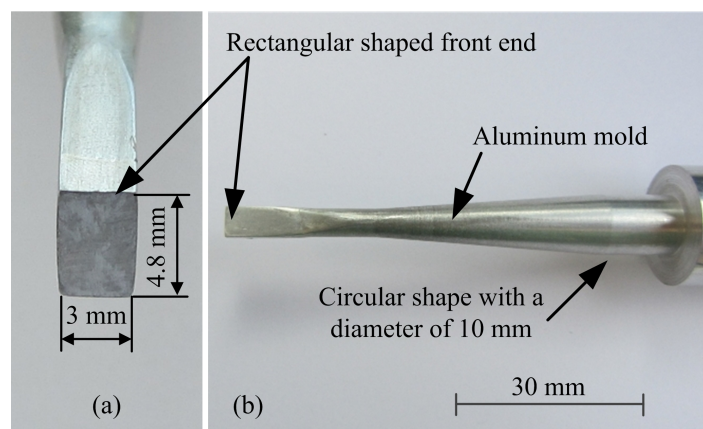


Figure 5.2: Mold (b) made of aluminum used to shrink the waveguide tubes from 10 mm in diameter circular shape down to a rectangular (3×4.8 mm aperture) (a) [5].

5.2 First Characterization Measurements

All measurements were conducted in a standard laboratory environment using a 3D stage [14], which is capable of measuring 1 m^3 in front of the 1D phase array, at ambient temperature and ambient pressure of one atmosphere. To avoid standing waves and to minimize reflections all measurements are taken with burst signals only and using expectation time windows to gather the data.

5.2.1 Transmit Mode

To drive the 1D phase array five waveform generators (four slaves and one master) of type Keysight 33522B (Keysight Technologies, Santa Clara, CA, USA) were used to control the beam steering in transmit mode (Figure 5.4). They were all synchronized by the same time base reference clock of 10 MHz. The four slave generators using two channels each for eight channels in total. Each of them was generating a true time delay (TTD). The master wave form generator provides a synchronized trigger to all four slaves, which were triggered externally. The waveform generators were initialized and then controlled via LabVIEW™ (National Instrument, Austin, TX, USA) program. Using this program the time delay, which required to achieve a given beam angle value, is calculated with the following equation [5]:

$$t = \left| \sin(\alpha_b) \frac{(N-1)d}{2c} \right| + \sin(\alpha_b) \left(n - \frac{N-1}{2} \right) \frac{d}{c}, \quad (5.1)$$

where α_b is the destination angle of the beam, c is the speed of sound at ambient temperature, with d as the pitch, N is the total number of channels and n is index of the actual channel starting with $n = 0, 1, 2, \dots, N-1$. Each of these four slave waveform generators generates then a 40 kHz sinusoidal burst signal with 80 cycles and $20 V_{pp}$ amplitude to excite the twelve ultrasonic transducers of each channel, which is shifted by the time delay, calculated by (Equation 5.1).

A calibrated 1/8 inch B&K 4138-A015 microphone combination (B&K, Skodsborgvej, Denmark) measured the sound pressure level (SPL) in front of the phased array (Figure 5.4) along a half circle with a radius of 35 cm using a 3D stage [14]. Hence, the directivity pattern are measured along this half circle from -90° to $+90^\circ$ in 0.2° steps. This 3D stage also is used to perform volumetric measurements covering 1 m^3 , thus the steered beam characteristics can be visualized in 3D.

5.2.2 Receive mode

In receive mode, two 4 channel oscilloscopes of type Keysight DSO-X 3024A (Keysight Technologies, Santa Clara, CA, USA) were used to obtain the waveform data, the so called A-scans of each of the eight channels. Thereby the phased array was rotated $\pm 90^\circ$ relative to an ultrasonic emitter in front of it using a rotation stage (8MR190-2-28, Standa Ltd., Vilnius, Lithuania). As an emitter, a parametric array with a big aperture size of 180 mm [92] in diameter is used, thus the emitted ultrasonic wave is almost a planar wave [Figure 3.18 (a), Chapter 3.4.2]. The parametric array consists of 222 parallel connected Murata

MA40S4S ultrasonic transducer of the same type and is mounted 1.5 m away facing to the 1D phased array. Again a 40 kHz sinusoidal burst signal with 80 cycles and $20V_{pp}$ excitation voltage is applied to this emitter using an amplifier Dynacord SL1200 (Dynacord GmbH (Bosch), Straubing, Bavaria, Germany). For post processing of the gathered A-scans MATLAB®R2014b (The MathWorks Inc., Natick, MA, USA) was used. Here a simple beam forming algorithm (delay-and-sum beam former [109, 110]) was applied to steer the receive sensitivity.

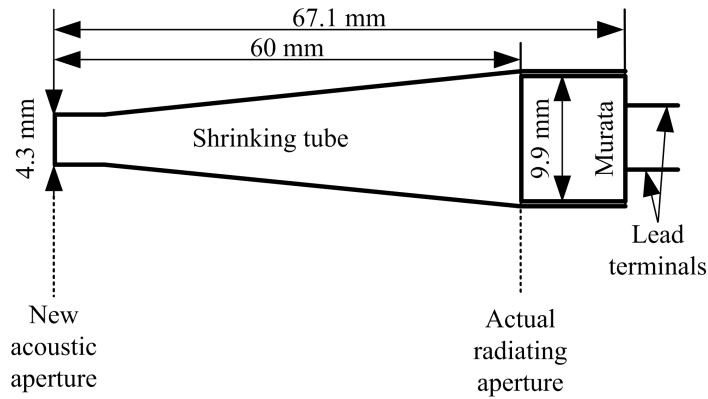


Figure 5.3: Schematic of a waveguide including a Murata ultrasonic transducer. Where the shrinking tube acts as a part of the smart packaging layer and thus separates the acoustic aperture from the actual radiating aperture [5].

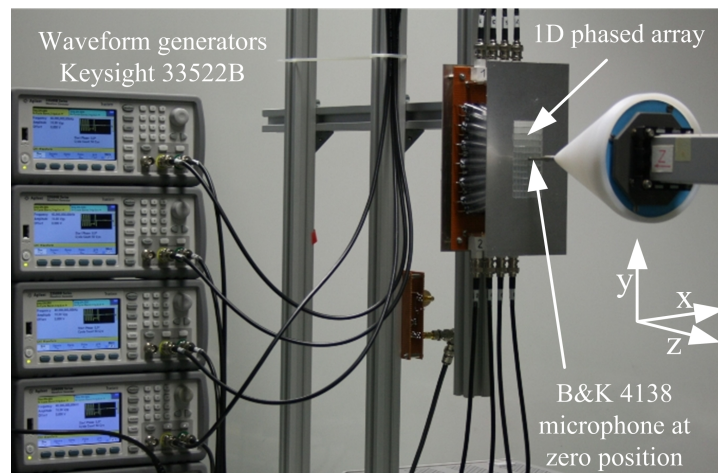


Figure 5.4: Experimental setup used for characterizing the performance of the 1D phased array transducer with a calibrated B&K 4138-A015 microphone combination [5].

5.3 Results and Conclusions

This 1D phased array prototype can be steered over a wide range of 110° in total, $\pm 55^\circ$ in each direction, without any significant grating lobes. A sound pressure distribution at an exemplary angle of -35° shows that no significant grating lobes are present (Figure 5.5). In transmit mode, an impressive sound pressure level of (130 ± 1) dB is measured at a distance of 1 m while operating at a frequency of 40 kHz in air. The directivity pattern shows the same behavior as theory at half wavelength pitch predicts [Figure 5.6 (a)]. In receive mode, the main lobe gives the highest sensitivity and no significant grating lobes are present as well [Figure 5.6 (b)]. The prototype 1D phase array is capable of receiving directed ultrasound with

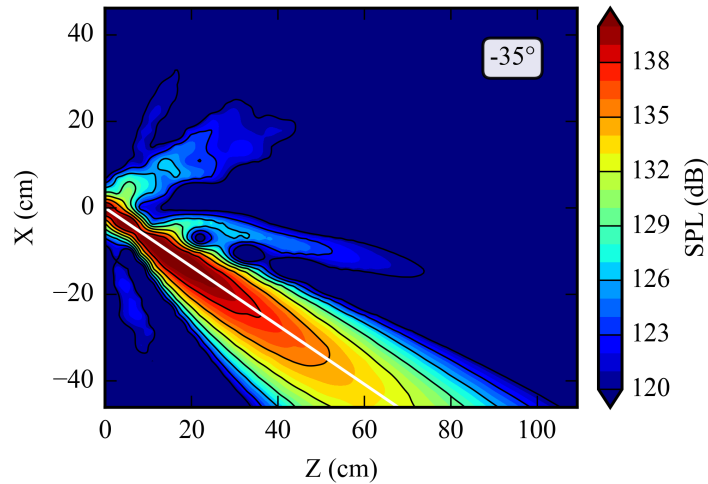


Figure 5.5: Cross section through volumetric measurement of the sound pressure distribution of a transmitted main lobe, whereby the beam is steered at an angle of -35° , the white line indicates the target angle. Note that no significant grating or side lobes are observed [5].

a sensitivity of -55.9 dB with 0 dB is equal to 1 V/Pa. Also the opening angle of the 1D phased array in receive mode is in total approximately 110° as well, due to reciprocity.

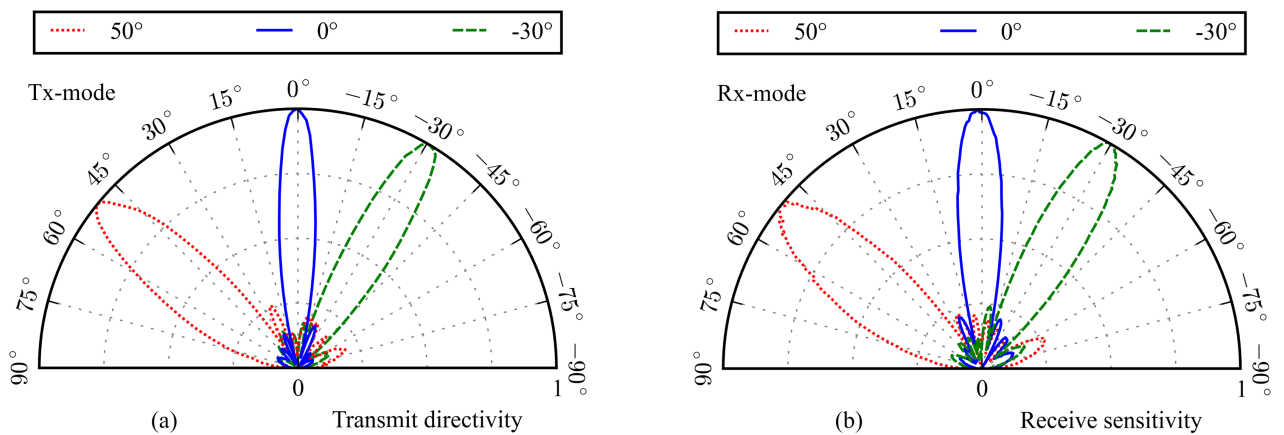


Figure 5.6: Measured transmit beam directivity patterns (a) of the 1D phased array transducer along a half circle in front of it, with e.g. beam steering of an angle of 50° , 0° , -30° and measurements results of the sensitivity patterns of our 1D phased array transducer in receive mode (b) by listening electronically again at 50° , 0° , -30° [5].

In the end it is a successful fabricated versatile 1D air coupled phased array operating at 40 kHz with a half wavelength pitch of 4.3 mm at the effective acoustic aperture. By adding such a smart packaging layer fabricated with many tapered waveguides, the intentional separation of the active acoustic aperture from the actual radiating aperture of the ultrasonic transducers was achieved. In doing so, the energy of each ultrasonic transducer is concentrated into a smaller aperture, which increases the overall SNR.

Such waveguide approach opens the door to many industrial applications, for example: First, in ultrasonic gas flow meters the ultrasonic beam can be adapted and steered to compensate for any flow velocity and profile variants easily, as already showed in [1]. Second, haptic feedback systems could

benefit from focusing capability of these new type of arrays. Third, without grating lobes the acoustic imaging in air will achieve wider FOV [111]. The smart packaging layer here made of shrinking tube was in the meantime successfully further developed and is printed with additive manufacturing methods (3D printing), also the phased array is now already a fully populated 2D phased array with proprietary electronics, which is a huge step forward for the usage in industrial application [2].

6 Mechanical Amplification of CMUT

Parts of this chapter have been published already in [15].

This chapter introduces an idea of a mechanically amplified capacitive micromachined ultrasonic transducer [15]. The mechanical amplification is already used at Muratas MA40S4x piezoelectric ultrasonic transducers (Chapter 2.2.1). Measurements of a MA40S4S sender with and without the aluminum horn structure (Figure 6.1) using a calibrated microphone B&K 1/8" 4138-A-015 (Brüel & Kjær, Nærum, Denmark) results in 30% higher sound pressure level (SPL) at 30 cm distance. Before fabricating and manipulating a CMUT with a horn, a finite element analysis (FEA) was performed by the author to show the feasibility. Finally measurements before and after gluing the horn were conducted for a validation of the FEA.

Looking into the literature several efforts of improvement of CMUT can be found. Main goals are often to increase the average displacement of the plate. To achieve this a non-uniform plate shape can be beneficial. Although it requires more effort to fabricate such complex structures. A CMUT featuring a plate with a piston shape was first introduced by [112] and Eccardt2000. In those work, however, for the piston shape it is needed to open up the top layers, to release the structure, with a standard CMOS-based fabrication process. The first intentionally designed piston-shaped for micromachined microphones made of silicon nitride plates using sacrificial release process have been introduced by [113]. Also [114, 115, 116] fabricated using the sacrificial release fabrication method as well. A direct wafer bonding process was used by [117] to realize CMUTs featuring piston-shaped plates. Where the pistons are facing down towards the gap. In [118] this fabrication process was further simplification by etching the pistons out of the front side of the plate. This was achieved by using two buried oxide layer (BOX) with a double silicon-on-insulator (SOI) wafer. All of these introduced approaches have in common that the non-uniformity of the plate was fabricated with micro machining techniques.

In this work, the author focus on single-cell air-coupled CMUT [15]. Ranging from 20 kHz to 150 kHz frequency range. The main idea is to add a lightweight hollow conical-shaped structure (a horn, a conical vibrator or mechanical amplifier), on top of the plate of a wafer-bonded single cell CMUT [Figure 6.1 (a)]. Whereby the main objective is the improvement of both the transmit and the receive sensitivity by increasing the average displacement of the plate, which means lowering the center-to-average displacement ratio. Here the horn is hollow and, thus, the modal mass does not increase as much as it would does for a solid piston-shaped plate. In addition, the structure is beneficial because in receive mode the force due to the impinging sound pressure wave is concentrated to the center of the plate, resulting in larger receive signals [15, 26]. Like it is achieved for commercially available piezoelectric-based bending plate devices [Figures 2.3 and 6.1 (b)]. Here the horn is not fabricated by means of micromachining techniques, it is probably simply punched out of aluminum sheet. The geometry of an already fabricated single cell CMUT [120] is our starting point for the author in this work. For a first step such CMUT will be investigated in transmit mode only.

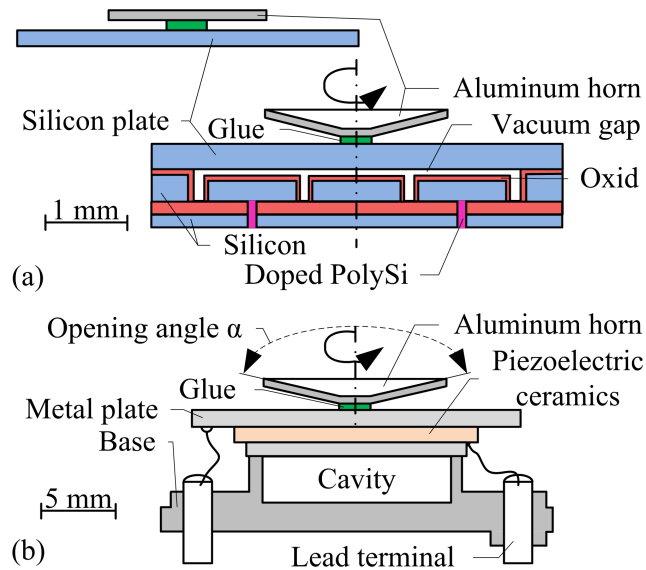


Figure 6.1: Schematic of a circular single-cell air-coupled CMUT with an aluminum horn glued on top of the plate (a) and a sketch of a piezoelectric ultrasonic transducer (b) [29, 26]. At both devices the horn has an opening angle $\alpha = 156^\circ$. As an idea a “horn” with an opening angle of $\alpha = 180^\circ$ could be fabricated with micromachining techniques as showed in [119] inlet top left (a) [15].

6.1 The Finite Element Model

The author uses an axially symmetric 2D finite element model (ANSYS, v14, Ansys Inc., Canonsburg, PA, USA) of the single cell CMUT modified with a horn made out of aluminum (Figure 6.2). Between the horn and the circular shaped single crystal silicon plate a layer of glue was added. From various gluing tests on glass plates and aluminum plates the author estimates the total area of the glue, which explains the overlap between the contact area of the horn and the glue layer in the model (Figure 6.2). The CMUT is assumed in a rigid baffle and Fluid29 elements are used to model the surrounding air. Those are meshed in a quarter-circle with an absorbing boundary with sufficient distance from the vibrating structure and with proper fluid-structure modifications [121]. The lumped transducer elements Trans126 [121] are used to apply the electrostatic force to the plate. The plate is $55 \mu\text{m}$ thick and has a diameter of 4 mm. Thus, the 300 nm thick aluminum electrode on top of the silicon plate can be neglected for this large device. The gap of this device is $12.58 \mu\text{m}$, which results in a pull-in voltage of about 225 V. Without the horn the device is operating at around 55 kHz. This CMUT has an electrically floating bottom electrode [120], which is marked with the dashed group of Trans126 [121] elements (Figure 6.2). This group in the center acts as a contact target pair only and is electrically not active.

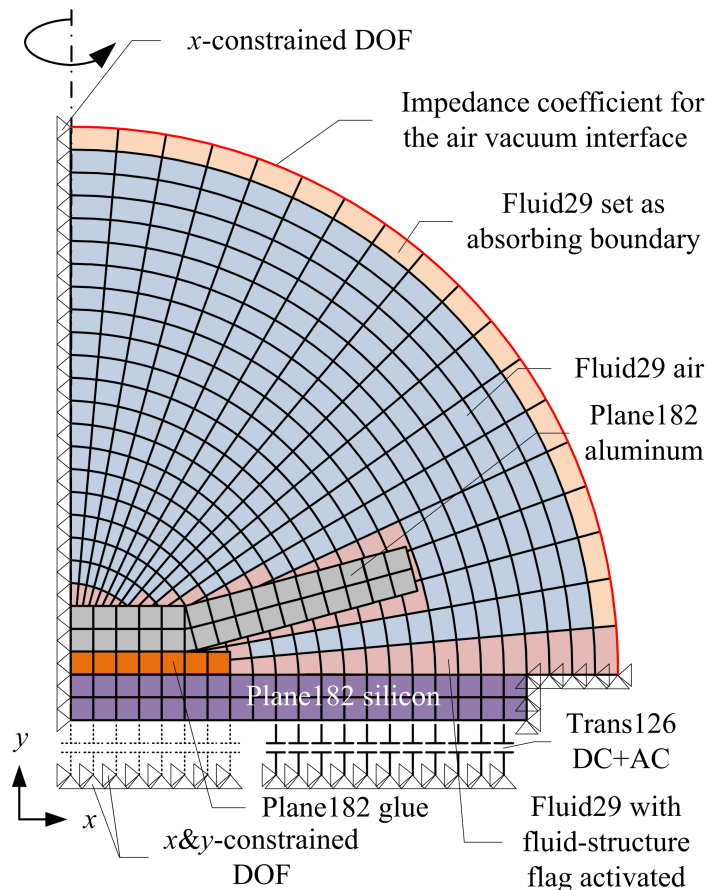


Figure 6.2: Finite element model of the single cell CMUT which is used for the calculation of the static, modal and harmonic response of the circular single cell air coupled CMUT with an aluminum horn glued on top of the plate [15].

6.2 Horn Fabrication and Simulations Results

Based on the diameter of the circular CMUT plate (4 mm), the author modified a commercially available punch pliers by making two different cutting bits for it with 2.5 mm and 3.2 mm in diameter (Figure 6.3). Furthermore, with the desired opening angle of $\alpha = 156^\circ$ [Figure 6.1 (b)] for the horn. By using thin aluminum metal sheets the author succeeded in fabricating several horns with thicknesses ranging from 100 μm to 300 μm .

During a large number of gluing tests of horns on top of a glass substrate the author identified a proper glue and activator combination of Loctite 480 with an activator 7455 (Henkel AG, Düsseldorf, North Rhine-Westphalia, Germany). Due to the black color of this glue, the author determines the glue layer diameter of about about 1.3 mm below the horn by looking through the glass substrate with a standard microscope. Then the thickness was measured, using a caliper, of about 150 μm .

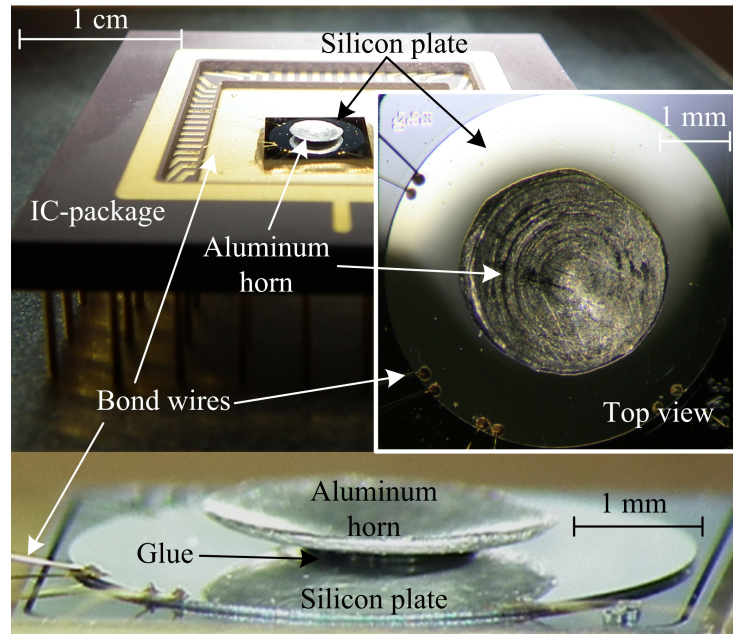


Figure 6.3: A 4 mm diameter single cell air coupled CMUT with an aluminum horn glued on top of the plate. The horn thickness is $100\ \mu\text{m}$ and the diameter is 2.5 mm. The device is glued and wire-bonded to a standard IC-package for electrical connection [15].

In a first step the author performs a non linear prestressed modal analysis [121] for all of these various types of horn geometries in terms of thickness and diameters. This delivers all relevant mode shapes of the entire structure with the corresponding frequencies and values for the effective modal mass for each mode. As a result of this first analysis was found out that the horn with a thickness of $100\ \mu\text{m}$ and a diameter 2.5 mm should be used. Such a horn is sufficiently stiff to avoid any higher mode in the horn itself and for a thicker horn the frequency would drop below 20 kHz due its larger mass [15].

In a next subsequent step the author performs a pre-stressed harmonic analysis to estimate the performance improvement caused by the horn. The FEA predicts that the frequency reduces from 55 kHz down to 27 kHz. The center displacement improves by a factor of 5.5 from 360 nm to $1.97\ \mu\text{m}$ and the average displacement improves by a factor of 9 from 110 nm to $1\ \mu\text{m}$ [15].

6.3 First Measurements for Validation

Before gluing the horn on top of the CMUT plate (Figure 6.3), the author characterizes the CMUT without horn at two different DC bias voltages, i.e. 150V and 180V. For all measurements the author used a calibrated microphone in front of the device (Chapter 3.3.2) [14]). As expected, the author observed that the sound pressure increases when the DC bias voltage is increased. The frequency decreases from 56.4 kHz down to 55.5 kHz due to the spring softening effect (Figure 6.4) [15].

After gluing the horn, the device was characterized again. The author started with a DC bias voltage of 150V and, surprisingly, instead of a drop in operation frequency, due to the increased modal mass, down to the predicted 27 kHz, the author observed a higher frequency of 64 kHz [15]. Further, the measured

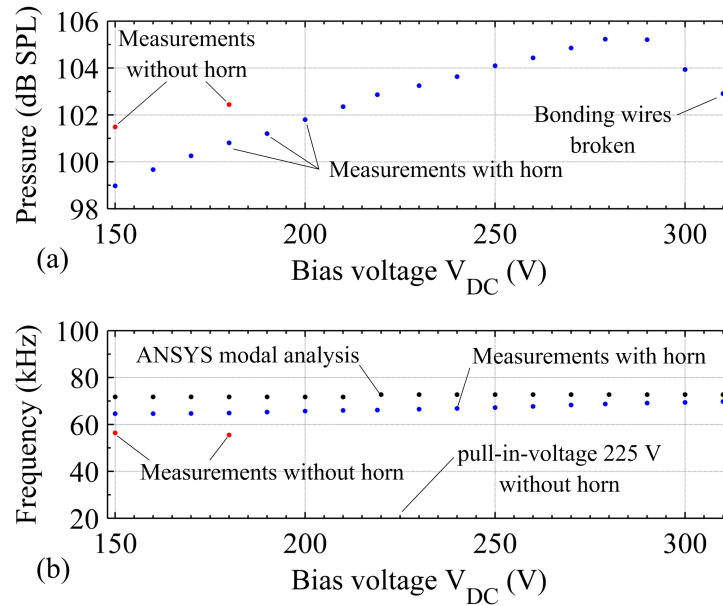


Figure 6.4: Sound pressure levels (a) measured at a distance of 2.6 cm in front of the CMUT with a calibrated microphone (B&K Type 4138-A-015) and a direct comparison of measured and calculated frequencies (b). All before and after gluing the horn at various DC bias voltages. The AC excitation signal was $10V_{pp}$ and the pull-in voltage of the CMUT without horn is 225 V [15].

sound pressure level was 2.5 dB lower (Figure 6.4). When the DC bias voltage was increased, the author observed larger sound pressure levels with a slight increase in operation frequency, which indicates that the device was not operating in conventional operation mode anymore. At a DC bias voltage of 310V the author unfortunately lost a bonding wire, and, thus, stops the measurement.

The behavior that was observed for this CMUT with a horn can be explained as follows: The glue below the horn at the center of the plate creates some tensile stress, which increases the static deflection of the CMUT plate in contrast to the initial expectation that the DC operation point stays unchanged. This is a similar effect as caused by thermal stress, observed in CMUTs with silicon nitride based half-metalized plates [122]. Instead of operating in conventional mode, as the author originally expected, the device operates in a permanent contact mode. Therefore, the horn cannot deploy its full enhancement in terms of sound pressure. The peak of sound pressure at a DC bias voltage of 290V can be explained by the fact that the effective aperture size of the silicon plate (vibrating ring) below the horn increases, and, thus, less energy is coupled into the horn via both the contact point and the air between horn and plate. The slight increase in operation frequency for every increment of DC bias voltage is typical for a CMUT with its plate in contact with the bottom of the cavity (permanent contact mode or beyond pull-in) [15].

To test this hypothesis the author extended the FEA to model the influence of the glue on the static DC operation point of the CMUT plate. It is essential to know that the horn is glued onto the silicon plate after it is deflected by the ambient pressure but before it is connected to the DC voltage source. Similar as in the work described in [122] the author uses the element birth and death feature (ekill and ealive command [121]). Killing an element means that its stiffness matrix will be multiplied by a small multiplication factor, eliminating its influence for a particular static solution step. This extended FEA revealed

that a small tensile stress inside the glue layer below the horn of only 5 MPa is sufficient to bring the plate into permanent contact operation mode. Therefore, the author repeated the non-linear prestressed modal analysis and obtained good agreement to the measurement results [Figure 6.4 (b)].

6.4 Conclusion of a Mechanically Amplified CMUT

A finite element analysis and first measurement results confirm that for a single cell air coupled CMUT, operating at frequencies below 150 kHz, it is a promising idea to simply glue a lightweight horn on top of the plate. Further, through experiments demonstrated that the static operation point of the CMUT can be affected by the glue in the opposite direction as expected. Thus, instead of operating the modified CMUT in conventional mode, the author only managed to validate the finite element model for the non-intended permanent contact mode of a CMUT with a glued horn. But even for this non-intended suboptimal operation mode for a CMUT with horn, the obtained sound pressure levels have been increased by around (3 ± 1) dB [15].

Conclusion and Future Work

In this work several common characterization methods are described and issues identified, which occur during the characterization of ultrasonic transducers. The characterization of the electrical impedance with a small signal analyses using network or impedance analyzer can be quick and precise. However, network analyzer are often designed for an impedance network of 50Ω , and, thus, a mismatch occurs when ultrasonic transducers are characterized over their entire frequency range, from below the short circuit resonance frequency up to above open circuit resonance frequency. The magnitude of the electrical impedance can change several orders of magnitude. In particular those high impedance leads to a significant higher measurement uncertainty, which has to be considered when analyzing those data. Further, ultrasonic transducers are often driven with higher excitation voltages, when used in an industrial application. Thus, they should also be characterized at higher excitation voltages. An influence on the behavior, simply by shifting the resonance frequencies and their electrical impedances, was observed when using the nominal excitation voltages. Depending on the type of ultrasonic transducers the frequency shift comes along with non-linearities such as bifurcation where the displacement over the frequency cycles through a hysteresis. Hence, the displacement is increased by tuning the excitation frequency by lowering the frequency from beyond short circuit resonance frequencies until the displacement reaches its maximum. The non-linearities observed could be used in subsequent steps with the main goal to increase the performance of application by using smart controllers.

The characterization of the electrical impedance is often conducted at ambient temperatures only. However in industrial applications, e.g. ultrasonic flow meters, the ultrasonic transducers are exposed a wide temperature range. Measurements of the electrical impedance of ultrasonic transducers over a wide temperature range of 450°C from -190°C up to $+250^\circ\text{C}$ show non negligible effects due to thermal stress, such as a permanent shift of their nominal resonance frequencies, i.e. both short and open circuit resonance. It was observed that a temper process, deliberately cycling through several temperatures, could stabilize and minimize these effects, which leads to an increased performance of industrial applications. In future work the temper process has to be evaluated if it could suppress the effects of the temperature due to self heating which occurs when ultrasonic transducers are driven by their maximum excitation voltage rated.

The extraction of important parameters out of the electrical impedance is often done based on the Butterworth-van Dyke (BvD) model. The basic BvD is often not enough to reflect all the properties and physical effects of the characterized ultrasonic transducer. Therefore, the BvD is extended in several variations to a more complex model using up to seven parameters. In doing so, the parasitic contact resistance and the parasitic contact capacitance are represented in a 5-elements and 6-elements model respectively. The 7-elements model is reflecting these effects too and in addition the parasitic parallel resistance of the electrodes is represented as well. A complex curve fit algorithm implemented in MATLAB[®] is used to fit these models to electrical impedance measurements of ultrasonic transducers. Further, through monitoring these parameters and analyzing them individually, more robust starting val-

ues are achieved, which lead to better likelihood of successful fit results. For future work, an interesting approach of using a differential evolution algorithm should be investigated further.

In order to achieve a better performance in any applications, two methods to increase the performance are described and applied in prototypes. First, the separation of the vibrating aperture from the acoustic aperture of an ultrasonic transducer, by adding a waveguide, opens the door for many opportunities of improvements, such as adding several degrees of freedom. Having a separated acoustic aperture, which is independent of the ultrasonic transducer, allows the manipulation of the acoustic properties by varying the waveguide in length, thickness and opening. Such a waveguide increases the distance between the media and the ultrasonic transducer. In harsh environment applications one often finds high temperatures, e.g. flair gas flow meters, in-situ non-contact non-destructive testing, or in-situ non-contact non-destructive evaluations at molten metal continuous casting, such waveguide approach opens the door for powerful but temperature sensitive ultrasonic transducers such as piezoelectric bolt-clamped Langevin transducers. The waveguides, 3D printed (metal or ceramics), can increase the distance and volume to an ultrasonic transducer. Therefore passive or active cooling, or heating, can bridge with a temperature gradient to an optimum temperature for operating the ultrasonic transducers. By successfully fabricating and characterizing an air-coupled 1D phased array, operating at 40 kHz, with an element pitch of only half-wavelength using waveguides, the approach of separating the acoustic aperture from the vibrating aperture is demonstrated in both transmit and receive mode, i.e. reciprocity for this type of approach to realize an ultrasonic phased array was proven for the first time.

Second, the mechanical amplification of a capacitive micromachined ultrasonic transducer (CMUT) is achieved, by adding a horn structure, such as is used in monomorph piezoelectric ultrasonic transducers from Murata, on top of an already exciting single cell 55 kHz device. The added horn structure increased the sound pressure level in transmit mode by (3 ± 1) dB although the used glue induced additional mechanical stress to the front plate of the CMUT. In future work the performance of the receive mode should be investigated further. A finite element analysis already indicated in an increased center-to-average displacement in transmit mode and due to reciprocity and in addition the concentration of the energy of the impinging ultrasonic wave to the center should lead to an increased receiver performance.

List of used symbols

Symbol	Numerical value	Unit	Description
A		%	Basic accuracy Keysight E5061B-3L5
B		m Ω	Short offset Keysight E5061B-3L5
B		S	Susceptance
BW		Hz	Bandwidth
BW_o		Hz	Bandwidth at open circuit
BW_s		Hz	Bandwidth at short circuit
C		μ S	Open offset Keysight E5061B-3L5
D		%	Additional error 16047E
F_1		kHz	Frequency of SPD
F_2		MHz	Frequency of SPD
f		Hz	Frequency
$f_{o,1,+3\text{ dB}}$		Hz	Lower cut off frequency of open circuit
$f_{o,2,+3\text{ dB}}$		Hz	Upper cut off frequency of open circuit
$f_{s,1,+3\text{ dB}}$		Hz	Lower cut off frequency of short circuit
$f_{s,2,+3\text{ dB}}$		Hz	Upper cut off frequency of short circuit
G		S	Conductance
i		A	Current (instantaneous value)
\hat{i}		A	Current (amplitude, peak value)
I_{RMS}		A	Current (root mean square value)
j	$j^2 = -1$		Imaginary unit
φ_{error}		°	Phase error
φ_i		°	Phase angle of current
φ_v		°	Phase angle of voltage
φ_x		°	Phase angle of impedance
$\varphi_{z,a}$		rad	Additional phase accuracy Keysight E5061B-3L5
$\varphi_{z,a,\text{fixture}}$		rad	Additional phase accuracy Keysight 16047E
π	3.14159		Mathematical constant
Q			Quality factor
Q_o			Quality factor at open circuit
Q_s			Quality factor at short circuit
R		Ω	Resistance
R_s		Ω	Shunt resistor
Δt_{error}		s	Cursor time error
v		V	Voltage (instantaneous value)
V_{error}		V	Total voltage error
\hat{v}		V	Voltage (amplitude, peak value)

\hat{v}	$\frac{m}{s}$	Velocity amplitude
\hat{v}_n	$\frac{m}{s}$	Velocity noise amplitude
V_{RMS}	V	Voltage (root mean square value)
ω	$\frac{1}{s}$	Angular frequency
X	Ω	Reactance
\hat{x}	m	Displacement amplitude
\underline{Y}	S	Complex electrical admittance
Y_0	S	Open repeatability of admittance
Z	Ω	Electrical impedance
\underline{Z}	Ω	Complex electrical impedance
Z_a	%	Additional impedance accuracy Keysight E5061B-3L5
$Z_{a, \text{fixture}}$	%	Additional impedance accuracy Keysight 16047E
Z_a	$\frac{Ns}{m^3}$	Acoustic impedance
Z_{error}	Ω	Impedance uncertainty voltage divider
Z_m	Ω	Measured impedance
Z_s	Ω	Short repeatability of impedance
Z_x	Ω	Unknown impedance

Acronyms and abbreviation

A	Amplitude (A-scan)
AC	Alternating Current
BLT	Bolt-Clamped Langevin
BNC	Bayonet Neill Concelman
BOX	Buried Oxide Layer
BvD	Butterworth-van Dyke
CMUT	Capacitive Micromachined Ultrasonic Transducer
CUT	Capacitive Ultrasonic Transducer
CW	Continuous Wave
DC	Direct Current
DR	Dynamic Range
DSLR	Digital Single Lens Reflex
DUT	Device under Test
EMAT	Electromagnetic Acoustic Transducer
FEA	Finite Element Analysis
FEM	Finite Element Model
FOV	Field Of View
GND	Ground
HTS	High Temperature Setup
I	Current
IFBW	Intermediate Frequency Band With
INI	Initialization, file format
LED	Light Emitting Diode
LDVM	Laser Doppler Vibrometer
NDE	Non Destructive Evaluation
NDT	Non Destructive Testing
NCNDE	Non Contact Non Destructive Evaluation
NCNDT	Non Contact Non Destructive Testing
ODE	Ordinary Differential Equation
OEXO	Oven Controlled Crystal Oscillator
PID	Proportional Integral Differential controller
PVC	Polyvinyl Chloride
PZT	Lead Zirconium Titanate
R	Reflection input (voltage)
RF	Radio Frequency
SMD	Surface Mounted Device
SOI	Silicon On Insulator
SPC	Supplemental Performance Characteristics

SPD	Supplemental Performance Data
T	Transmission input (current)
TDP	Thermal Design Power
THD	Total Harmonic Distortion
TOF	Time Of Flight
TVSD	Transient Voltage Suppressor Diodes
SNR	Signal to noise Ratio
SPL	Sound Pressure Level
UFM	Ultrasonic Flow Meter
US	Ultrasonic Transducer
USB	Universal Serial Bus
V	Voltage

Bibliography

- [1] A. Jäger, A. Unger, H. Wang, Y. Arnaudov, L. Kang, R. Su, D. Lines, S. N. Ramadas, S. Dixon, and M. Kupnik. “Ultrasonic phased array for sound drift compensation in gas flow metering”. In: *2017 IEEE International Ultrasonics Symposium (IUS)*. Sept. 2017, pp. 1–4. DOI: 10.1109/ULTSYM.2017.8092174.
- [2] A. Jäger, D. Großkurth, M. Rutsch, A. Unger, R. Golinske, H. Wang, S. Dixon, K. Hofmann, and M. Kupnik. “Air-coupled 40-KHZ ultrasonic 2D-phased array based on a 3D-printed waveguide structure”. In: *2017 IEEE International Ultrasonics Symposium (IUS)*. Sept. 2017, pp. 1–4. DOI: 10.1109/ULTSYM.2017.8091892.
- [3] F. Schiewer, Han Wang, A. Unger, N. Stefanova, and M. Kupnik. “Single-transducer acoustic levitator with equidistant vertical positioning capability”. In: *2016 IEEE International Ultrasonics Symposium (IUS)*. Sept. 2016, pp. 1–4. DOI: 10.1109/ULTSYM.2016.7728813.
- [4] S. E. Burrows, S. N. Ramadas, T. J. R. Eriksson, L. Kang, S. M. Dixon, A. Unger, and M. Kupnik. “High temperature flexural ultrasonic transducer for non-contact measurement applications”. In: *2016 Joint IEEE International Symposium on the Applications of Ferroelectrics, European Conference on Application of Polar Dielectrics, and Piezoelectric Force Microscopy Workshop (ISAF/ECAPD/PFM)*. Aug. 2016, pp. 1–3. DOI: 10.1109/ISAF.2016.7578077.
- [5] A. Unger, E. Konetzke, M. Rutsch, M. Hoffmann, S. N. Ramadas, S. Dixon, and M. Kupnik. “Versatile air-coupled phased array transducer for sensor applications”. In: *2015 IEEE SENSORS*. Nov. 2015, pp. 1–4. DOI: 10.1109/ICSENS.2015.7370187.
- [6] C. Hatzfeld, C. Schröder, A. Unger, O. Morar, T. Klemm, M. Kupnik, and R. Werthschützky. “Flow sensor for field measurement of viscous liquid usage for consumer studies”. In: *2015 IEEE SENSORS*. Nov. 2015, pp. 1–4. DOI: 10.1109/ICSENS.2015.7370343.
- [7] E. Konetzke, M. Rutsch, M. Hoffmann, A. Unger, R. Golinske, D. Killat, S. N. Ramadas, S. Dixon, and M. Kupnik. “Phased array transducer for emitting 40-kHz air-coupled ultrasound without grating lobes”. In: *2015 IEEE International Ultrasonics Symposium (IUS)*. Oct. 2015, pp. 1–4. DOI: 10.1109/ULTSYM.2015.00019.
- [8] M. Rutsch, E. Konetzke, A. Unger, M. Hoffmann, S. N. Ramadas, S. Dixon, and M. Kupnik. “Extending the receive performance of phased ultrasonic transducer arrays in air down to 40 kHz and below”. In: *2015 IEEE International Ultrasonics Symposium (IUS)*. Oct. 2015, pp. 1–4. DOI: 10.1109/ULTSYM.2015.00095.
- [9] R. Golinske, M. Hoffmann, E. Konetzke, A. Unger, M. Rutsch, and M. Kupnik. “Diffraction loss calculation based on boundary element method for an air-coupled phased array”. In: *2015 IEEE International Ultrasonics Symposium (IUS)*. Oct. 2015, pp. 1–4. DOI: 10.1109/ULTSYM.2015.00375.
- [10] T. J. R. Eriksson, S. N. Ramadas, A. Unger, M. Hoffman, M. Kupnik, and S. M. Dixon. “Flexural transducer arrays for industrial non-contact applications”. In: *2015 IEEE International Ultrasonics Symposium (IUS)*. Oct. 2015, pp. 1–4. DOI: 10.1109/ULTSYM.2015.00047.

- [11] M. Hoffmann, A. Unger, A. Jäger, and M. Kupnik. “Effect of transducer port cavities in invasive ultrasonic transit-time gas flowmeters”. In: *2015 IEEE International Ultrasonics Symposium (IUS)*. Oct. 2015, pp. 1–4. DOI: 10.1109/ULTSYM.2015.0272.
- [12] A. Guseva, M. Hoffmann, A. Unger, S. Zulk, M. B. El Amien, E. Sarradj, and M. Kupnik. “Ultrasonic transducer characterization in air based on an indirect acoustic radiation pressure measurement”. In: *2015 IEEE International Ultrasonics Symposium (IUS)*. Oct. 2015, pp. 1–4. DOI: 10.1109/ULTSYM.2015.0333.
- [13] Min-Chieh Ho, Maik Hoffmann, Alexander Unger, Park Kwan Kyu, Mario Kupnik, and Butrus T. Khuri-Yakup. “CMUTS in permanent contact operation for high output pressure”. In: *ASME 2015, InterPACKICNMM*. July 2015. URL: <http://tubiblio.ulb.tu-darmstadt.de/77484/>.
- [14] M. Hoffmann, A. Unger, M. C. Ho, Kwan Kyu Park, B. T. Khuri-Yakub, and M. Kupnik. “Volumetric characterization of ultrasonic transducers for gas flow metering”. In: *2013 IEEE International Ultrasonics Symposium (IUS)*. July 2013, pp. 1315–1318. DOI: 10.1109/ULTSYM.2013.0336.
- [15] A. Unger, M. Hoffmann, M. C. Ho, K. K. Park, B. T. Khuri-Yakub, and M. Kupnik. “Finite element analysis of mechanically amplified CMUTs”. In: *2013 IEEE International Ultrasonics Symposium (IUS)*. July 2013, pp. 287–290. DOI: 10.1109/ULTSYM.2013.0074.
- [16] G. Sessler R. Lerch and D. Wolf. *Technische Akustik*. 1st ed. Springer-Verlag Berlin Heidelberg, 2009. ISBN: 978-3-540-23430-2.
- [17] Murata Manufacturing Co., Ltd. *Piezoelectric Ceramic Sensors (Piezotite)*. 2008. URL: <http://application-notes.digchip.com/102/102-44570.pdf> (visited on 04/02/2018).
- [18] INC. STEMINC Steiner & Martins. *Bolt-Clamped Transducers*. 1991. URL: <https://www.steminc.com/PZT/en/bolt-clamped-langevin-transducer-40-khz> (visited on 10/02/2018).
- [19] Inc Universal Flow Monitors. *Universal Flow Meters*. 2018. URL: <http://www.flowmeters.com/> (visited on 03/06/2018).
- [20] J. F. Blackburn, and M. G. Cain. “Nonlinear piezoelectric resonance: A theoretically rigorous approach to constant I-V measurements”. In: *Journal of Applied Physics* 100.11 (2006), p. 114101. DOI: 10.1063/1.2365385.
- [21] D. Guyomar, N. Aurelle, and L. Eyraud. “Piezoelectric Ceramics Nonlinear Behavior. Application to Langevin Transducer”. In: *Journal de Physique III* 7.6 (June 1997), pp. 1197–1208. DOI: 10.1051/jp3:1997183.
- [22] D. Guyomar and B. Ducharne, and G. Sebald. “High nonlinearities in Langevin transducer: A comprehensive model”. In: *Ultrasonics* 51.8 (2011), pp. 1006–1013. ISSN: 0041-624X. DOI: 10.1016/j.ultras.2011.05.017.
- [23] B. V. Tucker. *Vocaltract*, GNU General Public License. Copyright Mar. 2, 2013 Benjamin V. Tucker. 2013. URL: <https://aphl.artsrn.ualberta.ca/?cat=10> (visited on 10/02/2018).
- [24] A. Langen. *Ein Verfahren zur Konstruktion anwendungsoptimierter Ultraschallsensoren auf der Basis von Schallkanälen*. 1st ed. Springer-Verlag Berlin Heidelberg, 1993. ISBN: 978-3-540-57376-0.
- [25] T. Takahashi, R. Takahashi, and S. Jeong. “Ultrasonic phased array sensor for electric travel aids for visually impaired people”. In: *ICMIT 2007: Mechatronics, MEMS, and Smart Materials*. Vol. 6794. Procspie. Provided by the SAO/NASA Astrophysics Data System. Dec. 2007,

- p. 67943V. DOI: 10.1117/12.783988. URL: <http://adsabs.harvard.edu/abs/2007SPIE.6794E..3VT>.
- [26] M. Kota and K. Nakatera. “Ultrasonic Sensor”. 5,495,766. Mar. 1996. (Visited on 04/02/2018).
- [27] R.R. Boullosa, A. Pérez-López, and R. Dorantes-Escamilla. “An Ultrasonic Levitator”. In: *Journal of Applied Research and Technology* 11.6 (2013), pp. 857–865. ISSN: 1665-6423. DOI: 10.1016/S1665-6423(13)71592-X.
- [28] Piceramic. *Ultrasonic Sensor Application Manual*. 2009. URL: <http://www.symmetron.ru/suppliers/murata/files/pdf/murata/ultrasonic-sensors.pdf> (visited on 08/02/2018).
- [29] Murata Manufacturing Co., Ltd. *Data sheet MA40S4S/MA40S4R*. 2017. URL: https://www.murata.com/~media/webrenewal/products/sensor/ultrasonic/open/datasheet_maopn.ashx?la=en (visited on 04/02/2018).
- [30] T. Fritzsche. “Modellierung von modifizierten Ultraschallwandlern zur chemisch/biologischen Anwendung in Flüssigkeiten”. Technische Universität Darmstadt, Fachgebiet Mess- und Sensortechnik, 2016.
- [31] V. Y. Topolov and C. R. Bowen. *Electromechanical Properties in Composites Based on Ferroelectrics*. 1st ed. Springer-Verlag, London, 2009. ISBN: 978-1-84800-999-8.
- [32] Precision Acoustics. 2018. URL: <https://www.acoustics.co.uk/product/1-3-piezo-composite-transducers/> (visited on 08/02/2018).
- [33] S. N. Ramadas et al. “Additive manufacture of impedance matching layers for air-coupled ultrasonic transducers”. In: *2015 IEEE International Ultrasonics Symposium (IUS)*. Oct. 2015, pp. 1–4. DOI: 10.1109/ULTSYM.2015.0367.
- [34] M. Toda and M. Thompson. “Novel multi-layer polymer-metal structures for use in ultrasonic transducer impedance matching and backing absorber applications”. In: *IEEE Transactions on Ultrasonics, Ferroelectrics, and Frequency Control* 57.12 (Dec. 2010), pp. 2818–2827. ISSN: 0885-3010. DOI: 10.1109/TUFFC.2010.1755.
- [35] S. Elgner. “Charakterisierung und Optimierung von Ultraschallwandlern”. Technische Universität Darmstadt, Fachgebiet Mess- und Sensortechnik, 2018.
- [36] Polaroid™. *Series 600 Environmental Grade Ultrasonic Sensor*. 1995. URL: <http://www.robotstorehk.com/6500.pdf> (visited on 20/05/2018).
- [37] SensComp, Inc. *Series 600 Environmental Grade Ultrasonic Sensor*. 2015. URL: <http://www.senscomp.com/pdfs/series-600-envir-grade-ultrasonic-sensor-spec.pdf> (visited on 20/05/2018).
- [38] A. S. Erguri, Y. Huang, X. Zhuang, Ö. Oralkan, G. G. Yarahoglu, and B. T. Khuri-Yakub. “Capacitive micromachined ultrasonic transducers: fabrication technology”. In: *IEEE Transactions on Ultrasonics, Ferroelectrics, and Frequency Control* 52.12 (Dec. 2005), pp. 2242–2258. ISSN: 0885-3010. DOI: 10.1109/TUFFC.2005.1563267.
- [39] M. Kupnik et al. “CMUT fabrication based on a thick buried oxide layer”. In: *2010 IEEE International Ultrasonics Symposium*. Oct. 2010, pp. 547–550. DOI: 10.1109/ULTSYM.2010.5935935.
- [40] D. C. Giancoli. *Physik*. 3rd ed. Pearson Studium, 2009. ISBN: 978-38689-4023-7.
- [41] M. Kogia, L. Cheng, A. Mohimi, V. Kappatos, T.-H. Gan, W. Balachandran, and C. Selcuk. *Electromagnetic Acoustic Transducers Applied to High Temperature Plates for Potential Use in the Solar*

- Thermal Industry*. 2018. URL: <http://www.mdpi.com/2076-3417/5/4/1715/htm> (visited on 05/02/2018).
- [42] American Society for Testing and Materials. *Standard Guide for Electromagnetic Acoustic Transducers (EMATs)*. 1997. URL: http://www.irss.ca/development/documents/CODES%20&%20STANDARDS_02-28-08/ASTM/Ultrasonic/Guides%20for/E1774-96%20EMAT%20Transducers.pdf (visited on 05/02/2018).
- [43] S. Huang, S. Wang, W. Li, and Q. Wang. *Electromagnetic Ultrasonic Guided Waves*. 1st ed. Springer-Verlag, Singapore, 2016. ISBN: 978-981-10-0562-6.
- [44] Osaka University Hirao Laboratory. *Research:EMAT(Electromagnetic acoustic transducer)*. 2018. URL: http://www-ndc.me.es.osaka-u.ac.jp/pmwiki_e/index.php?n=Research.EMATs (visited on 05/02/2018).
- [45] H. Janocha. *Aktoren*. 1st ed. Springer-Verlag Berlin Heidelberg, 1992. ISBN: 978-3-662-00418-0.
- [46] S. Butterworth. "On Electrically-maintained Vibrations". In: *Proceedings of the Physical Society of London*. Vol. 27. 1914, pp. 410–424.
- [47] W. P. Mason. *Electromechanical Transducers and Wave Filters*. 2nd ed. D. van Nostrand Company, Inc., 1942. URL: <https://archive.org/details/in.ernet.dli.2015.13601> (visited on 24/05/2018).
- [48] W. P. Mason. "An Electromechanical Representation of a Piezoelectric Crystal Used as a Transducer". In: *Proceedings of the Institute of Radio Engineers* 23.10 (Oct. 1935), pp. 1252–1263. ISSN: 0731-5996. DOI: 10.1109/JRPROC.1935.227273.
- [49] K. S. Van Dyke. "The Piezo-Electric Resonator and Its Equivalent Network". In: *Proceedings of the Institute of Radio Engineers* 16.6 (June 1928), pp. 742–764. ISSN: 0731-5996. DOI: 10.1109/JRPROC.1928.221466.
- [50] W. G. Cady. "The Piezo-Electric Resonator". In: *Proceedings of the Institute of Radio Engineers* 10.2 (Apr. 1922), pp. 83–114. ISSN: 0731-5996. DOI: 10.1109/JRPROC.1922.219800.
- [51] H. F. Olson. *Acoustical Engineering*. 1st ed. D. van Nostrand Company, Inc., 1957. URL: http://cyrille.pinton.free.fr/electroac/lectures_utiles/son/olson.pdf (visited on 24/05/2018).
- [52] P. Miodrag. *Piezoelectric transducers modeling and characterization*. 2004. URL: <http://alejandria.ccm.itesm.mx/biblioteca/digital/liele/pcmc.pdf> (visited on 22/05/2018).
- [53] W. Weißgerber. *Elektrotechnik für Ingenieure 2*. 6th ed. Vieweg, 2007. ISBN: 978-3-8348-0191-3.
- [54] R. Lerch. *Elektrische Messtechnik*. 6th ed. Springer-Vieweg, 2012. ISBN: 978-3-642-22608-3.
- [55] F. V. Hunt. *Electroacoustics The Analysis of Transduction and Its Historical Background*. 2nd ed. American Institute of Physics for the Acoustical Society of America, 1982. ISBN: 0-88318-401-X.
- [56] W. Böge and W. Pläßmann. *Formeln und Tabellen Elektrotechnik*. 1st ed. Vieweg, 2007. ISBN: 978-3-528-03973-8.
- [57] T. Lohse, and M. zur Neden. *Physik der Musikinstrumente*. 2007. URL: http://www-hera-b.desy.de/people/nedden/lectures/02_03/musik/musik.pdf (visited on 08/06/2013).
- [58] Keysight Technologies. *Impedance Measurement Handbook*. 2018. URL: <https://literature.cdn.keysight.com/litweb/pdf/5950-3000.pdf?id=1000075407:epsq:dow> (visited on 08/02/2018).

- [59] Keysight Technologies. *8 Hints for Successful Impedance Measurements*. 2017. URL: <http://literature.cdn.keysight.com/litweb/pdf/5968-1947E.pdf> (visited on 02/03/2018).
- [60] Keysight Technologies. *Keysight E5061B-3L3/3L4/3L5 LF-RF Network Analyzer with Option 005 Impedance Analysis Function*. 2017. URL: <http://literature.cdn.keysight.com/litweb/pdf/5990-7033EN.pdf> (visited on 02/03/2018).
- [61] Anritsu. *MS4630B Network Analyzer Operation Manual Vol.1 Panel Operation*. 2007. URL: https://dl.cdn-anritsu.com/en-au/test-measurement/files/Manuals/Operation-Manual/MS4630B_W1534AE_opm1_e_10_0.pdf (visited on 02/03/2018).
- [62] Keysight Technologies. *Keysight 16047E Test Fixture*. 2014. URL: <http://literature.cdn.keysight.com/litweb/pdf/16047-90040.pdf> (visited on 02/03/2018).
- [63] STmicroelectronics, Doc ID 3068 Rev 7. *Data sheet P6KE, Transil™ transient voltage surge suppressor (TVS)*. 2012. URL: <http://www.st.com/content/ccc/resource/technical/document/datasheet/1a/3b/f2/a9/96/72/49/ca/CD00000720.pdf/files/CD00000720.pdf/jcr:content/translations/en.CD00000720.pdf> (visited on 15/04/2018).
- [64] TT Electronics. *Data sheet HVC Series, High Voltage Chip Resistors Series*. 2016. URL: <http://www.ttelectronics.com/themes/ttelectronics/datasheets/resistors/HVC.pdf> (visited on 13/04/2018).
- [65] Cornell Dubilier. *Data sheet Type 942C, Polypropylene Capacitors, for Pulse, Snubber*. URL: <http://www.cde.com/resources/catalogs/942C.pdf> (visited on 13/04/2018).
- [66] SRS Stanford Research Systems. *SERIES PS300 High Voltage Power Supply, Revision 3.0*. 2007. URL: <http://www.thinksrs.com/downloads/PDFs/Manuals/PS300m.pdf> (visited on 20/05/2018).
- [67] Keysight Technologies. *Keysight 33500B and 33600A Series Trueform Waveform Generators 20, 30, 80, 120 MHz, Data Sheet*. 2017. URL: <https://literature.cdn.keysight.com/litweb/pdf/5992-2572EN.pdf> (visited on 03/05/2018).
- [68] Dynacord. *SL Series Standard Precision Power Amplifiers*. 2008. URL: https://www.dynacord.com/binary/SL_Technische_Informationen.pdf (visited on 08/02/2018).
- [69] Keysight Technologies. *InfiniiVision 2000 X-Series Oscilloscopes, Data Sheet*. 2018. URL: <https://literature.cdn.keysight.com/litweb/pdf/5990-6618EN.pdf> (visited on 03/05/2018).
- [70] Keysight Technologies. *Keysight N28XXA/B Passive Probes, Data Sheet*. 2018. URL: <https://literature.cdn.keysight.com/litweb/pdf/5990-7111EN.pdf> (visited on 03/05/2018).
- [71] Tektronix®. *DMM 7510 7½-Digit Graphical Sampling Multimeter, Data Sheet*. URL: <https://www.tek.com/tektronix-and-keithley-digital-multimeter/dmm7510> (visited on 03/05/2018).
- [72] Working Group 1 of the Joint Committee for Guides in Metrology (JCGM/WG 1). *Evaluation of measurement data — Guide to the expression of uncertainty in measurement*. 2008. URL: http://www.bipm.org/utils/common/documents/jcgm/JCGM_100_2008_E.pdf (visited on 22/05/2018).
- [73] memert. *memmert, Betriebsanleitung*. 2011. URL: <https://www.memmert.com/index.php?eID=dumpFile&t=f&f=2771&token=420bb30982313abf3a3b5d10e5f2f04ff48f8287> (visited on 23/05/2018).
- [74] J. Lunze. *Regelungstechnik 1*. 8th ed. Springer-Verlag Berlin Heidelberg, 2010. ISBN: 978-3-642-13808-9.

- [75] LAPP. *Ölflex® HEAT 260 SC*. 2016. URL: <https://www.lappkabel.de/produkte/online-kataloge-shop/anschluss-und-steuerleitungen/erweiterte-umgebungstemperaturen/ptfe-einzeladern-190c-bis-260c/oelflex-heat-260-sc.html> (visited on 08/02/2018).
- [76] A. Unger. "ENTWICKLUNG EINES MESSPLATZES FÜR TEMPERATURTESTS VON ULTRASCHALLWANDLERN". BTU Cottbus-Senftenberg, Lehrstuhl für Allgemeine Elektrotechnik und Messtechnik, 2012.
- [77] Polytec GmbH. *OFV-534 Kompaktmesskopf, Datenblatt*. 2015. URL: https://www.polytec.com/fileadmin/d/Corporate/OM_DS_OFV-534_D_42377.pdf (visited on 18/04/2018).
- [78] Polytec GmbH. *Laser Doppler Vibrometer, Manual*. URL: https://www.atecorp.com/ATECorp/media/pdfs/data-sheets/Polytec-OFV-3001_Manual.pdf (visited on 18/04/2018).
- [79] Physik Instrumente. *Precision Translation Stage M-403, Data sheet*. 2017. URL: https://static.physikinstrumente.com/fileadmin/user_upload/physik_instrumente/files/datasheets/M-403-Datasheet.pdf (visited on 28/04/2018).
- [80] GW Instek. *Arbitrary Function Generator AFG-2225, User Manual*. 2017. URL: http://www.gwinstek.com/en-global/products/Signal_Sources/Arbitrary_Function_Generators/AFG-2225 (visited on 08/02/2018).
- [81] M. Zollner and E. Zwicker. *Elektroakustik*. 3rd ed. Springer, Berlin, 2003. ISBN: 978-3540646655.
- [82] G. M. Sessler. *Schallreflexionsarmer Raum*. URL: http://www.ea.tu-darmstadt.de/elektroakustik_nt/measuring_facilities_1/einrichtungen_ea_nt_2.de.jsp (visited on 18/05/2018).
- [83] Physik Instrumente. *Precision Rotations Stage M-060, Data sheet*. 2018. URL: https://www.physikinstrumente.de/fileadmin/user_upload/physik_instrumente/files/datasheets/M-060-Datasheet.pdf (visited on 28/04/2018).
- [84] isel Germany AG. *Lineareinheiten Übersicht*. URL: https://www.isel.com/de/downloads/dl/file/id/9001/technische_daten_bestellangaben_aller_lineareinheiten.pdf (visited on 18/05/2018).
- [85] Brüel & Kjær. *1/8" Pressure-field Microphone - Type 4138*. 2008. URL: <https://www.bksv.com/media/doc/bp2030.pdf> (visited on 18/05/2018).
- [86] M. Rutsch. "Charakterisierung von Ultraschallwandler Arrays". Technische Universität Darmstadt, Fachgebiet Mess- und Sensortechnik, 2017.
- [87] M. Rutsch. "Anleitung akustische Messkammer". Technische Universität Darmstadt, Fachgebiet Mess- und Sensortechnik, 2018.
- [88] National Instruments. *PXI-5922 24-Bit, Flexible Resolution PXI Oscilloscope, Data sheet*. 2017. URL: <http://www.ni.com/pdf/manuals/374033a.pdf> (visited on 18/05/2018).
- [89] Brüel & Kjær. *Condenser Microphones and Microphone Preamplifiers for acoustic measurements, Data Handbook*. 1982. URL: <https://www.bksv.com/media/doc/be0089.pdf>.
- [90] Yokogawa Electronic Cooperation. *DL750 ScopeCorder, Manual*. 2002. URL: <https://cdn.tmi.yokogawa.com/IM701210-04E.pdf> (visited on 23/04/2013).
- [91] Y. Bendel. "Schlierenaufnahmesystem zur Darstellung des Schallfeldes eines akustischen Levitators". Technische Universität Darmstadt, Fachgebiet Mess- und Sensortechnik, 2018.
- [92] M. Rutsch. "Auslegung eines konfigurierbaren effizienten parametrischen Ultraschall-Lautsprechers". BTU Cottbus-Senftenberg, Lehrstuhl für Allgemeine Elektrotechnik und Messtechnik, 2014.

- [93] A. Marzo, T. Corkett, and B. W. Drinkwater. “Ultraino: An Open Phased-Array System for Narrow-band Airborne Ultrasound Transmission”. In: *IEEE transactions on ultrasonics, ferroelectrics, and frequency control* 65.1 (2018), pp. 102–111. DOI: 10.1109/TUFFC.2017.2769399.
- [94] M. Klemm et al. “Performance Assessment of CMUT Arrays Based on Electrical Impedance Test Results”. In: *Journal of Microelectromechanical Systems* 24.6 (Dec. 2015), pp. 1848–1855. ISSN: 1057-7157. DOI: 10.1109/JMEMS.2015.2445937.
- [95] H. Fritze et al. “High temperature bulk acoustic wave properties of langasite”. In: *Phys. Chem. Chem. Phys.* 5 (23 2003), pp. 5207–5214. DOI: 10.1039/B307503F. URL: <http://dx.doi.org/10.1039/B307503F>.
- [96] A. Arnau, Y. Jimenez, and T. Sogorb. “An extended Butterworth Van Dyke model for quartz crystal microbalance applications in viscoelastic fluid media”. In: *IEEE Transactions on Ultrasonics, Ferroelectrics, and Frequency Control* 48.5 (Sept. 2001), pp. 1367–1382. ISSN: 0885-3010. DOI: 10.1109/58.949746.
- [97] G. K. Reeves and H. B. Harrison. “Contact resistance of polysilicon silicon interconnections”. In: *Electronics Letters* 18.25 (Dec. 1982), pp. 1083–1085. ISSN: 0013-5194. DOI: 10.1049/el:19820741.
- [98] J. A. Thiele, and M. P. da Cunha. “Platinum and palladium high-temperature transducers on langasite”. In: *IEEE Transactions on Ultrasonics, Ferroelectrics, and Frequency Control* 52.4 (Apr. 2005), pp. 545–549. ISSN: 0885-3010. DOI: 10.1109/TUFFC.2005.1428035.
- [99] J. A. Nelder and R. Mead. “A Simplex Method for Function Minimization”. In: *The Computer Journal* 7.4 (1965), pp. 308–313. DOI: 10.1093/comjnl/7.4.308. eprint: /oup/backfile/content_public/journal/comjnl/7/4/10.1093/comjnl/7.4.308/2/7-4-308.pdf. URL: <http://dx.doi.org/10.1093/comjnl/7.4.308>.
- [100] Inc. The MathWorks. *MATLAB Documentation R2016a*. 2018.
- [101] J. C. Lagarias, J. A. Reeds, M. H. Wright, and P. E. Wright. “Convergence Properties of the Nelder–Mead Simplex Method in Low Dimensions”. In: 9 (Dec. 1998), pp. 112–147.
- [102] K. S. Mylvaganam. “High-rangeability ultrasonic gas flowmeter for monitoring flare gas”. In: *IEEE Transactions on Ultrasonics, Ferroelectrics, and Frequency Control* 36.2 (Mar. 1989), pp. 144–149. ISSN: 0885-3010. DOI: 10.1109/58.19144.
- [103] M. Kupnik, A. Schröder, and M. Gröschl. “Adaptive Asymmetric Double-Path Ultrasonic Transit-Time Gas Flowmeter”. In: *2006 IEEE Ultrasonics Symposium*. Oct. 2006, pp. 2429–2432. DOI: 10.1109/ULTSYM.2006.543.
- [104] T. Hoshi, M. Takahashi, T. Iwamoto, and H. Shinoda. “Noncontact Tactile Display Based on Radiation Pressure of Airborne Ultrasound”. In: *IEEE Transactions on Haptics* 3.3 (July 2010), pp. 155–165. ISSN: 1939-1412. DOI: 10.1109/TOH.2010.4.
- [105] S. Inoue, Y. Makino, and H. Shinoda. “Active touch perception produced by airborne ultrasonic haptic hologram”. In: *2015 IEEE World Haptics Conference (WHC)*. June 2015, pp. 362–367. DOI: 10.1109/WHC.2015.7177739.
- [106] S. Harput and A. Bozkurt. “Ultrasonic Phased Array Device for Acoustic Imaging in Air”. In: *IEEE Sensors Journal* 8.11 (Nov. 2008), pp. 1755–1762. ISSN: 1530-437X. DOI: 10.1109/JSEN.2008.2004574.

- [107] I. O. Wygant, M. Kupnik, J. C. Windsor, W. M. Wright, M. S. Wochner, G. G. Yaralioglu, M. F. Hamilton, B. T. Khuri-Yakub. "50 kHz capacitive micromachined ultrasonic transducers for generation of highly directional sound with parametric arrays". In: *IEEE Transactions on Ultrasonics, Ferroelectrics, and Frequency Control* 56.1 (Jan. 2009), pp. 193–203. ISSN: 0885-3010. DOI: 10.1109/TUFFC.2009.1019.
- [108] M. Kupnik, I. O. Wygant, and B. T. Khuri-Yakub. "Finite element analysis of stress stiffening effects in CMUTS". In: *2008 IEEE Ultrasonics Symposium*. Nov. 2008, pp. 487–490. DOI: 10.1109/ULTSYM.2008.0119.
- [109] J. Benesty et al. "On Microphone-Array Beamforming From a MIMO Acoustic Signal Processing Perspective". In: *IEEE Transactions on Audio, Speech, and Language Processing* 15.3 (Mar. 2007), pp. 1053–1065. ISSN: 1558-7916. DOI: 10.1109/TASL.2006.885251.
- [110] S. A. Schelkunoff. "A Mathematical Theory of Linear Arrays". In: *Bell System Technical Journal* 22.1 (), pp. 80–107. DOI: 10.1002/j.1538-7305.1943.tb01306.x. URL: <https://onlinelibrary.wiley.com/doi/abs/10.1002/j.1538-7305.1943.tb01306.x>.
- [111] G. Allevato. "Signalverarbeitungsarchitektur für die Bildgebung mit Luftultraschall-Phased-Arrays". Technische Universität Darmstadt, Fachgebiet Mess- und Sensortechnik, 2018.
- [112] P. C. Eccardt, K. Niederer, T. Scheiter, and C. Hierold. "Surface micromachined ultrasound transducers in CMOS technology". In: *1996 IEEE Ultrasonics Symposium. Proceedings*. Vol. 2. Nov. 1996, 959–962 vol.2. DOI: 10.1109/ULTSYM.1996.584150.
- [113] B. T. Khuri-Yakub, S. T. Hansen, and A. S. Ergun. *DC-GHz micromachined capacitor microphones*. Aug. 2001. URL: <http://www.dtic.mil/docs/citations/ADA512915> (visited on 22/03/2013).
- [114] J. G. Knight and F. L. Degertekin. "Capacitive micromachined ultrasonic transducers for forward looking intravascular imaging arrays". In: *2002 IEEE Ultrasonics Symposium, 2002. Proceedings*. Vol. 2. Oct. 2002, 1079–1082 vol.2. DOI: 10.1109/ULTSYM.2002.1192482.
- [115] M. N. Senlik, S. Olcum, and A. Atalar. "Improved performance of cMUT with nonuniform membranes". In: *IEEE Ultrasonics Symposium, 2005*. Vol. 1. Sept. 2005, pp. 597–600. DOI: 10.1109/ULTSYM.2005.1602923.
- [116] M. Wang, J. Chen, X. Cheng, C. Li, and X. Liu. "Fabrication and characterization of surface micromachined CMUT with a bossed membrane". In: *2008 IEEE Ultrasonics Symposium*. Nov. 2008, pp. 394–397. DOI: 10.1109/ULTSYM.2008.0097.
- [117] Y. Huang, E. O. Haggstrom, X. Zhuang, A. S. Ergun, and B. T. Khuri-Yakub. "Capacitive micromachined ultrasonic transducers (cmuts) with piston-shaped membranes". In: *IEEE Ultrasonics Symposium, 2005*. Vol. 1. Sept. 2005, pp. 589–592. DOI: 10.1109/ULTSYM.2005.1602921.
- [118] S. H. Wong, M. Kupnik, K. B. Pauly, and B. T. Khuri-Yakub. "Capacitive micromachined ultrasonic transducer (CMUT) for MR-guided noninvasive therapeutic ultrasound applications". In: *TRANSDUCERS 2009 - 2009 International Solid-State Sensors, Actuators and Microsystems Conference*. June 2009, pp. 354–357. DOI: 10.1109/SENSOR.2009.5285491.
- [119] Y. Zhang, R. Howver, B. Gogoi, and N. Yazdi. "A high-sensitive ultra-thin MEMS capacitive pressure sensor". In: *2011 16th International Solid-State Sensors, Actuators and Microsystems Conference*. June 2011, pp. 112–115. DOI: 10.1109/TRANSDUCERS.2011.5969151.

-
- [120] M. C. Ho, M. Kupnik, and B. T. Khuri-Yakub. “FEA of CMUTs suitable for wide gas pressure range applications”. In: *2010 IEEE International Ultrasonics Symposium*. Oct. 2010, pp. 1234–1237. DOI: 10.1109/ULTSYM.2010.5935678.
- [121] Ansys Inc., Canonsburg, PA. *ANSYS 14.0 Manual*.
- [122] M. Kupnik, A. S. Ergun, X. Zhuang, A. S. Ergun, B. Bayram, Ö. Oralkan, S. H. Wong, D. Lin, and B. T. Khuri-Yakub. “5I-6 Finite Element Analysis of Fabrication Related Thermal Effects in Capacitive Micromachined Ultrasonic Transducers”. In: *2006 IEEE Ultrasonics Symposium*. Oct. 2006, pp. 942–945. DOI: 10.1109/ULTSYM.2006.254.

List of Figures

2.1	Overview of air coupled ultrasonic transducers	7
2.2	Piezo modes	8
2.3	Murata MA40S4S ultrasonic transducer	9
2.4	Murata MA40S4S cutted in half	9
2.5	1-3 Composite Transducer	10
2.6	Bolt-Clamped Langevin Ultrasonic Transducer	11
2.7	SensComp 600 series ultrasonic transducer	12
2.8	Capacitive Micromachined Ultrasonic Transducer	14
2.9	Butterworth-van Dyke model	17
2.10	Butterworth-van Dyke model and its behavior over frequency	18
2.11	The complex vocal tract of a human	23
3.1	Test fixture compensation	28
3.2	Accuracy Keysight E5061B-3L5	31
3.3	Accuracy Keysight 16047E test fixture	32
3.4	Bias-T schematics	33
3.5	Bias-T circuit with protection diodes	34
3.6	Measured Bias-T with protection circuit	36
3.7	Error of Bias-T with protection circuit	37
3.8	Details of error of Bias-T with protection circuit	38
3.9	Impedance measurement schematic for higher voltages	40
3.10	Impedance measurement compared with E5061B-3L5	42
3.11	Cryo temperature impedance measurement setup	44
3.12	Vibrometer setup	48
3.13	Mounting plate for DUTs	49
3.14	Volumetric sound pressure measurement setup based on Goniometer	53
3.15	Volumetric sound pressure measurement setup based 3D linear stages	55
3.16	Schlieren setup	57
3.17	Schlieren photography of a Murata ultrasonic transducer	58
3.18	Schlieren photography of a parametric array and a focused array	58
4.1	Overview of a selction of the different BvD model extensions	60
4.2	Dependency on the series resistance of the extended BvD model	65
4.3	Dependency on the series inductance of the extended BvD model	66
4.4	Dependency on the series capacitance of the extended BvD model	67
4.5	Dependency on the parallel capacitance of the extended BvD model	68
4.6	Dependency on the contact resistance of the extended BvD model	69
4.7	Dependency on the parallel resistance of the extended BvD model	70

4.8	Dependency on the contact capacitance of the extended BvD model	71
4.9	Monitoring of bad values of the pararemters	76
4.10	LabVIEW program for visualizing the BvD model parameters	77
4.11	Monitoring of good values of the pararemters	78
4.12	Fit results of a 8.5 MHz CMUT	79
4.13	Parameter overview of a 8.5 MHz CMUT fit result	80
5.1	Prototype of an air coupled phased array operting at 40 <i>kilo</i> Hz	83
5.2	Design mold made of aluminum	83
5.3	Schematic of a waveguide including a Murata ultrasonic transducer	85
5.4	Experimental measurement setup of the 1D phase array	85
5.5	Cross section from a volumetric measurement, 1D phased array steered at -35°	86
5.6	Measured transmit beam directivity pattern	86
6.1	Schematic of a circular single-cell air-coupled CMUT featureing a horn	89
6.2	FE model of a mechanically amplified CMUT	90
6.3	A single cell CMUT with mechanically amplifier	91
6.4	Sound pressure level measurements of a machanically amplified CMUT	92

List of Tables

1.1	Overview of typical frequencies of ultrasound	1
2.1	Analogy of parameters	17
3.1	Main specification of the audio amplifier Dynacord SL2400	39
3.2	Main specification of Polytec LDVM OFV 3001	46
3.3	Main specification of Polytec laser unit with sensor head OFV 534	46
3.4	Main specification of PI M-403.4 DG translational linear stages	47
3.5	Main specification data of rotational stages M-061.2S and M-062.2S [83]	52
3.6	Main specification of the 4138-A-015 microphone unit [85]	52
3.7	Main specification data of NI PXI-5922 24-Bit PXI oscilloscope [88]	53
3.8	Comparison of volumetric measurement systems 3D stage linear vs. Goniometer	56
5.1	Main characteristics of a Murata MA40S4S ultrasonic transducer	83

Curriculum vitae

Alexander Unger

Adress: Elisabeth-Selbert-Str. 4
64289 Darmstadt

Phone: +49 6151 78 73 594

Mobil: +49 177 506 33 56

E-Mail: alexander.earl.unger@gmail.com

Education

since 02/2015 PhD student at the Technische Universität Darmstadt, at the Chair of Measurement and Sensor Technology

10/2012 – 01/2015 PhD student at the BTU Cottbus-Senftenberg, at the Chair of Electrical Engineering and Measurement Technique

09/2012 Diploma degree in Electrical Engineering

10/2007 – 09/2012 Studies of Electrical Engineering, at BTU Cottbus-Senftenberg

Awards

11/2013 Award for Junior Researchers of the federal state Brandenburg

01/2013 Award for the Best Diploma Thesis of the Faculty III, BTU Cottbus-Senftenberg
